

**NSF/REU
RESEARCH EXPERIENCE
FOR UNDERGRADUATES
IN PHYSICS**



STUDENT RESEARCH PAPERS

SUMMER 2011

VOLUME 22

REU DIRECTOR

UMESH GARG, PH.D.



REU Student Research Papers – Summer 2011
University of Notre Dame – Department of Physics

Student	Research Title	Page No.
Andrew Arend University of Wisconsin	Thickness Measurements and Isotopic Identification of Cadmium, Tin, and Tellurium Targets	1
Molly Ball Monmouth College	Correction Methods for Project GRAND Data	11
Brittany Batman Manchester College	A Simulated Galaxy Redshift Distribution	21
Christopher Bell University of Notre Dame	Numerical Methods in Quantum Field Theories	31
Anna Czerepak University of Illinois	Pt-Ir Tip Etching Techniques for Scanning Tunneling Microscopy	42
Erin Dahlstrom Rice University	Examination of the Validity of Statistical Models for the $^{12}\text{C} + ^{12}\text{C}$ Fusion Reaction at Sub-barrier Energies	52
Joshua Ferguson Butler University	Double Chooz and Neutrino Detection	62
Quinn Hailes Hampton University	Measuring the Half-Life of ^{60}Fe Data Analysis	72
John Hardin University of North Carolina Kevin McDermott University of Notre Dame	Analyzing Potential Tracking Algorithms for the Upgrade to the Silicon Tracker of the Compact Muon Solenoid	83
Robert Heitz Virginia Tech	Recoil Mass Separator Hysteresis Measurements and Germanium Detector Development	101

Student	Research Title	Page No.
Janie Hoormann Baylor University	Magnetic Fields in a Supernovae-driven, Stratified Disk	111
Justin Kelly Northern Arizona University	Magnetotransport of Topological Insulators: Bismuth Selenide and Bismuth Telluride	120
Ruben Medina California State – Dominguez Hills	Magnetic Properties of $\text{La}_{0.7}\text{Sr}_{0.3}\text{Mn}_{1-x}\text{Ni}_x\text{O}_3$ Perovskites	130
Nishanth Sasankan University of Texas - Austin	Energetics in Ice VI	142
Branden Summa University of Notre Dame	The Effects of an Accretion Stream on the Period and Spectra of a Cataclysmic Variable	151
Bryant Vande Kolk Ripon College	Searching for Transients in the Kepler Mission Data	161

THICKNESS MEASUREMENTS AND
ISOTOPIC IDENTIFICATION OF
CADMIUM, TIN, AND TELLURIUM
TARGETS

ANDY AREND

2011 NSF/REU Program
Physics Department, University of Notre Dame

Advisors: W. TAN, S. R. LESHER, A. APRAHAMIAN

1. Abstract

The nature and site of the p-process is still a major enigma in our understanding of nucleosynthesis. The p-process is thought to be responsible for the origin of the 35 most neutron deficient stable even-even isotopes between $^{92,94}\text{Mo}$ and ^{196}Hg [1]. The nature of the p-process is still under debate but currently the most favored interpretation is gamma-induced photodisintegration of stable nuclei. There are significant challenges in understanding these reaction rates, particularly near the Cd, Sn, and Te isotopes. In preparation for measuring some of the relevant rates we characterized a set of 54 thin foil targets of Cd, Sn, or Te. The targets had Al or C backings and Al or Ta frames.

Using Particle Induced X-ray Emission (PIXE), we determined the elemental composition of each target by comparing the observed x-ray emission lines with that of the characteristic emissions of the relevant elements. While PIXE is a useful technique for identifying the elemental compositions of the foils, we concluded that it is not an accurate method of measuring foil thickness. We next used Rutherford Backscattering with a $^{12}\text{C}^{3+}$ beam to determine the isotopic composition and thicknesses of the targets. A Silicon detector was placed at 150° with respect to the beam direction to detect the back-scattered ^{12}C particles. A mixed ^{148}Gd ^{241}Am α -source was used to ensure a good energy calibration.

Analyzing the energy at the leading edge of the energy spectrum of the scattered particles allowed identification of the specific isotopes in each sample. The width of the scattered ^{12}C peak, indicating the maximum energy loss of ^{12}C in a target, yielded the thickness of the target when compared to calculations. The target thicknesses range from about 87 to 913 $\mu\text{g}/\text{cm}^2$.

2 Introduction

2.1 P-Process

The nature and site of the p-process is still a major enigma in our understanding of nucleosynthesis. The p-process is thought to be responsible for the origin of the 35 most neutron deficient stable even-even isotopes between $^{92,94}\text{Mo}$ and ^{196}Hg [1]. The nature of the p-process is still under debate but currently the most favored interpretation is gamma-induced photodisintegration of stable nuclei. Alternative possibilities include proton capture (p,γ) by stable heavy nuclides. Proton capture now seems unlikely because of the increasing coulomb barrier associated with heavier elements. The chief ways to compensate for high coulomb barriers are increased kinetic energy i.e. increased temperature or very proton rich environments [2]. Neither condition is present in sufficient magnitude in stars to adequately explain the p-process.

2.2 PIXE

The Pauli exclusion principle states that no two electrons may occupy the same quantum state. Therefore all electrons of an atom must occupy certain discrete energy levels [3]. When an atom is bombarded with ions of sufficient energy, the inner shell (K or L) electrons can be excited into a state of ionization. Outer shell electrons then fall into the newly vacant lower shell orbits. These orbital changes include photon emissions of specific energy levels, typically in the x-ray spectrum. All elements have certain characteristic x-ray emissions, enabling elemental analysis of samples by inducing x-ray emissions. A simple detector apparatus can be used for this analysis. This process is called Particle Induced X-ray Emission (PIXE). PIXE enables only elemental analysis as it is dependent solely upon the atomic number of the target nucleus, and therefore cannot be used to determine isotopic makeup of samples. Additionally, this method is limited to

use with thin films or surface layers of samples, typically with thicknesses on the order of hundreds of $\mu\text{g}/\text{cm}^2$. PIXE is a powerful non-destructive method of analysis which has applications in physics, biology, materials science, geology, archaeology, and in the art world [4].

2.3 Rutherford Backscattering

Rutherford Backscattering is a high kinetic energy elastic collision between an incident ion beam and a target particle. Ions fired at a thin foil have a chance of interacting with and scattering off of the atomic nucleus through a coulomb collision. The chance of scattering (cross-section) of the reaction depends upon the atomic number and isotope, among other things. The cross-section of the reaction is characteristic of each isotope in the target and incident beam and can be used to determine the isotopic composition of the target sample [5].

3 Experimental Methods

All experiments were conducted using the FN tandem accelerator at the university of Notre Dame Nuclear Science Laboratory (NSL). Tandem accelerators work by attracting negatively charged ions to a high voltage terminal. At the terminal, the beam passes through a thin foil which strips electrons from the atoms and creates positive ions. Additionally, because the ions are now of the same charge as the terminal they are repelled from the terminal.

3.1 PIXE

The incident proton beam was generated using the tandem FN accelerator at the NSL. The thin foils were analyzed in 9 runs of 6 targets each. At the beginning and end of each run, background was taken by running the beam through an empty target.

Initial PIXE data was captured and analyzed using the Maestro software system. Figure 3.1.1 shows the initial data for a Tin target before the removal of background. Figure 3.1.2 shows the same target data after background was subtracted. Background was calculated for each run by averaging the two background measurements. The total number of counted events in the main peak was then normalized so that the background level was scaled to be the same as the background on the initial set of runs. This removed the variable of fluctuation in beam strength. The carbon backings did not absorb as many of the x-rays emitted by the targets as did the aluminum backings. Thus, a further correction was made to targets with aluminum backings. The composition of the targets was determined by the location of the main as well as lesser peaks. Cadmium targets had their largest peak at the same level as the background Argon peak. The lesser peak at 3.1 MeV was used to confirm that the target was not merely background. Tin and Tellurium targets could be easily identified.

Figure 3.1.1 Tin Target Data on Maestro Software Before Background Subtraction

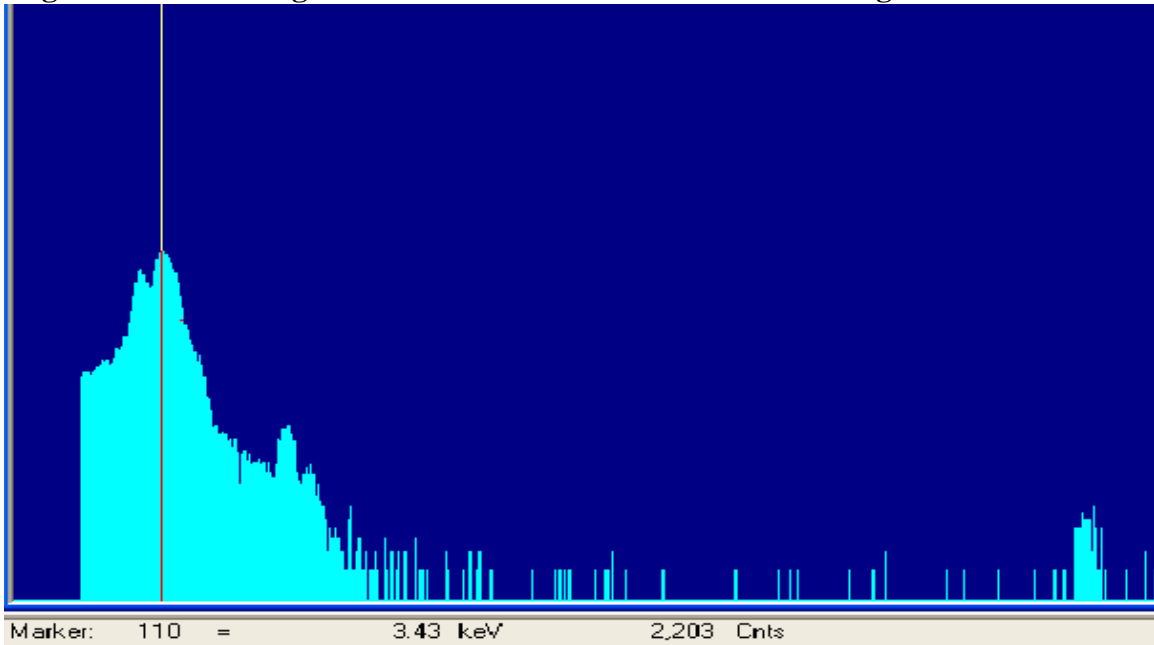
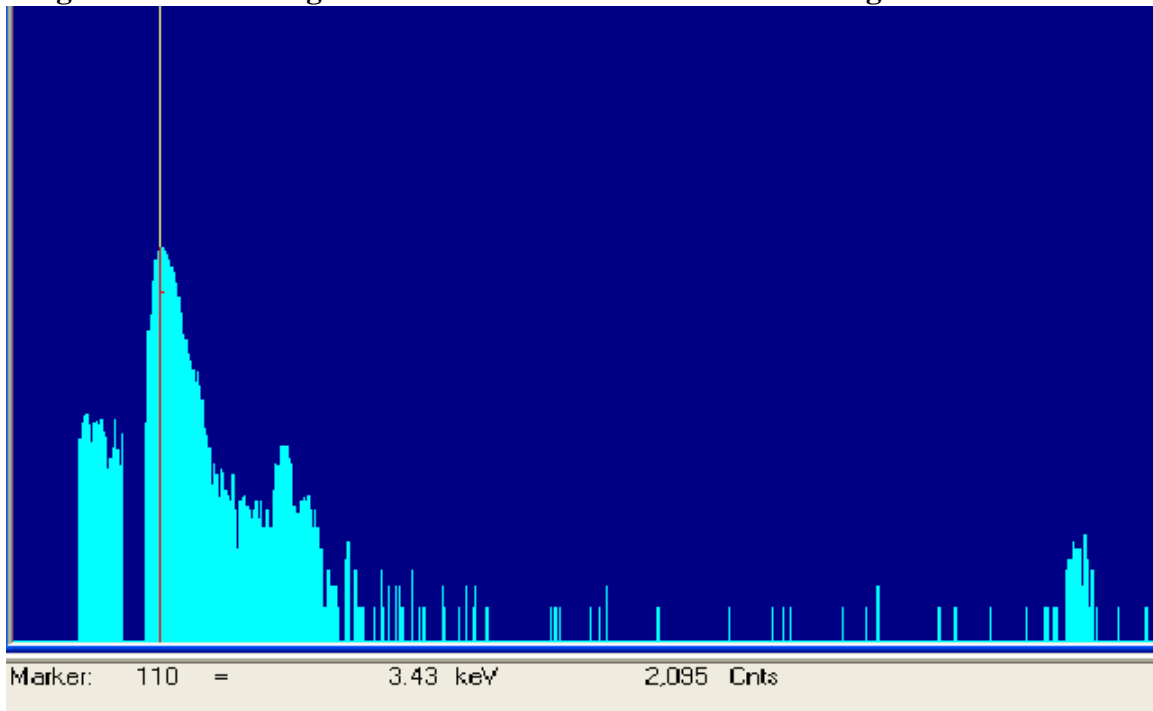


Figure 3.1.2 Tin Target Data on Maestro Software after Background Subtraction



3.2 Backscattering

The Rutherford Backscattering (RBS) experiment used a mixed ^{148}Gd ^{241}Am alpha source and a silicon detector at 150° with respect to the beam direction. The incident ion beam was $^{12}\text{C}^{3+}$ at 15 MeV using the tandem FN accelerator at the NSL. The beam energies ranged from 15.003 to 15.005 MeV, calculated using proprietary software and measurements from the accelerator controls. Only 14 of the 54 foils tested in PIXE were tested again in the RBS experiment. Figure 3.2.1 shows data from a sample of Tellurium that was ultimately determined to be $555 \mu\text{g}/\text{cm}^2$ thick $^{120}\text{TeO}_2$. The two alpha peaks are of known energy and therefore easily used for calibration.

The energy loss of the scattered particles was determined from the Full-width Half Maximum (FWHM) of the energy peak. The region of interest of the same data from Figure 3.2.1 is shown below in Figure 3.2.2.

Figure 3.2.1 RBS Data from a Tellurium Target

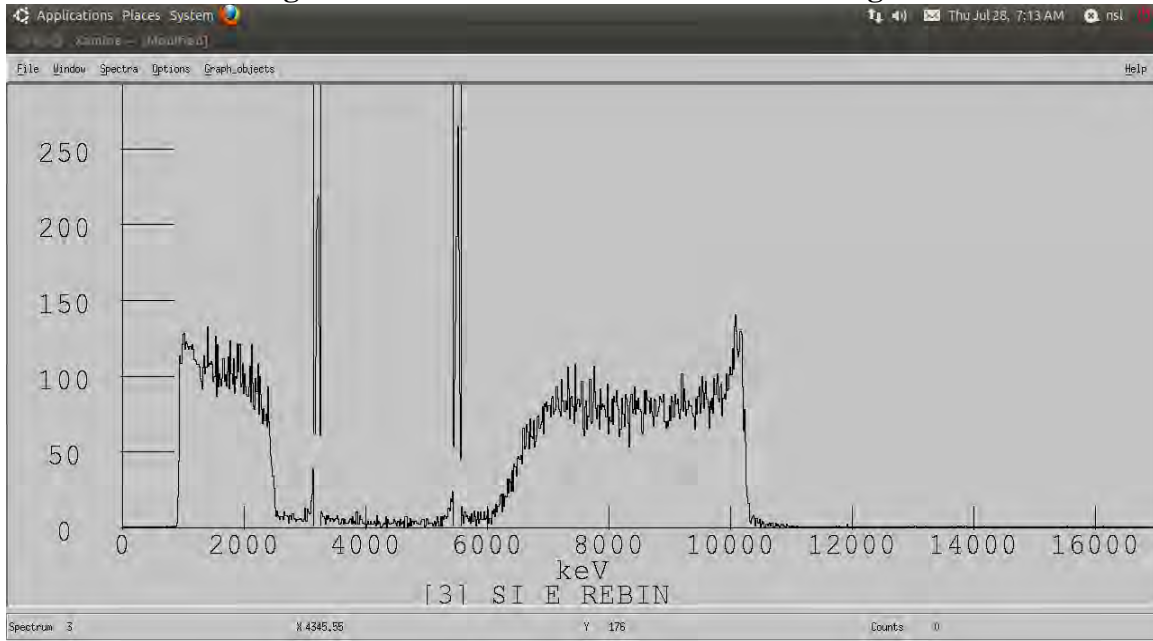
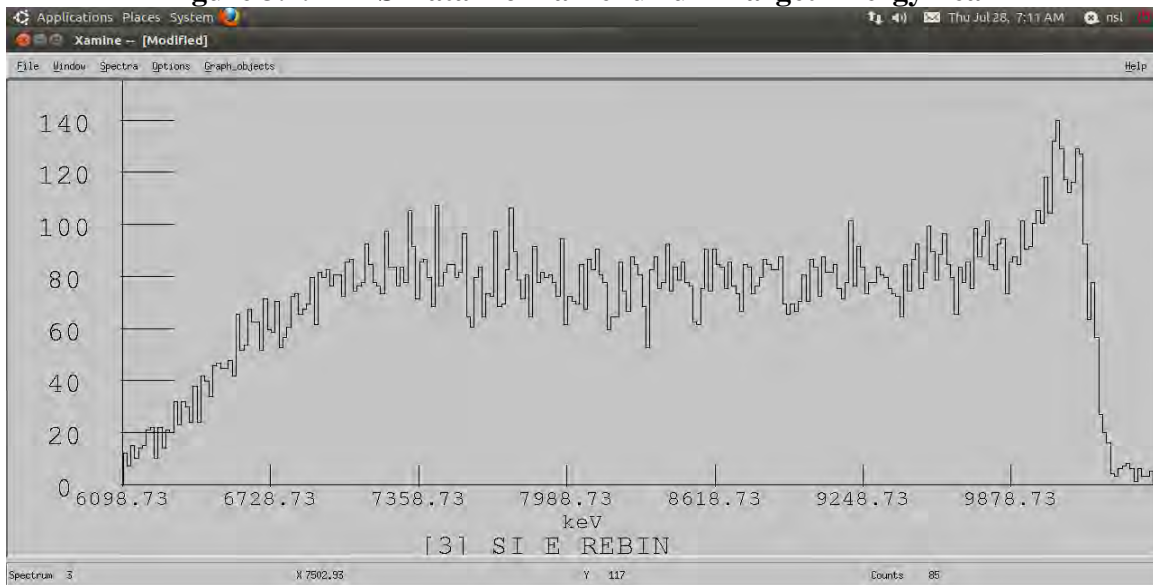


Figure 3.2.2 RBS Data from a Tellurium Target Energy Peak



Integration of the stopping power in $\text{keV}/\mu\text{g}/\text{cm}^2$ for a range of possible target thicknesses was calculated and interpolated to produce a relationship between energy loss and target thickness. Energy loss in the particle collision was calculated using proprietary kinematics software. Of the 14 foils tested, 2 were determined to contain no heavy elements. Additionally, one of the Cadmium target foils was too thick to obtain an

accurate measurement. The isotopic composition of the targets was determined by analyzing the energy at the leading edge of the peak. Two of the targets tested were known to be $^{120}\text{TeO}_2$. Using these foils as benchmarks, the energy signature of each isotope could be determined.

4 Results and Conclusions

The final relevant and adjusted data for all RBS tested targets is shown below in Table 4.1. The hope was that count data from the peaks in PIXE would scale linearly along with the thickness measurements determined through the RBS experiment. The relationship between RBS calculated density and PIXE measured counts for the Tellurium targets is shown below in Figure 4.1.1. Controlling for target backing and framing do nothing to produce a more linear relationship. Further, the different isotopes of Tellurium are not grouped together; although this is not surprising as PIXE is only dependent on the number of protons in the target sample.

Figure 4.1
Density vs Counts

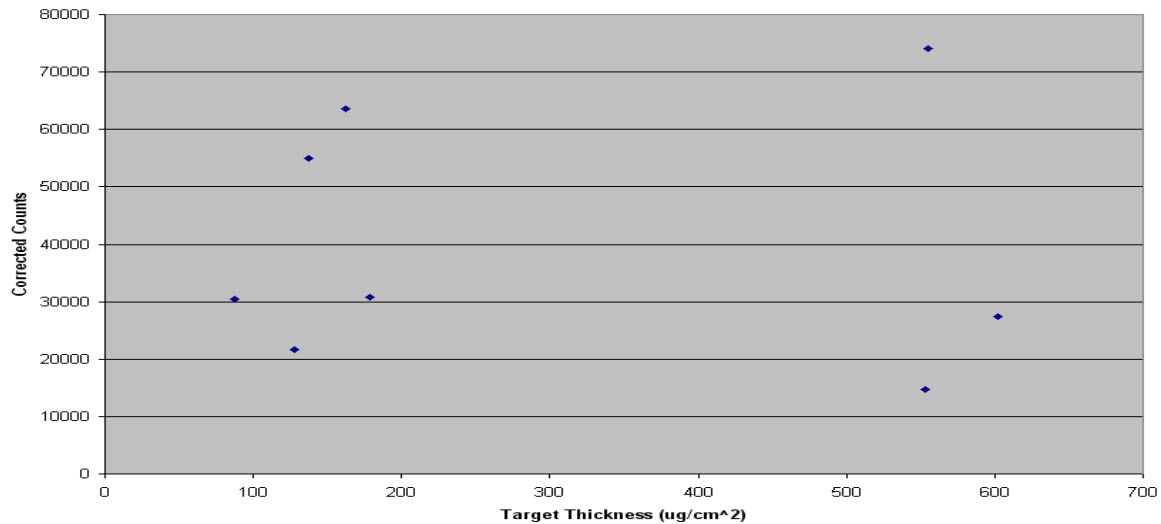


Table 4.1

Target	Composition	Thickness $\mu\text{g}/\text{cm}^2$	Energy Loss kev	PIXE Counts
--------	-------------	--	--------------------	----------------

3A Box					
4	Cadmium	Excess		Unknown	522
25 Box					
1	118SnO2		168	1030	47901
61	120TeO2		128	775	21684
16	120TeO2		555	3428	74146
92 Box					
4	Cadmium		584	3008	148717
10	120TeO2		553	3415	14642
4 Box 2	128TeO2		162	964	63523
3 Box 2	128TeO2		137	814	55026
10 Box					
5	None	Unknown		Unknown	3864
2 Box 2	126TeO2		602	3606	27442
74 Box					
6	124TeO2		179	1091	30764
6A Box					
7	None	Unknown		Unknown	473
13 Box					
5	128TeO2		87	515	30411
5 Box 4	Cadmium		913	4819	152138

It was determined that PIXE is not a reliable method of gathering data on the thickness of thin foil target. Further RBS experiments must be conducted in order to fully characterize each of the remaining 42 targets. However, the 14 RBS tested targets did provide enough data points to move forward in the main experiment. The Tellurium targets were irradiated in order to better determine the half lives of the unstable isotopes of Tellurium. These results can then be used to improve models of stellar nucleosynthesis and the p-process.

This work was supported by the National Science Foundation under contract number PHY0822648.

5. References

1. E. M. Burbidge, G. R. Burbidge, W. A. Fowler, Fred Hoyle (1957). "Synthesis of the Elements in Stars". *Reviews of Modern Physics* 29 (4): 547–650
2. A. G. W. Cameron: *Nuclear Reactions in Stars and Nucleogenesis*. In: *Publications of the Astronomical Society of the Pacific*, Vol. 69, 1957, p. 201-222
3. D. Bohm, *Quantum Theory*, Prentice-Hall, New York, 1951, Chapter 4
4. W. D. Ehmann, D. E. Vance, *Radiochemistry and Nuclear Methods of Analysis*, Wiley-Interscience, Toronto, 1991, p. 347-355
5. W. D. Ehmann, D. E. Vance, *Radiochemistry and Nuclear Methods of Analysis*, Wiley-Interscience, Toronto, 1991, p. 355-363

Correction Methods for Project GRAND Data

Molly Ball

**2011 NSF/REU Program
Physics Department, University of Notre Dame**

Advisor: John Poirier

Abstract

Project GRAND is a cosmic ray experiment located north of the University of Notre Dame. It consists of 64 huts of proportional wire chambers that make up a 100 m x 100 m detector array. These detectors identify muons produced when cosmic rays reach the Earth's upper atmosphere. The muon counting rates remain fairly constant, but this is not the case when there are solar flares and coronal mass ejections. An interesting occurrence called a Forbush Decrease was seen in February 2011 in data from the Oulu Neutron Monitor, a lower energy experiment than GRAND. This was caused by a cloud of charged particles and the magnetic fields moving toward Earth which deflect the path of charged cosmic rays that come from outside our solar system and bombard the Earth's upper atmosphere. GRAND's data was examined and a similar decrease at the same time as Oulu was found along with additional phenomenon not seen by Oulu, which usually sees more structure than GRAND due to its ability to detect lower energy particles more easily affected by solar activity. Several steps, such as looking at pressure correction and good hut corrections, have been taken to correct GRAND's data for non-physics effects. An upper air temperature correction remains to be done as well.

1 Introduction

Project GRAND (Gamma Ray Astrophysics at Notre Dame) is a broad air shower array of proportional wire chambers (PWC) that detect secondary muons. Located directly north of the campus of the University of Notre Dame at 41.7°N and 86.2°W at an elevation of 220 m above sea level, the experiment is made up of 64 stations that are arranged in an 8 x 8 grid. Each station contains four PWC pairs with a detection area of 1.29 m², giving the experiment a total muon detecting yield of 82 m² [1]. Project GRAND runs two experiments simultaneously. One identifies single tracks of individual muons, while the other identifies extensive air showers, which are when multiple stations are hit in a very small period of time [1]. The experiment is most sensitive to primary energies of greater than 10 GeV with a peak sensitivity

at 56 GeV for vertical tracks. This makes Project GRAND ideal for studying high energy particles from cosmic rays.

Each of the four pairs of PWC planes contains one plane with 80 signal wires running east-west and the other plane has 80 signal wires running north-south for a total 160 wires in each chamber. The configuration of these two orthogonal planes is used to measure the angle of a charged secondary muon track to $\pm 0.5^\circ$. All of the pairs of PWC planes, stacked one on top of the other, are separated by 200 mm of space and the bottommost two pairs are separated by a 50 mm thick steel plate that helps to differentiate between muons and electrons. When charged particles move through the detectors, several interactions can occur. If the charged particle is a muon, it will travel in a straight line directly through all of the PWC pairs. If the charged particle is an electron, it will either be completely stopped, start a shower, or scatters when it hits the steel plate. The plate is 96% accurate in distinguishing between muon and electron, but in view of the fact that the number of electrons seen at ground level is only a third of the number of muons that accuracy is closer to 99%.

The PWC chambers are filled with a gaseous mixture of 80% argon and 20% carbon dioxide. When a charged particle like a muon or an electron passes through a chamber, it will ionize the gas and a trail of ions will be left. These ionized particles will move through the chamber and as they do so will collide with other gas molecules. A current is formed on the closest signal wire that is amplified to denote the position of the wire in the chamber therefore the position of the particle.

Identifying the x-value of each wire hit will result in finding the angle of the muon track geometrically.

2 Cosmic Ray Effects

Project GRAND was established to do cosmic ray astrophysics, which investigates particles (or rays) that arrive at the earth's surface from the sun and other galaxies. When cosmic rays hit earth's atmosphere, they collide with air nuclei, typically oxygen or nitrogen, and create secondary particles, such as pions. These pions quickly decay into muons that are able to reach earth's surface to be identified by muon detectors. Project GRAND has the ability to detect rises in ground level muon flux that are associated with powerful solar flares as well as a Forbush decrease which is a rapid decrease in cosmic ray intensity followed by a slower recovery back to the normal muon flux. Forbush decreases are often caused by coronal mass ejections (CME), a massive burst of solar wind, light isotope plasma, and magnetic fields rising above the sun's corona and being released into space. This ejected material consists of charged particles with magnetic fields. Traveling at an average of 500 km/s, CMEs will reach the earth in a matter of days and if the CME is strong, detectors will be able to see the Forbush decrease. The magnetic fields will disrupt the particles heading toward earth and deflect some of the cosmic rays from reaching the atmosphere causing a decrease in cosmic ray detection. Over just a few hours this decrease transpires, but it takes several days for the solar cosmic ray intensity to return to normal.

3 Analyzing Forbush Decrease of February 2011

There were several incidents of activity on the surface of the sun in the month of February, which may be an indication that the sun is coming out of a solar minimum in its normal eleven year solar cycle. The strongest of this activity was a X2 flare on February 15, 2011 with a peak at 1:56 UT [2]. Moving with a speed of about 900 km/s, the CME created by this flare was expected to reach earth's atmosphere early on February 18, 2011. Several different detectors were examined to see if they saw any special phenomenon during this time period. The main detector that was inspected was the Oulu neutron monitor, which identifies secondary particles at a lower primary energy than Project GRAND. This means Oulu would have a better chance of seeing structure due to a Forbush decrease. The plotted data for February 12, 2011 00:00 UT to February 28, 2011 07:00 UT from Oulu can be seen in Figure 1. This neutron monitor saw definite structure in their neutron count with a 4% drop in a couple of hours and a gradual rise back to the normal count which is characteristic of Forbush decreases [3].

After seeing the structure in Oulu's data, Project GRAND's data was examined. The structure seen on GRAND's website seemed to be more dramatic than Oulu. The data for GRAND can be seen in figure 2. GRAND's data needed to be analyzed in more detail to make sure all non-physics effects have been properly taken into account.

4 Correction Methods

When the cosmic rays come into earth's atmosphere, several factors can have an effect on them. The atmospheric pressure is one of the most influential factors on particles moving toward the surface of the earth. When the pressure is high, it takes particles more energy to reach the earth's surface, meaning fewer muons reach the detectors. The opposite effect is true for lower pressure periods. A pressure correction that is completely accurate is essential if the physics of cosmic rays is to be studied. Without a proper pressure correction, the effects of the earth's atmospheric conditions would overshadow the physics. The first check was to verify whether the GRAND's data lab website was doing the pressure correction properly. Several time periods were checked and the conclusion was that the website did not perform the pressure correction accurately. A new program had to be written to correctly handle the pressure correction and pressure corrections can now be made quite easily.

After applying the pressure correction, the data from the February period still showed more structure than that of Oulu so further investigation was necessary. Additional corrections adjust for disabled stations or stations having problems with their counts. There is no simple way to check to see if the program that does this correction is working correctly, so another program was needed to verify this. This new program was written to take dayfiles from Project GRAND and find the stations with the highest counts for each ten-minute period that the experiment records, it would then combine the top four muon counts into a single count. This is not how

the normal correction, known as the “good hut correction” works from GRAND’s data lab website. When a hut has a problem the efficiency goes down, meaning the muon count will decrease. By applying this top four station correction, it is possible to circumvent any problem that might be associated with the good hut correction. A pressure correction could then be applied to the count found by the top four station correction and data that was both pressure corrected and provisional correction for top stations would be available. After completing this step for GRAND’s February data, it was found that it still resembled the original count data that seemed to have too much structure.

5 Other Possible Problems

Although several steps were taken that would lead to a more accurate muon count, there is a great deal of structure still present in Project GRAND’s data and this leads to the notion that there might be more corrections or repairs that need to be done. December 2010 through March 2011 was examined and there was found to be a definite correlation between average daily temperature and muon count. A section of this comparison can be seen in figure 3. At the end of December, there is a sharp increase in the temperature, which corresponds to a decrease in the counting rate. This indicates that a proper temperature correction needs to be performed. This will be something that Project GRAND students will work on in the future. Another potential cause for the structure in GRAND’s data is gas leakage to the stations. This could affect the muon count rate if the gas flow wasn’t at a level it should be and the detector efficiency would be decreased. These are both potential problems that will be examined in order to verify that Project GRAND’s data is accurate.

6 Conclusion

When looking at the activity seen by detectors during the solar active period in the middle of February 2011, specifically a suspected Forbush decrease on February 18, 2011, it was noted that data from Oulu Neutron Monitor in Finland and Project GRAND didn't correspond with each other. The interesting observation that accompanied this was that Project GRAND, a higher energy experiment, saw a significant amount structure that was undetected by Oulu, which typically is able to see more activity due to its lower energy observations. Several methods of correcting the raw data were implemented to try and decipher if the data reported by GRAND's data lab website was accurate and there is still an ongoing effort to establish this. It is necessary to exhaust every possible explanation for the structure seen by GRAND before the data can be viewed as significant cosmic ray activity.

Acknowledgements

I would like to thank my advisor, Dr. John Poirier, for being very helpful and patient as I conducted by research. He made my REU experience very enjoyable as well as enlightening. I would also like to acknowledge the work of Calvin Swartzendruber, Chris Windbigler, and Evan Grimes with helping to maintain the detectors. I would like to thank Chris D'Andrea for his assistance when we struggled to find the next steps to take. Finally, I would like to thank Dr. Garg and the entire Notre Dame Physics Department for making this summer an exciting and educational experience.

References

- [1] J. Poirier, C. D'Andrea et al (2007), Status report on project GRAND, *30th International Cosmic Ray Conference (ICRC)*.
- [2] NASA, <http://www.nasa.gov/>
- [3] Oulu Neutron Monitor, <http://cosmicrays.oulu.fi/>
- [4] NOAA National Weather Service, <http://www.crh.noaa.gov/>

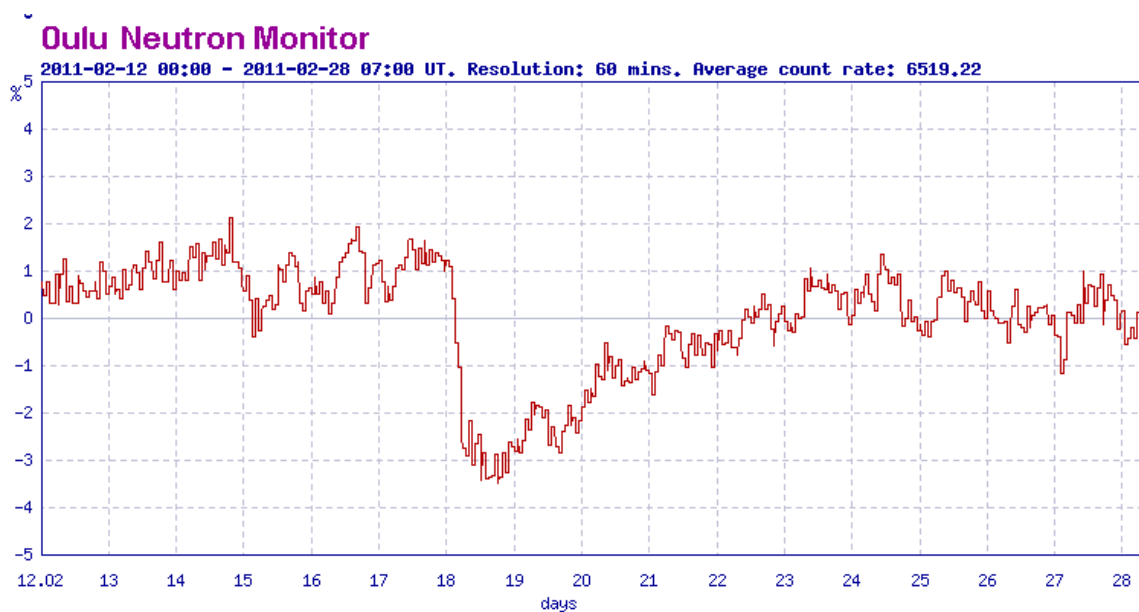


Figure 1: This is the graphical representation of Oulu Neutron Monitor's data. It shows a rapid decrease of about 4% in neutron count at the beginning of February 18 followed by a gradual increase back to normal [3].

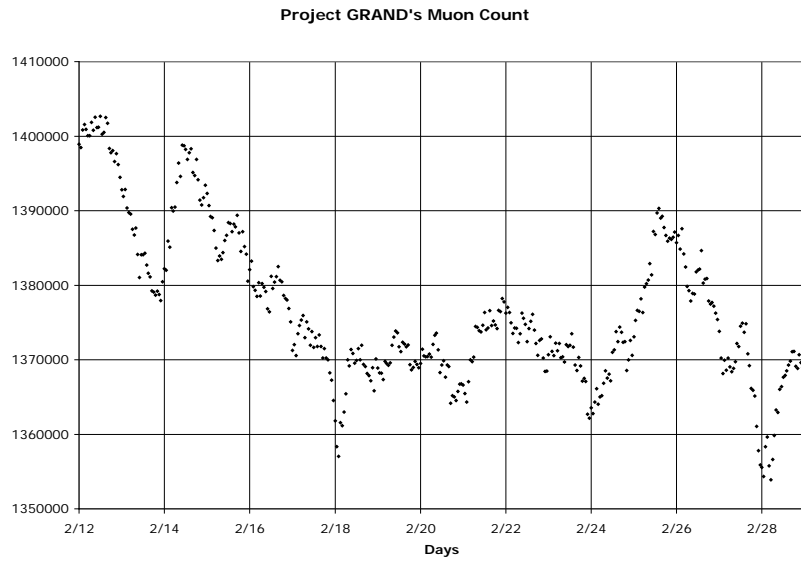


Figure 2: This is Project GRAND's count data after top stations have been selected and after corrections for pressure have been made. It sees a slight drop in count around the beginning of February 18, but it doesn't seem to be as significant as Oulu's data.

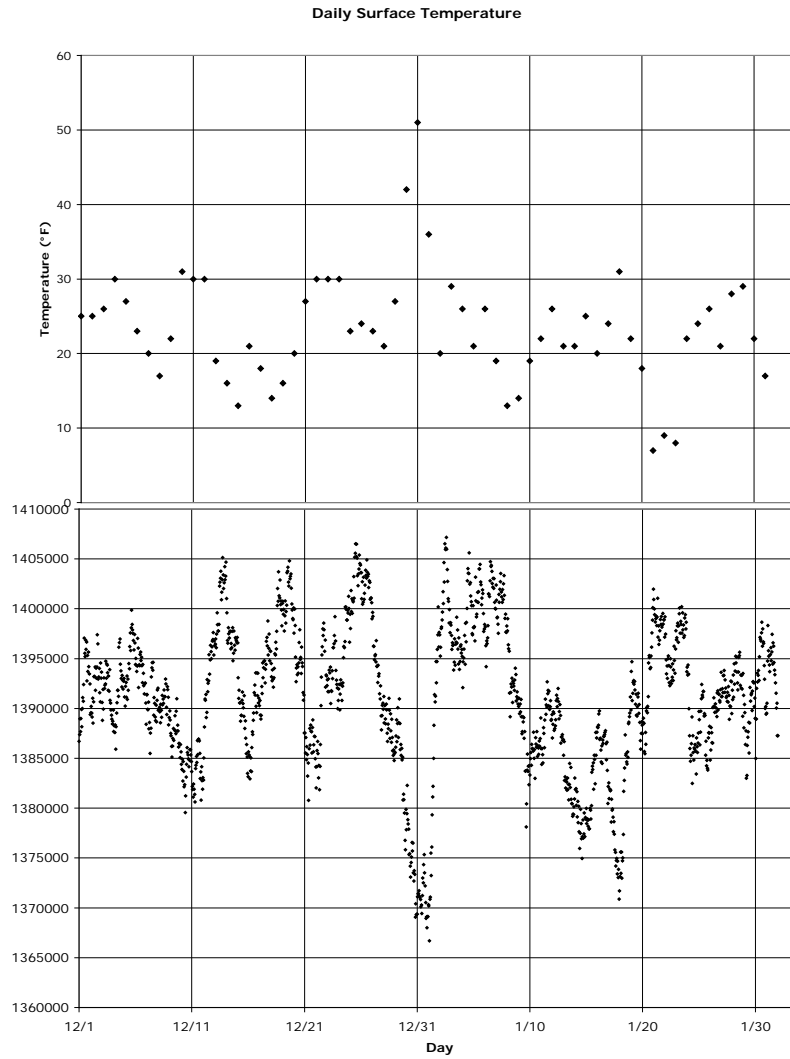


Figure 3: These two graphs show the correlation between surface temperature (top) and GRAND's muon count (bottom) [4].

A Simulated Galaxy Redshift Distribution

Brittany Batman

2011 NSF/REU Program
Physics Department, University of Notre Dame

Advisor:
Dr. Lara Arielle Phillips

Abstract

A link between the observed universe and simulated models of the universe can be made through the large scale structure characteristics of the galaxy redshift distribution. The output of simulated models can reveal a significant amount of information about the universe if the model can be verified and contrasted with observations of the actual universe. Computationally simulating the evolution of the universe results in information about the distribution of dark matter, baryonic gas, and galaxies in a finite volume with periodic boundary conditions. Using the galaxy distribution at different epochs. We distribute the galaxies in a larger space and compute the redshifts in order to create a model that reproduces surveys such as the Sloan Digital Sky Survey (SDSS), among others. The redshift calculation gives a measurement of the time elapsed since the light was emitted.

A computer program was created to manipulate the output from the simulated model's distribution of galaxies. The program we use translates, rotates and shuffles the galaxy distribution then takes computed quantities (galaxy position and velocity) to calculate the redshift. The redshift distribution is then used to create a galaxy redshift catalog similar to the SDSS by imposing survey characteristics, such as magnitude limits in the different observed bands (or portions of the electromagnetic spectrum). This simulated galaxy redshift distribution program will be used to create a bridge between the simulated models of the universe and observations of the universe.

Introduction

Astronomers observed the radial velocities of spiral nebulae through the Doppler-

shift spectral lines, which were thought to be due to random motions. However, Vesto Melvin Slipher at the Lowell Observatory noticed the velocities were not random, but were redshifted, indicating motion away from the Earth. From these observations Slipher continued on to find that 12 galaxies surveyed were moving away from the Earth and therefore redshifted, while the galaxy Andromeda showed a blueshifted spectrum meaning that it was moving towards the Earth. The observations of Slipher led to the conclusion that the galaxies were moving away not only from Earth, but one another as well through the expansion of the universe. Over the period of 1914 to 1925 Slipher was able to measure velocities for 40 galaxies and confirmed that blueshift was much rarer than redshift, drawing the conclusion that most galaxies were retreating from Earth. [Carroll & Ostlie, 1996:1100-1112]

In order to continue studying these motions of the galaxies many surveys of the sky have been done. These redshift surveys measure the apparent velocities of distant galaxies, which give astronomers an estimate of the distance away the galaxies are. From this distance astronomers are able to gain an idea of the levels of structure within the universe as illustrated in the image below taken from the Southern Sky Redshift Survey.

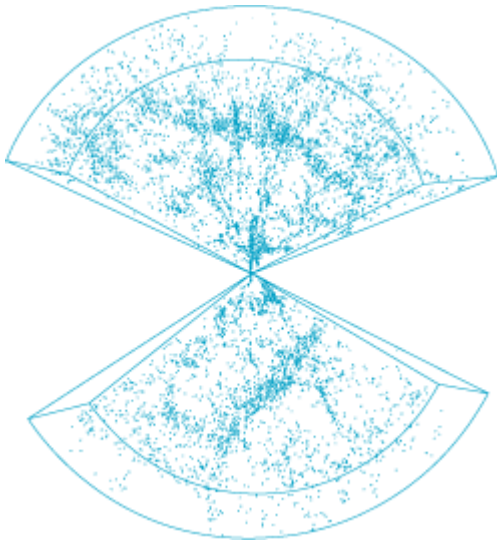


Fig. 1 Large-scale distribution of galaxies in two opposing regions of the sky, as measured by extensive redshift surveys. Each dot represents a galaxy. (From L. N. Da Costa et al., *A complete southern sky redshift survey*, *Astrophys. J.*, 424:L1–L4, 1994)

Considered one of the most ambitious and influential surveys taken in the history of astronomy, the Sloan Digital Sky Survey (SDSS) has obtained images and data of more than 930,000 galaxies and more than 120,000 quasars over eight years of operation. The SDSS uses a 2.5 meter telescope located at Apache Point Observatory in New Mexico and is equipped with a 120-megapixel camera imaging 1.5 square degrees of the sky at a time.¹

We use the data from a large scale hydrodynamical simulation, namely the positions of the galaxies and velocities, to calculate the redshift distribution. [Cen & Ostriker, 1999] We then apply limitations which the SDSS has in order to reproduce a redshift distribution similar to SDSS allowing us to make the connection between our simulated model and the observational universe of the SDSS images.

Galaxy Distribution

We use the multi-redshift galaxy information from cosmological

¹ <http://www.sdss.org/>

hydrodynamical simulations by Cen & Ostriker (1999). The galaxy formation criteria and feedback processes used in the simulation are described in detail in Nagamin, Cen & Ostriker (2000). The chosen cosmology is the “concordance model” described by Wang et al. (2000). A data file containing the coordinates of each galaxy was provided and used to find the distance each galaxy is away from the point at which the galaxy distribution is viewed from. Within the program the galaxy distribution is able to be rotated, randomly shuffled and translated some distance away. The translation allows for the galaxy distribution to be viewed from various distances away, while the rotation of the axes allows a different view of the galaxy distribution. The shuffling permits for the galaxies to move out of the box at one end and with the application of periodic boundary conditions to return at the other end, staying within the limits of the space as shown in figure 2.

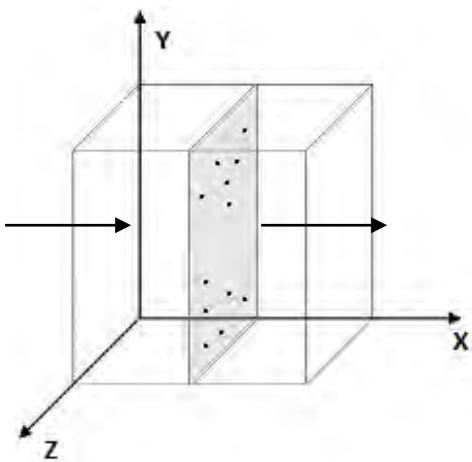


Figure 2

An illustration of the galaxies within a given plane, represented by black dots, the program is able to move planes of galaxies and to rotate the axes from which the box is seen. In addition the program applies periodic boundary conditions to the shuffling to keep all the galaxies within the box limits.

The distance of each galaxy is needed in order to calculate the redshift. The

distance of the galaxy is calculated from a simple distance equation as listed below.

$$r = [x^2 + y^2 + z^2]^{\frac{1}{2}} \quad (1)$$

In order to apply the periodic boundary conditions the shuffling within the program is written so that the shuffling will not put a galaxy outside of the boundary limit, in the case we used the galaxies had to stay within 25 h⁻¹Mpc in the x, y and z direction. Therefore x was defined as follows

$$x = [x_{coord} + value - obs.x] \times factor \quad (2)$$

Where x_{coord} is the coordinate value from the file containing all galaxies coordinates, $factor$ is due to the coordinates of the galaxies being in terms of a fraction of the box size, $value$ is a term associated with the shuffling motion, which was a random number generator, and $obs.x$ is a term associated with the translation of the galaxies. Similar to the x value, the y value and z value are as follows.

$$y = [y_{coord} + value - obs.z] \times factor \quad (3)$$

$$z = [z_{coord} + value - obs.y] \times factor \quad (4)$$

The position in the sky of the galaxies was used to limit the galaxy distribution to match the SDSS conditions and was calculated as listed below.

$$\theta = \tan^{-1} \left[\frac{z}{[(x^2 + y^2)^{1/2}]} \right] \quad (5)$$

$$\phi = \tan^{-1} \left[\frac{y}{x} \right] \quad (6)$$

Redshift Calculation & Interpolation

Two methods of interpolation were used with the galaxy distribution to find the redshift from a distance to redshift conversion table that reflects the “concordance model”. The first method used was a simple linear interpolation created in a spread sheet using the distances generated from the galaxy distribution

and a redshift table that contains distances and the redshift associated with that distance. This calculation was not applied across all 2097 data points within the galaxy distribution since it was used only as a method to check the other interpolation scheme used.

The other method of interpolation was a linear interpolation as well, but a c program was written to use the redshift table and interpolate the values from the galaxy distribution with the appropriate points, the nearest two points in the redshift table. This task proved to be a challenge as two interpolation schemes were attempted to be implemented, but could not handle the input of the large arrays. Therefore an interpolation scheme was written based off the algorithm described in *Numerical Analysis* by the Neville's iterated interpolation. [Burden & Faires, 2010:3.1] The program uses equation 7, which was adapted from Neville's iterated interpolation:

$$Q_{i,j} = \frac{(x - x_{i-j})Q_{i,j-1} - (x - x_i)Q_{i-1,j-1}}{(x_i - x_{i-j})}$$

And the interpolation scheme used in the program:

$$z' = \frac{(r' - r_{less})z_{greater} + (r' - r_{greater})z_{less}}{r_{greater} - r_{less}} \quad (7)$$

Where r' is the distance calculated from the galaxy distribution (equation 1) and z' is the redshift corresponding to the distance. The r_{less} and $r_{greater}$ are the distances such that:

$$r_{less} < r' < r_{greater} \quad (8)$$

And similarly the z_{less} and $z_{greater}$ values are defined as:

$$z_{less} < z' < z_{greater} \quad (9)$$

The c program is able to isolate the terms above so that the linear

interpolation is only across those two points instead of the whole array, which was the challenge with other methods attempted. The program then created a comma-separated-values (csv) file that contained the distance, θ , ϕ and the redshift. This csv file was then cross referenced with the spread sheet interpolation to ensure the program ran properly and correctly.

In addition to the redshift found from the linear interpolation scheme, there is a redshift associated with the particular velocity of the galaxy. The redshift associated with the velocity produces either a redshift, the galaxy is moving away from the observer, or a blueshift in which the galaxy is moving towards the observer. [Carroll & Ostlie, 2007:98] This was found from the velocity along the line of sight of the particular galaxy as follows.

$$Z = z + \frac{v}{c} \tag{10}$$

Where Z is the total redshift, z is the redshift value from the interpolation, and the last term is the velocity along the line of sight of the galaxy divided by the speed of light.

Redshift Distribution and SDSS

In order for the redshift distribution of the simulated model to be similar to the SDSS there were various limits that were applied. These limits, found from the SDSS Constants table, must be applied since the computer produces all data points while observable data would have limits due to the technology used and by the fact that we can only visibly see parts of the electromagnetic spectrum whereas the computer would be able to produce data of all parts of the electromagnetic spectrum. In addition, the SDSS covers a limited area in the sky while the simulation has no such limits on the area of the sky it does calculations on. The area mapped

for SDSS was limited by η and λ , which are respectively the survey latitude and longitude limits and mapped in terms of stripes. [Strauss] The program will need to convert the position, so that the area mapped by the stripes in the SDSS can be applied to the simulation.

The next step for the program will be to implement a calculation of the magnitude using the luminosities available for the galaxy distribution through the following equations.

$$F = \frac{L}{4\pi r^2} \tag{11}$$

Where F is the radiant flux measured at a distance r (already obtained previously in the program) and L is the luminosity of the object.

$$\frac{F_2}{F_1} = 100^{(m_1 - m_2)/5} \tag{12}$$

Where m is the apparent magnitude of the object and the subscripts are used so that the flux and magnitude have some object compared to them.

These calculated magnitudes from the galaxy distribution would then be limited just as θ and ϕ were based off the SDSS Constants table, part of which is listed below.

Filter name	Limiting magnitude
g-green	23.3
i-near infrared	22.3
r-red	23.1
u-ultraviolet	22.3
z-infrared	20.8

Conclusions

The program successfully calculates the redshift from the interpolation of the redshift table along with the redshift due to the velocity of each galaxy within the distribution. This creates a redshift distribution similar to the SDSS and the program applies the conditions of the SDSS to the simulated redshift distribution. The next step towards verifying the simulated galaxy distribution will be to implement the limiting magnitude conditions within the program.

Acknowledgements

I would like to thank my advisor, Dr. Lara Arielle Phillips, for allowing me the opportunity to work on this project. I would also like to thank Ali Snedden for all the help he provided. I would finally like to thank Dr. Umesh Garg and the University of Notre Dame Department of Physics for the opportunity to research with such exceptional researchers, students and staff.

References

- Burden, Richard, & Faires, J. (2010). *Numerical Analysis*. Boston, MA: BrooksCole Pub Co.
- Carroll, Bradley W., & Ostlie, Dale A. (1996). *An Introduction to Modern Astrophysics*. Benjamin-Cummings Pub Co.
- Carroll, Bradley W., & Ostlie, Dale A. (2007). *An Introduction to Modern Astrophysics*. San Francisco, CA: Benjamin-Cummings Pub Co.
- Cen, R., & Ostriker, J. P. 1999, ApJ, 514, 1
- Nagamine, K., Cen, R., & Ostriker, J. P. 2000, ApJ, 541, 25
- Sloan Digital Sky Survey. (2011, May). SDSSConstants. from SDSS.
- Strauss, Michael. *et al.*, 2003, Sloan Digital Sky Survey. *Great Circle Drift Scanning*.
- Wang, L., Caldwell, R. R., Ostriker, J. P., & Steinhardt, P. J. 2000, ApJ, 530, 17

Numerical Methods in Quantum Field Theories

Christopher Bell
2011 NSF/REU Program
Physics Department, University of Notre Dame

Advisors: Antonio Delgado, Christopher Kolda

1 Abstract

In this paper, preliminary results from investigation into the formalism of Quantum Field Theory as well as various numerical techniques used to approximate theoretical models will be presented. First, the two equations of primary interest, the Klein Gordon and Dirac equations, will be introduced and examined for underlying mathematical and physical structure. In the next section, a naive approach to transforming the differential equations into difference equations will be used and their limitations will be discussed. We will then proceed to investigate methods of preserving discrete forms of the continuous symmetries these equations hold. Finally we will discuss how these methods can be combined together in ways that can balance the need for numerical methods to both well approximate the system as well as preserve the symmetry of the equations.

2 Introduction

The formulation of Quantum Field Theory succeeded in unifying Quantum Mechanics with Special Relativity in a very satisfying way. While the subject is nowhere near complete, the interactions described with QFT explain observed behavior so naturally it is impossible to deny its computational ability. However, while the theory allows us to write down very elegant descriptions of how particles with internal degrees of freedom (spin) interact with each other through the Strong, Weak and Electromagnetic Forces, the process of actually calculating values that are physically observable becomes complicated very quickly because the corresponding integrals have no closed form solution. The physicist must truncate an infinite series at some point to begin making a calculation. These approximations can be carried out to arbitrary precision, but this is not the only issue. Ignoring the common divergences that physicists encounter in these approximations, there is the

issue of practicality. It does not make sense to carry out these calculations by hand when a computer can do them exponentially faster. However, a very large sacrifice is made when computation is left to a computer because it only has the ability to add and multiply. Binary cannot represent $\frac{1}{10}$ without truncating an infinite sequence, so the reduction of a very complex integral equation to a series of arithmetic operations is not a trivial process.

3 Klein-Gordon and Dirac Equations

We begin by stating the two primary field equations of interest¹.

Definition 1 (Klein-Gordon Field). *Let $\phi(x) = \phi(\vec{x}, t)$ be a real valued scalar field satisfying the Lagrangian density*

$$\mathcal{L} = \frac{1}{2}(\partial_\mu\phi)^2 - \frac{1}{2}m^2\phi^2$$

Then ϕ is called the Klein-Gordon field satisfying the Euler-Lagrange equation

$$\partial^\mu\partial_\mu\phi + m^2\phi = 0$$

This will be our first relativistic wave equation to consider. As a scalar field it describes the motion of a neutral spin 0 particle who is it's own antiparticle. If we were to modify it to be complex valued the real and imaginary parts would correspond to a particle-antiparticle pair with opposite

¹Throughout the text the metric signature $(+,-,-,-)$ will be used. Also $\hbar = c = 1$

charges.

Before defining the next field of interest, we define a mathematical object vital to working with the field.

Definition 2 (Lorentz Algebra). *Let γ^μ be 4 $n \times n$ matrices satisfying the anti-commutation relations*

$$\{\gamma^\mu, \gamma^\nu\} = 2g^{\mu\nu} \times 1_n$$

Then we have an n -dimensional representation of the Lorentz algebra given by these four matrices from the commutation relations

$$S^{\mu\nu} = \frac{i}{4}[\gamma^\mu, \gamma^\nu]$$

The elements of the Lorentz algebra satisfy the following commutation relations

$$[S^{\mu\nu}, S^{\rho\sigma}] = i(g^{\nu\rho}S^{\mu\sigma} - g^{\mu\rho}S^{\nu\sigma} - g^{\nu\sigma}S^{\mu\rho} + g^{\mu\sigma}S^{\nu\rho})$$

In the case of $n = 4$, the γ^μ matrices are the Dirac matrices. Their particular representation will be specified later. With these in mind, we proceed to the next field under consideration.

Definition 3 (Dirac Field). *Let ψ be a 4 component field that transforms under boosts and rotations according to the Lorentz algebra (called a Dirac spinor). Let ψ satisfy:*

$$(i\gamma^\mu\partial_\mu - m)\psi(x) = 0$$

This is the Dirac equation. To describe the Lagrangian of the Dirac Field, first define:

$$\bar{\psi} \equiv \psi^\dagger \gamma^0$$

the so called Dirac adjoint. With this, the Lorentz invariant Dirac Lagrangian is

$$\mathcal{L}_{Dirac} = \bar{\psi}(i\gamma^\mu \partial_\mu - m)\psi$$

This field describes a spin 1/2 particle and its corresponding antiparticle. A solution to the Dirac Field equation is automatically a solution to the Klein-Gordon equation, but not vice versa.

These two fields give us the foundational tools to describe the interactions of relativistic quantum systems. It should be noted that both equations have solutions with negative energies, which was initially seen as a weakness of the theories. Reinterpretation of those solutions as particles corresponding antiparticle resolved those issues. Of course, it is inaccurate to say these two fields describe particles at all, because we have not quantized them yet. When the quantization procedure is carried out, care must be taken to apply appropriate commutation relations. Specifically, for the Dirac Field we must impose anti-commutation relations to preserve causality and to explain the negative energy solutions in terms of antiparticles.

One final thing to make note of with these equations is the conserved energy norm. Because solutions to the Dirac equation are automatically solutions to the Klein-Gordon equation, it is sufficient to just show the conserved norm

for the Klein-Gordon equation. To do this, we define a quantity called the energy

$$E(t) = \int_{\mathbb{R}^n} \left| \frac{\partial \phi}{\partial t} \right|^2 + \left| \frac{\partial \phi}{\partial x_1} \right|^2 + \left| \frac{\partial \phi}{\partial x_2} \right|^2 + \cdots + \left| \frac{\partial \phi}{\partial x_n} \right|^2 dx$$

And for our solution $\phi(\vec{x}, t)$, the energy should be conserved (i.e. $E(t) = E(0) \forall t$). This quantity is important in its own right, because it allows us to define a topology on the space of solutions to the Klein-Gordon equation. Any approximation should then have a discrete conserved energy norm in order to recover the structure of the continuous solution.

4 2nd Order Finite Difference Method - A Careless Attempt

To begin, we consider the Klein-Gordon equation in (1+1) dimensions:

$$(\partial_t^2 - \partial_x^2)\phi(x, t) + \phi(x, t) = 0$$

There are several conditions that we must impose to effectively translate this differential equation to a difference equation. The first is that we must restrict the equation to some finite region. For simplicity, we will consider a box of side length L and partition it into n equal sized intervals. In other words, $\Delta t = \Delta x = L/n = h$. Additionally, boundary conditions must be specified so that the value of the field is known along the $x = -h$ and $x = L + h$ lines. Again, we strive for simplicity and make the field equal to zero everywhere

outside of the box. Finally, we specify an initial condition $\phi(x, 0) = f(x)$. With these conditions it is quite simple to formulate a discrete approximation to our field. To evaluate the $n+1$ -th time step at the k -th spacial step:

$$\phi(kh, (n+1)h) = (\phi((k+1)h, nh) + \phi((k-1)h, nh)(1 - h^2/2)) - \phi(kh, (n-1)h)$$

This difference equation came out nicely because we assumed the step size for the time and spacial steps were equal. In general, we also need to know the value at the k -th and n -th step as well. This formulation's error is second order in both time and space, so by taking smaller step sizes, the error decreases quadratically.

However, there is a glaring issue with this approach, we treated the equation classically and non-relativistically. Even for the simple case of the Klein-Gordon Field, we must affix harmonic oscillators at every point in space. By specifying a finite region, we ensured that our eigenfunctions would have a discrete spectrum, but we did nothing to ensure these eigenfunctions satisfy relativistic constraints, nor did we consider the fact that there is a countably infinite basis of eigenfunctions. We also failed to treat $\phi(x,t)$ as an operator. It should be obvious then that more care is needed to apply numerical methods for quantum fields.

5 A Second Attempt

From the last section, it is now obvious that the equation of motion of a field is not the correct thing to consider. This is obvious when the importance of the Lagrangian in Quantum Field Theory is recognized. We are ultimately interested in describing interactions among particles and calculating scattering cross sections and probability amplitudes. To return to the Klein-Gordon equation, let's consider the true form of our field:

$$\phi(\vec{x}, t) = \int \frac{d^3p}{(2\pi)^3} \frac{1}{\sqrt{2E_{\vec{p}}}} (a_{\vec{p}} e^{-ip^\mu x_\mu} + a_{\vec{p}}^\dagger e^{ip^\mu x_\mu})$$

From here it is obvious that ϕ should act on state kets. If we want to calculate the amplitude for a particle to propagate between two points we must evaluate:

$$D(x - y) = \langle 0 | \phi(x) \phi(y) | 0 \rangle = \int \frac{d^3p}{(2\pi)^3} \frac{1}{\sqrt{2E_{\vec{p}}}} e^{-ip^\mu (x_\mu - y_\mu)}$$

We now begin to touch on the heart of the matter. Calculations in Quantum Field Theory are not differential equations, they are integral equations. Attempting to apply numerical techniques to the equations of motion for the Klein-Gordon and Dirac fields will give solutions that are difficult to interpret and possibly nonphysical and probably nonsense.

6 A Solution and Applications

We have avoided the functional integral until now, because it is not the most obvious approach. Of course, by prioritizing the Lagrangian over the Hamiltonian, we move away from the more familiar grounds of Quantum Mechanics, and so the picture becomes less algebraic and more analytic. However, it is undeniable that the path integral formulation makes concerns about preserving symmetry and Lorentz invariance much less of an issue. The reason this method was not considered from the start stems from a numerical standpoint. Solving an integral equation is more involved than a differential equation and is substantially more computationally intensive. This approach does allow for many different techniques to be applied and allows us to delay the need to discretized any equations, or at least to work with semi-discrete equations. Additionally, by working with integral equations we no longer work with point by point evaluation, but with the construction of explicit functions that both well approximate the equation and are easier to work with. In short, this approach trades ease of computation for flexibility.

The flexibility of integral equations comes from the two radically different methods of evaluating the integral. Using the power of Stoke's Theorem, we can change the type of integral from surface to volume or vice versa, depending on the nature of the integrand. We could also construct a weak solution using functional analysis. This variational method has been successfully applied to Atomic Physics and could be quite useful for examining the bound

states of elementary particles.

7 Conclusion

This paper represents the preliminary investigations into how systems in Quantum Field Theory can be numerically evaluated. It is evident that the restrictions quantization and relativity put on the equations make a consistent and accurate numerical approach complex. Further investigation will be made into how successfully numerical schemes can be constructed for the path integral formulation of Quantum Field Theory. In doing so, methods of transforming continuous symmetries into discrete ones will be explored to see if the approximations made for the integral equations retain any sort of symmetry.

References:

W.R. Johnson, S.A. Blundell, and J. Sapirstein, *Phys. Rev. A* **37**, 2 (1988).

M. Peskin and D. Schroeder, *An Introduction to Quantum Field Theory* (Westview Press, 1995).

L. Schumaker, *Spline Functions: Basic Theory* (Cambridge University Press, Cambridge, 2007).

J.J. Sakurai and S.F. Tuan, *Modern Quantum Mechanics* (Addison-Wesley, 1994).

Pt-Ir Tip Etching Techniques for Scanning Tunneling Microscopy

Anna Czerepak

2011 NSF/REU Program

Physics Department, University of Notre Dame

Advisor: Dr. Morten Ring Eskildsen

Abstract

Superconductors have gained significant attention in the last decade. Understanding the properties of superconducting materials is a critical step both in the field of condensed matter physics and the next advances in engineering. Our group sought to investigate the topic of magnetic vortices in Type II superconductors through low-temperature, ultra high vacuum scanning tunneling microscopy. An important component of a successful STM image is the quality of the tips used in the microscope. Two platinum iridium tip-making methods were tested: the Argonne method and a variation on a method introduced in a paper by Lindahl et al^[1]. Sample images taken on an open-air STM by Professor Kandel's group in chemistry, as well as electron microscope pictures of the products of the two tip-making procedures are included and discussed.

1 Argonne Method

The idea behind the Argonne method is to use a two-step chemical etching setup (coarse etch then fine etch/micropolishing) in order to shape the tips. The advantage of this two step method is the short preparation time (less than 20 minutes per tip) and decent control over tip shaping. Some papers advocate a one-step coarse etch instead of the additional micropolishing step. However, various factors in the coarse etch step make any fine control or observation of the tip difficult, including the rapidity of the reaction and wide range of etching times that vary with voltage, length of wire in solution, and even the chemical batch of calcium chloride used to make the solution. The opacity of the precipitate that is produced also makes it difficult to judge the progress of the etching. It is these uncertainties that make single-step coarse etching of tips usually unreliable, especially because the end of the wire breaking off tends to produce tips with ball-shaped ends. This feature is necessary for a sharp result from fine-etching but detrimental to immediate use as a STM tip.

A note on the cut-off time (the time between when the end of the wire drops off and the time when the power to the etching setup is shut off); it is advantageous to minimize this time as much as possible. A longer cut-off time will result in the tip being etched after the desired shape has been obtained. This leads to blunt tips and destroys the ball at the end of the tip. Some groups propose building an automatic cut-off circuit in order to minimize the cut-off time, but it was found that these cut-off circuits still had a significant delay (500 ns at minimum, but usually on the order of milliseconds). This is an improvement on manual shut-off times but the desire to finely control the last stages of this etching is what motivated the alternate approach in section 2 of this paper. If a manual shut off is used, the sound that the reaction produces can be used as a rough guide to determine when etching may be close to completion, with a noticeable decrease in volume when the end of the wire is about to break off.

1.1 Procedure

1. Cut a clean piece of 0.25mm diameter Pt-Ir wire with wire cutters about 12-15mm long.
2. Insert the wire into the copper clips attached to the coarse etching setup. Make sure the wire protruding is as close to vertical as possible in order to ensure that the etched mass on the end falls off cleanly and without bending the tip.

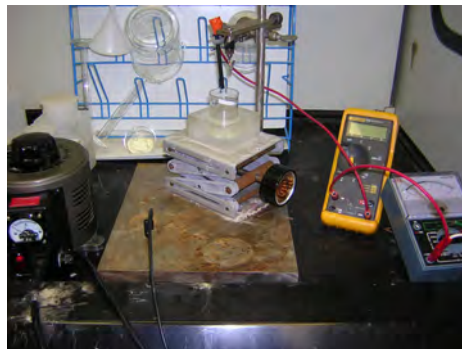


Figure 1: Coarse etching setup showing: AC powder supply, multimeter, voltmeter, copper clip, carbon counter electrode, and stand with solution beaker.

3. Fill the beaker with 30-40ml of 1.5M calcium chloride.
4. Lower the wire into the solution, making sure that the amount of wire in the solution is no less than 1.3mm and no more than 2mm. ¹
5. Set the power supply to 35 V AC and start the timer.² A rough guide to the steps and the duration is provided below, but it will vary, depending on the setup. It must be kept in mind that it is advantageous for the etch to finish on the lowest voltage, as this produces a finer tip shape. It is acceptable to decrease the time of steps one and two, but it must be kept in mind that the subsequent stage times will be longer the shorter the time spent on higher voltage steps.

Voltage Setting	Etching Time
35 V AC	~90 seconds
30 V AC	~45 seconds
28 V AC	Until process is complete

6. Lower the beaker and solution and carefully extract the tip from the copper clip, being careful not to touch or knock the etched end. The solution can be used up to four times, but was discarded after two in our setup, as it became difficult to determine how much of the tip was in the solution when much precipitate was present. Clean and dry the tip using the following steps, being careful to immerse the tip cut-end first and to hold the etched end facing down when it is placed under running water in order to preserve the tip shape.

- Immerse in deionized water for 10 seconds.
- Rinse under hot running water for 2 minutes.
- Immerse again in deionised water for 20 seconds.
- Dry with nitrogen gas.

7. Secure the tip in the fine etching setup and wet the tungsten loop with calcium chloride solution. The solution will need to be replaced frequently, as precipitate builds up rapidly and the available chloride ions are depleted.

8. Set up the electronics for fine etching. This setup is described in detail in the Argonne procedure paper^[2], but it consists most basically of an AC power supply set to about 2.5 V AC³, a switch box with a button to apply current, and a multimeter to verify the voltage. A microscope stage was modified to hold a copper clip to hold the tip in place, a platform to mount the tungsten loop and an additional two-way adjustable stage in order to easier position the loop in relation to the fixed position of the clip.

¹It was found that less than 1.3mm led to the entire end of the wire being etched off, with no 'neck' that was thinned and eventually broken off. More than 2mm was found to deform the tip after the drop off. This is speculated to be due to the increased weight and bulk of the end that forces the drop off to occur sooner, when the neck of the wire is not as thin, and strains the wire. Around 1.5mm was found to be a good length for this step.

²AC power is absolutely necessary, as DC power will not circulate the chloride ions around the wire as much as AC power will. This will result with an etching time on the order of hours instead of minutes.

³It may be tempting to use voltages of 10 V or above in order to speed the fine etch. However, around 10 V or higher, the small amount of solution in the loop is used up very quickly and must be replaced a few times every minute. Voltages higher than 15 V were found to lead to rapid bubble formation in the loop and give blunt tips. It is therefore advisable to restrict voltages for this step below 10 V.

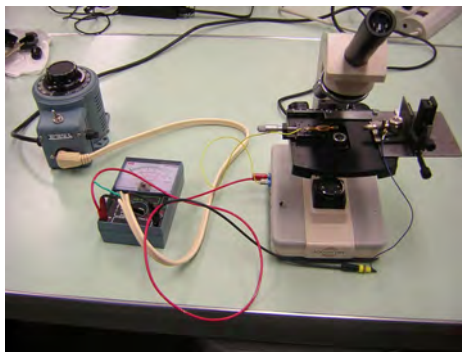
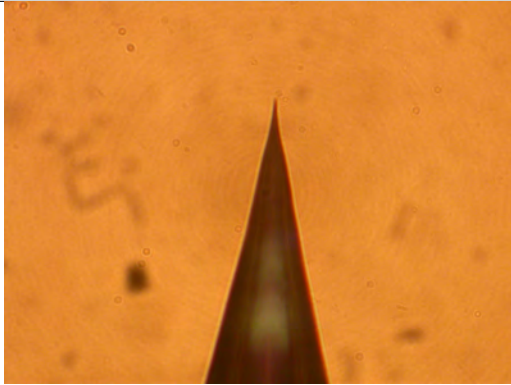
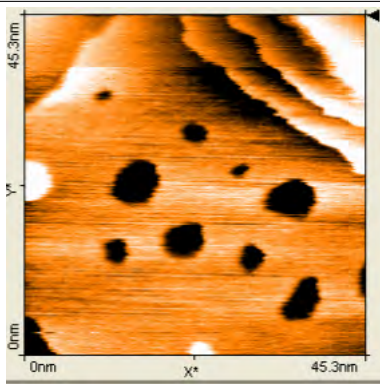
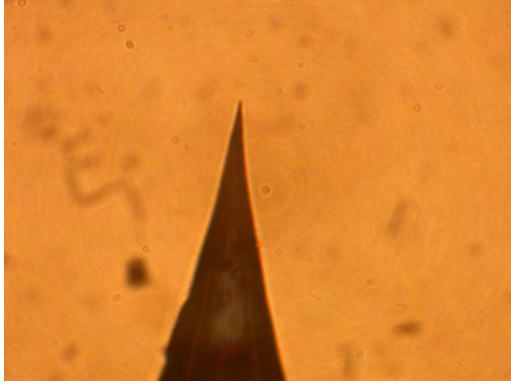
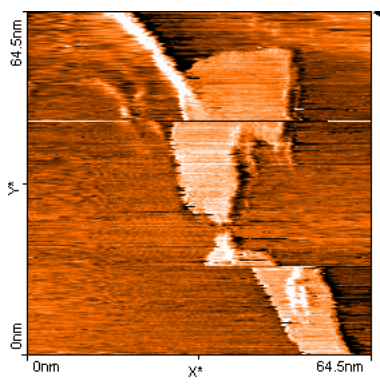
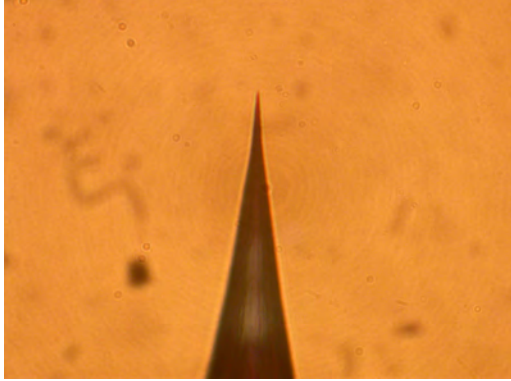
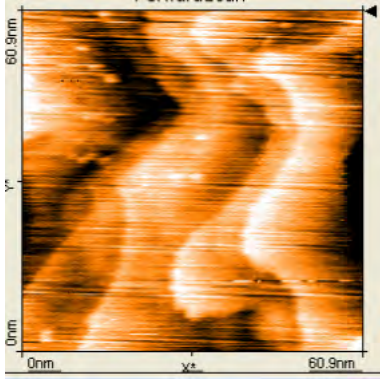


Figure 2: Fine etching setup, showing voltmeter, AC power supply, modified microscope, stage, tungsten loop, and copper clip.

9. Align the tip with the center of the loop. Position the loop behind the ball on the end of the tip, and pull the loop back slowly while pressing the switch box. It is important to apply the power in ONE direction only for proper tip shaping.
10. This process is repeated (changing solution as necessary) until the section of wire just behind the ball is thinned enough to be etched away, leaving a very sharp tip with no ball or other tip anomalies.
11. The tip is cleaned again, using the same procedure as outlined in step 6 and placed under an optical microscope for characterization and cataloging.

1.2 Tips and Resulting Images

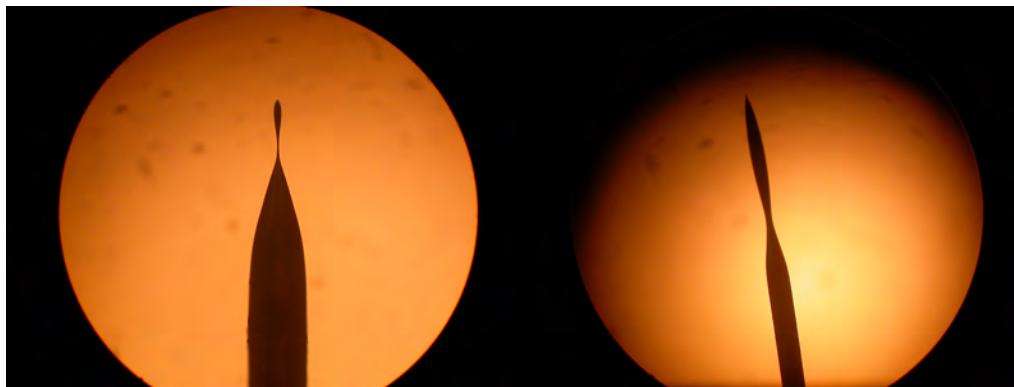
Tip Number/Operator/Sample	Optical Pictures (400x)	Open-Air STM Images
#5/Chris/Octanediol on gold		
#8/Guido/Octanediol on gold		
#9/Chris/Octanediol on gold		

1.3 Discussion

One immediately obvious feature of this experiment is that tip grading by an optical microscope is very difficult. No good measurement of sharpness can be made at 400x magnification and all three tips look roughly the same in terms of apex shape. The optical microscope pictures are best used as a method to check tips for obvious deformities or crashes. However, tip #5 produced the best images by far and no anomalies occurred in either stage of its preparation. Tip #8 had an average quality fine etch and produced a good image, despite the discontinuity in the middle third of the picture. Tip #9 had a slightly longer cut-off time than recommended but still managed to produce a reasonably coherent image at 60.9nm. It can be concluded that the Argonne method produces good tips when the procedure works and has some resilience against minor errors in tip preparation.

2 Experimental Method

The prime motivation behind the experimental method was inspired by a paper published by Lindahl et al^[1]. In it, a method of etching is outlined that stops the coarse etch just before the end of the wire drops off, bends the wire 90° and then continues the etch in sulfuric acid and then does some amount of micropolishing. Their method was found to be unworkable for our group (the bending of the wire did not seem to have a purpose and the entire process was very labor intensive) but the idea of stopping the coarse etch earlier was incorporated into our experimental tip procedure. The idea behind this inclusion was to stop the etching when the neck of the wire is thin and close to dropping off, but finish the etching in the micropolishing setup under a microscope.



Figures 3a and 3b: (L) Properly etched tip, showing a thinned neck section. (R) Improperly etched tip with a thick neck and very large bulk section on the end.

In this way, there is no possibility for over-etching through long cut-off times in the rapid coarse etching step. Tip shaping is finished in the fine etching stage, where the voltage is much lower, the control finer, and there is more influence on the final tip shape. Additionally, the progress of the tip shaping can be seen easily under the microscope, unlike the coarse etching setup. The disadvantage of this method is that it is difficult to stop the etching late enough so that enough of a neck is formed to be easily etched away (if the thinned sections not sufficiently small compared to the tip shank, the etching will not progress correctly and will lead to a blunt tip) but early enough so that the end does not drop off or become so thin that the end section bends and deforms during cleaning or micropolishing. With practice, it is not difficult to tell when etching should be stopped. Our group relied on sound (the fizzing of the reaction will taper off just before it is done) and monitoring the current. When the current dropped to 10-20% of its initial value, the etching was almost complete and the power was shut off.⁴

There is one problem that will be explored in the future and that was the issue of the neck of the tip bending when pulled through the wire loop in the fine etching step. This bending is believed to be caused by the surface tension of the solution in the loop. This could be solved by dabbing some of the solution in the loop away with a piece of paper towel, leaving a film instead of a droplet in the loop, or with a slightly larger loop. The tips produced by this method were the sharpest our group has produced (despite the bend in the tip apex) and show great promise as STM tips if a better method of preventing the strain on the neck of the wire in the last step could be found.

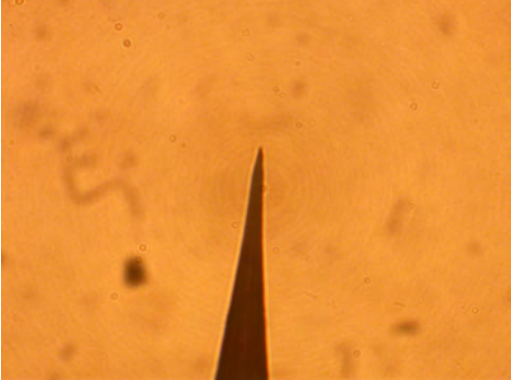
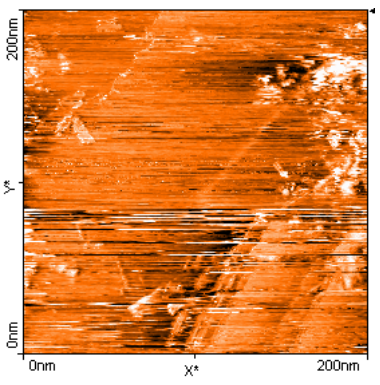
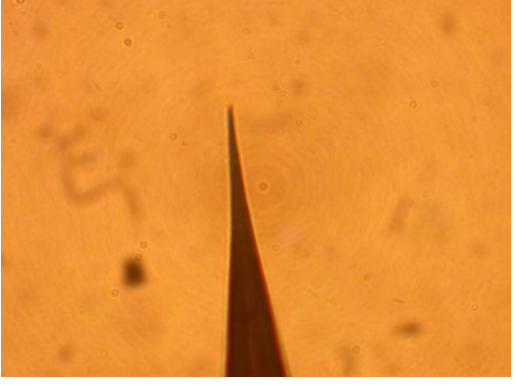
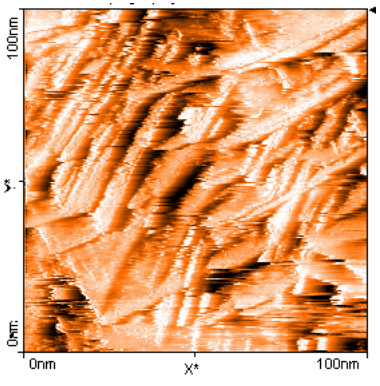
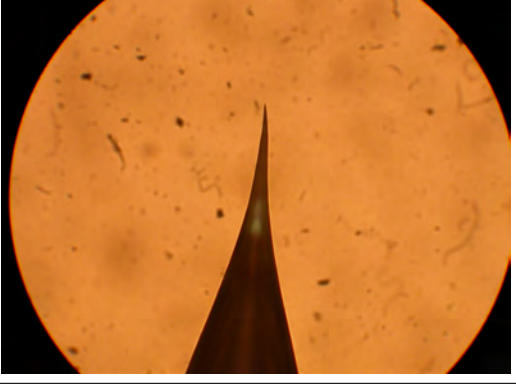
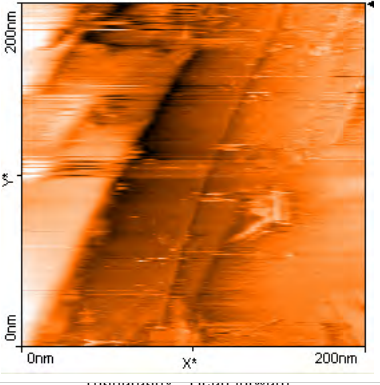
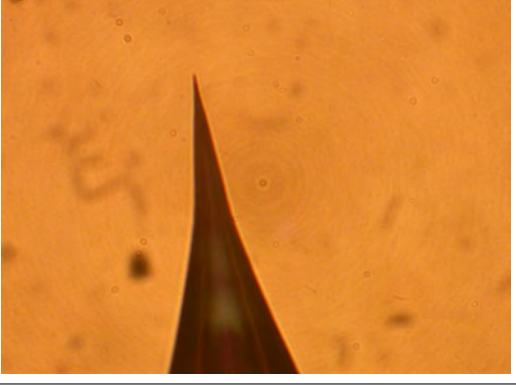
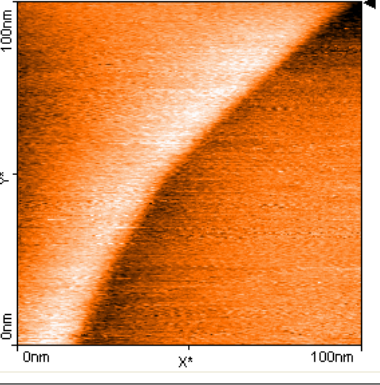
⁴It should be noted that the current does not decrease uniformly to zero as the reaction finishes. Our group found that it reached a finite value at about 10% of the initial value and then discontinuously fell to zero when the end of the tip dropped.

2.1 Procedure

1. The experimental method follows the same steps 1-4 as the Argonne method outlined in section 1.1.
2. Set the power supply to 35 V and start the timer. The time table for this step is the same as step 5 in section 2.1, with the important exception of cutting the reaction short just before the end of the wire breaks off.⁵
3. Clean and dry the tip as in step 6 in section 1.1, being careful when handling the tip, as the end of the tip is quite prone to bending.
4. Insert the tip into the optical microscope micropolishing setup and dip the loop in the 1.5M calcium chloride solution. Dab off some solution with a Kimwipe such that a thin film is left in the loop instead of a droplet.
5. Move the loop onto the wire behind the thinned section.
6. Draw the loop off of the wire while holding the switch button. It is not necessary to draw the entire loop past the neck of the wire each time, as the strain from the wicking between the wire and solution bends the thinned section to the side at late stages in micropolishing.
7. Refresh the solution as necessary and cease etching once the thinned section is removed.
8. Clean and dry the tip using the same method as in step 3.

⁵Details on determining when the reaction is about to finish and what a tip should look like after this step can be found in the introduction to section 2.

2.2 Tips and Resulting Images

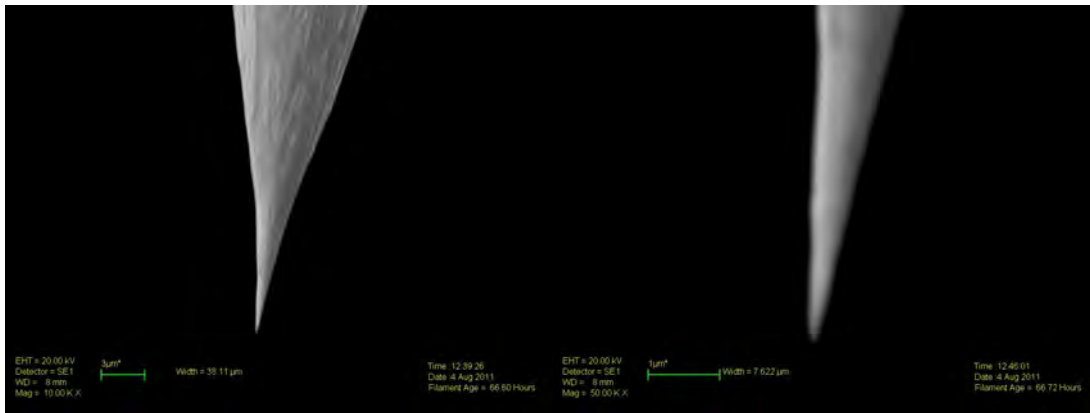
Tip Number/Operator/Sample	Optical Pictures (400x)	Open-Air STM Images
#1/Guido/DTC2		
#2/Guido/DTC2		
#3/Guido/DTC2		
#6/Guido/DTC2		

2.3 Discussion

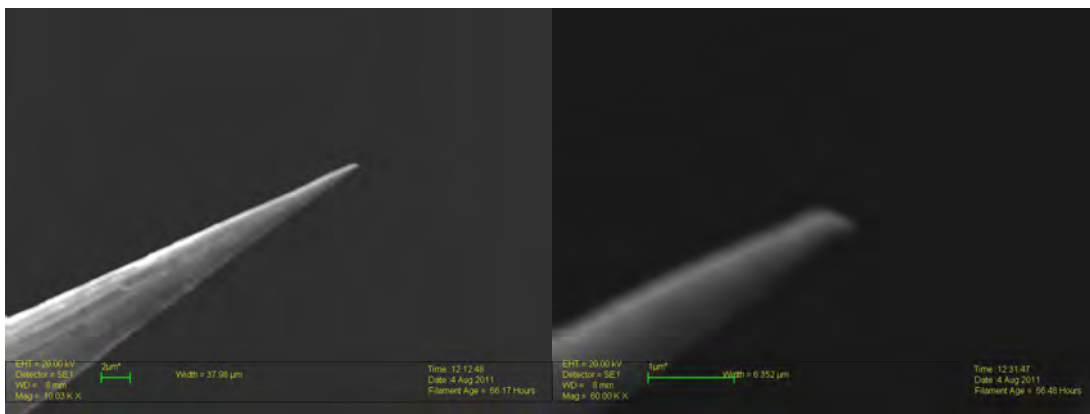
As exemplified in the optical pictures for tips #2 and #3, this method does produce significant bending at the tip apex. This makes it very difficult to align the tip properly with respect to the sample in order for tunneling to occur. Tips #1 and #3 produced fairly decent image resolution at 200nm scales, but it was difficult to get any more detail and all three images show significant smearing and noise. This method is still incomplete and not reliable in its current form. However, it does show promise as part of a different procedure as a way to control more of the etching in the micropolishing step instead of the difficult coarse etching step. Tips #1 and #2 had the thinned sections broken off and then etched a few times to sharpen. #3 had the thinned section broken off and then etching immediately ceased. #6 had the thinned section fold completely over during micropolishing and produced the worst image.

3 Electron Microscope Images

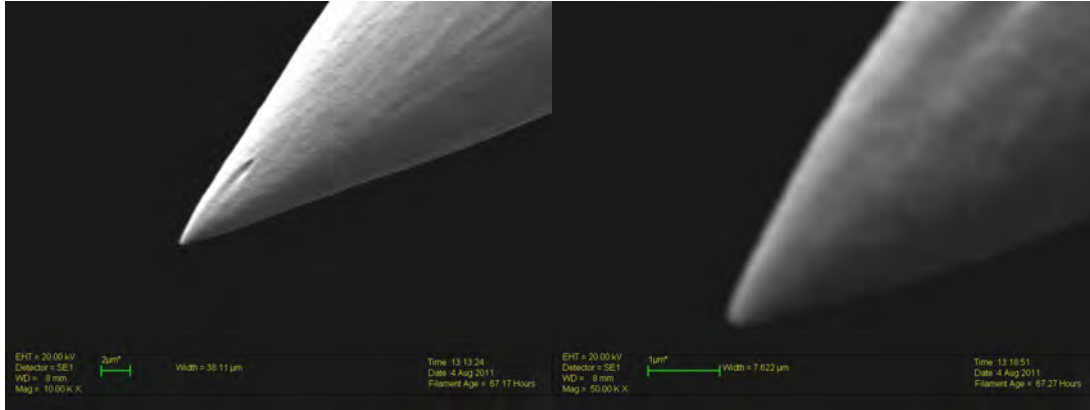
Our group took three tip samples mounted on carbon tape to the Notre Dame Integrated Imaging Facility and used a Leo SEM (scanning electron microscope) under Dr. Alexander Mukasyan in order to produce a series of images at x10,000 and x50,000 of three tip-making methods; the Argonne method, the experimental method, and the Geneva method used primarily by our group up to this point.



Figures 4a and 4b: Argonne method tip at (L) x10,000 and (R) x50,000



Figures 5a and 5b: Experimental method tip at (L) x10,000 and (R) x60,000



Figures 6a and 6b: Geneva method tip at (L) x10,000 and (R) x50,000

As one can see, though the electron microscope we used was not able to resolve much below $1\mu m$, the Argonne method produces much sharper tips (less than $100nm$) than the currently used Geneva method (about $300nm$). The experimental method also produced sharper tips than the Geneva method, however the bend at the apex is obvious and must be refined before useable tips are produced. A more detailed measurement of the tips' radii of curvature could be made in a higher resolution electron microscope, if additional accuracy or more information about the last few nanometers of the tip are desired.

4 Conclusions and Suggestions

The recommendation for the method at this time is the Argonne procedure. It produced atomic-resolution images, was not difficult to implement, and showed resilience to errors in the etching stages. The experimental method explored different ways to avoid run away etching at the end of the coarse etching step, but suffered from the problem of producing a delicate tip that deformed in the last stages of fine etching and produced tips with bent ends. Various other tip production techniques were not explored, but would be interesting to study in the future. These include tip annealing with a Bunsen burner in order to smooth out the tip apices and eliminate multi-tips, using various other solutions (including hydrochloric acid, sulfuric acid, and acetone), and building a cut-off circuit to further minimize cut-off time.

References

- [1] J. Lindahl, T. Takanen, and L. Montelius, *J. Vac. Sci. Technol. B* 16 (6), Nov/Dec (1998).
- [2] Center for Nanoscale Materials, *STM Tip Fabrication and Characterization Procedure*, (Argonne National Labs, Argonne, IL 2010) pp. 1-15.

Examination of the validity of statistical models for the
 $^{12}\text{C} + ^{12}\text{C}$ fusion reaction at sub-barrier energies

Erin Dahlstrom

2011 NSF/REU Program

Physics Department, University of Notre Dame

Advisor: Xiao-Dong Tang

ABSTRACT

Previous experimental studies of $^{12}\text{C} + ^{12}\text{C}$ fusion at sub-barrier energies using gamma spectroscopy have been limited by the use of a single detector. Use of the Gammasphere at the Argonne National Laboratory, however, allows for an array of germanium detectors to pick up the characteristic gamma rays, greatly increasing the information received. These decay products do not give us the total cross section for the fusion reaction though; we rely on statistical models that relate them to how the excited states are originally populated and decay. Using a combination of gamma spectroscopy based on data from the Gammasphere and proton spectroscopy from a recent $^{12}\text{C} + ^{12}\text{C}$ fusion experiment at Notre Dame, we tested these statistical models. The initial population of excited states for ^{23}Na predicted by Empire, a standard statistical model for the decay of different ^{24}Mg spins, was compared with the population determined from the gamma and proton spectroscopy. This comparison will potentially help us more accurately predict the spin population of ^{24}Mg , further constraining the fusion reaction theory.

1 INTRODUCTION

Carbon burning is the third step in the evolution of a star, preceded by Hydrogen and Helium burning as the first two steps. Studying these primary processes can help us understand not only stellar evolution, but also the nucleosynthesis of heavier elements. After fusing, two ^{12}C s form ^{24}Mg , which quickly evaporates to one of three channels: an alpha particle and ^{20}Ne , a proton and ^{23}Na , or a neutron and ^{23}Mg . In this report, we concentrate on the second channel. These evaporation products are in an excited state and decay to their ground state, releasing gamma rays [1]. This paper will focus on gamma spectroscopy from a ^{12}C fusion experiment using the Gammasphere at Argonne National Laboratory [2] and proton spectroscopy from a recent experiment at Notre Dame. While previous experiments used only one germanium detector [3, 4], the Argonne experiment is unique in that it collects data from an array of 110 germanium detectors, allowing us to gather many more gamma rays. We can in fact collect almost the full gamma decay information from the ^{24}Mg decay from which the decay feeding intensities for various channels are then determined. Such work was not possible in previous experiments, in which much of the information was lost by the simple detection system. Since experiments at the low energies most relevant to astrophysics are not feasible, these accurate measurements at higher energies are especially important to test the statistical models crucial to the determination of the total cross section at low energies.

In this paper, the analysis of the gamma ray data includes determining the efficiency corrected initial population of the ^{23}Na prior to its decay and checking this with the initial populations

predicted by Becker's data [3] and the proton channel of the Notre Dame experiment. We then compared the Gammasphere's initial population to the prediction by Empire, allowing us to predict the spin population of ^{24}Mg and test the statistical model [5]. Analyzing and understanding the new information obtained from this experiment will provide us with a new possibility to predict the spin population, which is essential for the understanding of the reaction mechanism of the formation of the $^{12}\text{C} + ^{12}\text{C}$ resonances.

2 EXPERIMENTAL METHOD

2.1 ^{23}Na and ^{20}Ne Decay Scheme

Using the data analysis program ROOT, I made a gamma-gamma graph of the Gammasphere data with the Doppler shift correction applied displaying two gamma ray energies that were detected in coincidence, which indicates they came from the same decay. Theoretically, this would be a matrix of points, as we know all of the expected energies from the decay, and due to quantization we should get only those energies. The graph, however, appears as a grid of lines because of background and Compton scattering events. Points appear at the crossing of lines where we would expect to see points on a theoretical graph.

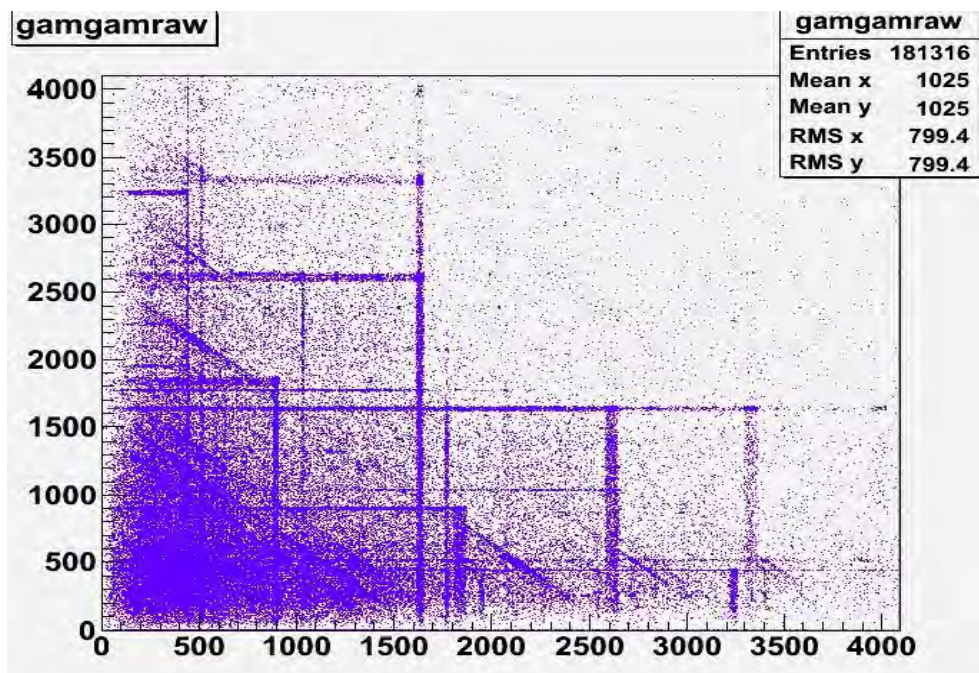


Figure 1: Gamma-gamma matrix measured at $E_{\text{CM}} = 5\text{MeV}$ using the Gammasphere.

By gating on a specific energy line and projecting the data onto one axis, we can find which gammas are emitted in coincidence with the first gamma energy by locating peaks. These peaks

can be identified using a level scheme, and we can determine the levels of ^{23}Na that were populated before the decay. We miss some of the decays because of their weak relative intensity, but this still provides an accurate picture. Gating on the 440 keV line, the strongest line in the spectrum, I found up to the 9th excited state populated for the ^{23}Na . There were two peaks not associated with ^{23}Na decay: one at around 900 keV which was identified as ^{88}Y contamination, probably left over from a previous Gammasphere experiment, and the standard 511 keV peak, which is the annihilation energy from pair production.

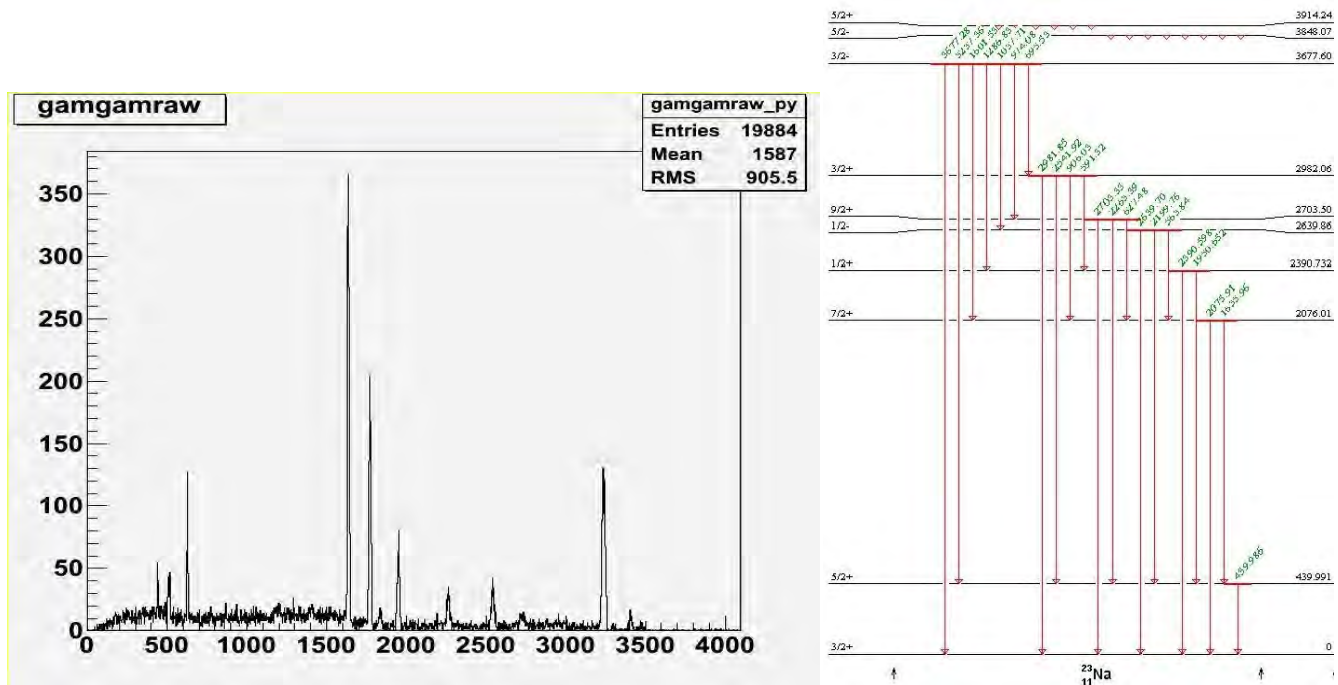


Figure 2: Left: Projection onto the y-axis of the gating at 440 keV. Right: ^{23}Na level scheme, ground to 9th excited

2.2 Efficiency Calibration

The germanium detectors pick up high energies with less efficiency, so before the data can be analyzed further, an efficiency curve must be calculated to correct this effect. To do this, we use gamma ray data from a source placed in the Gammasphere and allowed to decay. Since the source is known, its decay pattern is known including relative intensities of the gamma ray energies. We used ^{152}Eu and ^{56}Co as our calibration sources. With the measured intensity for each of the peaks, we can then use the equation,

$$I_d = I\varepsilon C, \quad (1)$$

where I_d is the measured intensity, I is the compiled intensity from NNDC [7], ϵ is the efficiency, and C is an unknown constant (necessary because the expected intensity is relative, not absolute), to find the relative efficiency, $C\epsilon$. The expected form of the gammasphere's efficiency curve is:

$$\epsilon_r = \exp[(A + Bx + Cx^2)^{(-G)} + (D + Ey + Fy^2)^{(-G)}]^{(-\frac{1}{G})} \quad (2)$$

with ϵ_r as the relative efficiency ($\epsilon_r = C\epsilon$), A through G as variable parameters that were adjusted to fit the efficiency curve, and x and y given by,

$$x = \ln\left(\frac{E_\gamma}{E_1}\right) \quad \text{and} \quad y = \ln\left(\frac{E_\gamma}{E_2}\right) \quad (3)$$

with $E_1 = 100$ keV, $E_2 = 1000$ keV, and E_γ also in keV [6]. The curve was first fitted separately to the two different sources, then an eighth parameter, H , was calculated to relate the two curves. The efficiency curves are displayed in Figure 3. Since these values are relative instead of absolute, to use the curve, we must pick a point as 100% efficient, determine the relative efficiency of the surrounding points, then apply this to the data.

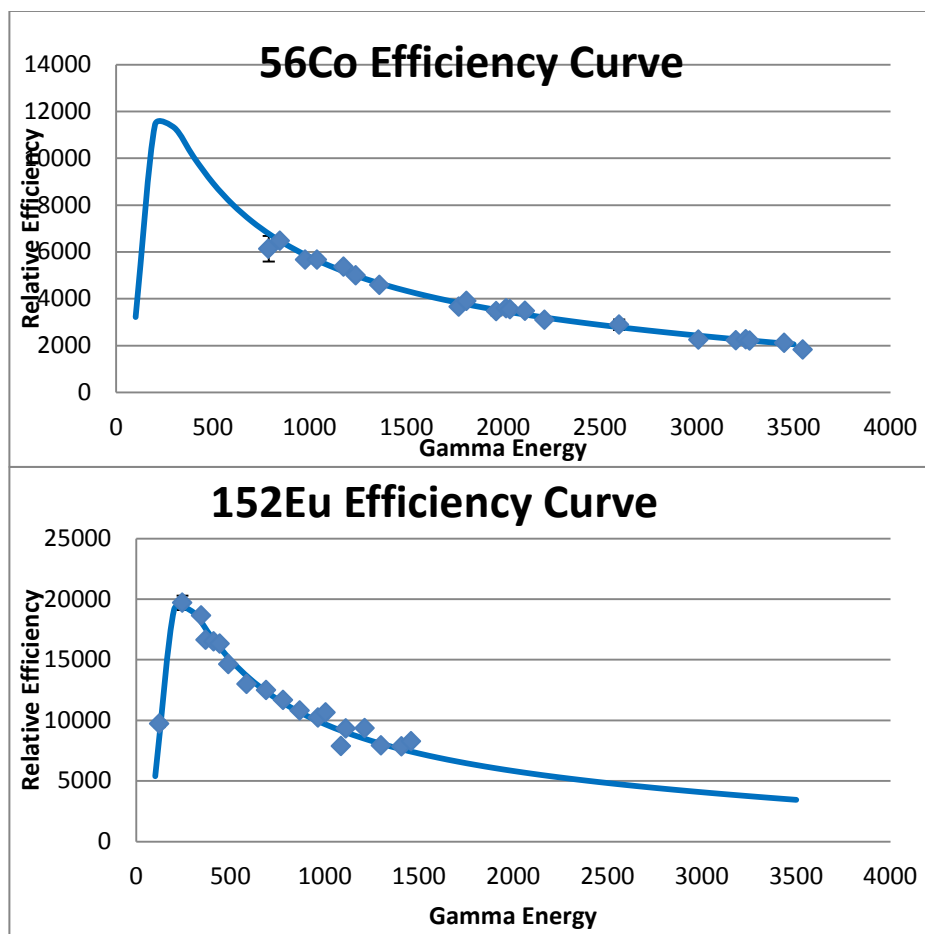


Figure 3: Efficiency curves for ^{56}Co and ^{152}Eu . Uses values: $A = 8.138$, $B = 3.776$, $C = -1.008$, $D = 8.695$, $E = -0.685$, $F = -0.0396$, $G = 11.342$, $H = 1.675$.

2.3 ^{23}Na Initial Population

2.3.1 Gammasphere Initial Population

To determine the initial population of ^{23}Na , we first assumed there were no levels populated above the 9th excited state, as the gamma ray energies that decay through 440 keV from above the 9th are too high for us to detect. According to Becker's data, decays from the 10th to 16th states would account for less than a tenth of the total decays, so this is a reasonable assumption, though a potential source of error. As discussed in section 2.1, by gating on the 440 keV line, we have all of the lower energy strong decays that pass through 1st to ground, but are lacking both the decays that go straight to ground and the smaller relative intensity decays. Since the relative intensities for all the decays are well known, however, we can correct for these unknowns.

Starting with the 9th excited state, we observed decays from $9^{\text{th}} \rightarrow 2^{\text{nd}}$ and $9^{\text{th}} \rightarrow 1^{\text{st}}$, and we expect to correct for $9^{\text{th}} \rightarrow \text{ground}$, $9^{\text{th}} \rightarrow 3^{\text{rd}}$, and $9^{\text{th}} \rightarrow 6^{\text{th}}$. We must also correct the $9^{\text{th}} \rightarrow 2^{\text{nd}}$ yield to account for those which decay directly to the ground state from 2^{nd} instead of to the 1st excited state. Once we know the total decay to the 2nd and 1st levels, we then use the known relative intensities to calculate all of the decays. This procedure is followed for all of the excited states: correct the experimental yields for any decays that go straight to ground then use the known relative intensities to calculate the decays that went undetected. For some of the lower levels, the cascading from above must be taken into account (e.g. $9^{\text{th}} \rightarrow 6^{\text{th}}$ when calculating 6^{th}); this is not part of the original population of that level.

We are limited in which levels we can calculate: anything that starts in the ground state will not give off gamma rays, so we are unable to determine the population of the ground state. The fourth state decays immediately to ground, and we gated on the energy from 1st to ground, so we lack the information to determine the initial population of the 4th and 1st excited states as well.

2.3.2 Comparison with Proton Channel and Becker

We next cross-checked the Gammasphere data with the proton channel from a recent Notre Dame experiment and the data from Becker's paper. Becker's data was displayed graphically; the graphs were printed out and the points found by hand. From the Notre Dame experiment, the energy versus angle of the emitted proton were recorded and are displayed in Figure 4, in which each horizontal line corresponds to the population of a particular state in the ^{23}Na . The 4th and 5th

channels are so close together that it is impossible to separate them accurately, as are the 8th and 9th channels. This graph is converted to q-value versus angle, then projected onto the y-axis, giving us peaks at the expected q-value for each channel, with the counts for each peak giving us relative populations.

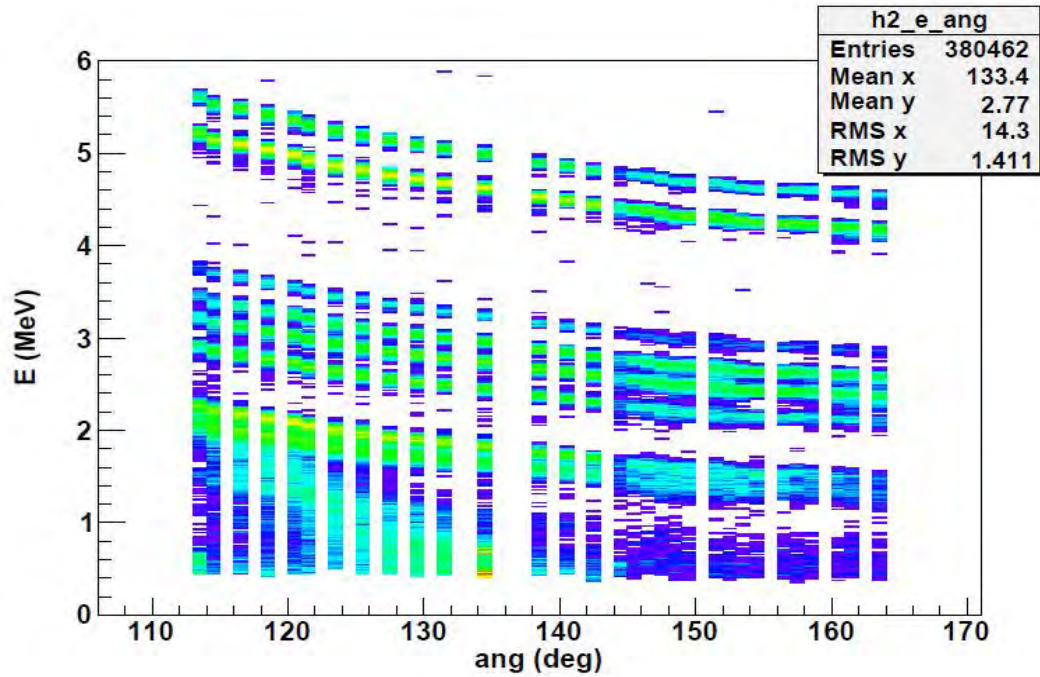


Figure 4: Energy vs. angle for various proton channels measured at $E_{CM} = 5\text{MeV}$.

To compare the data, ratios of the channels were made (e.g. 7th/6th), combining levels 9 and 8 since they are inseparable for the proton channel and ignoring the ground, 1st, and 4th excited states, as we do not have that information from the Gammasphere data.

Ratio	Gammasphere	Error	Proton (ND)	Proton (Becker)	Error
(9th+8th)/7th	1.210	0.059	1.028	0.659	0.038
(9th+8th)/6th	3.450	0.225	1.475	1.115	0.052
(9th+8th)/3rd	2.388	0.137	1.596	1.686	0.131
(9th+8th)/2nd	5.900	0.656	5.947	4.647	0.199
7th/6th	2.850	0.154	1.435	1.692	0.093
7th/3rd	1.973	0.088	1.553	2.558	0.213
7th/2nd	4.874	0.512	5.787	7.051	0.368
6th/3rd	0.692	0.043	1.082	1.512	0.115
6th/2nd	1.710	0.195	4.032	4.167	0.167
3rd/2nd	2.471	0.270	3.725	2.756	0.205

Table 1: Ratios of the individual excited state populations from the three sources.

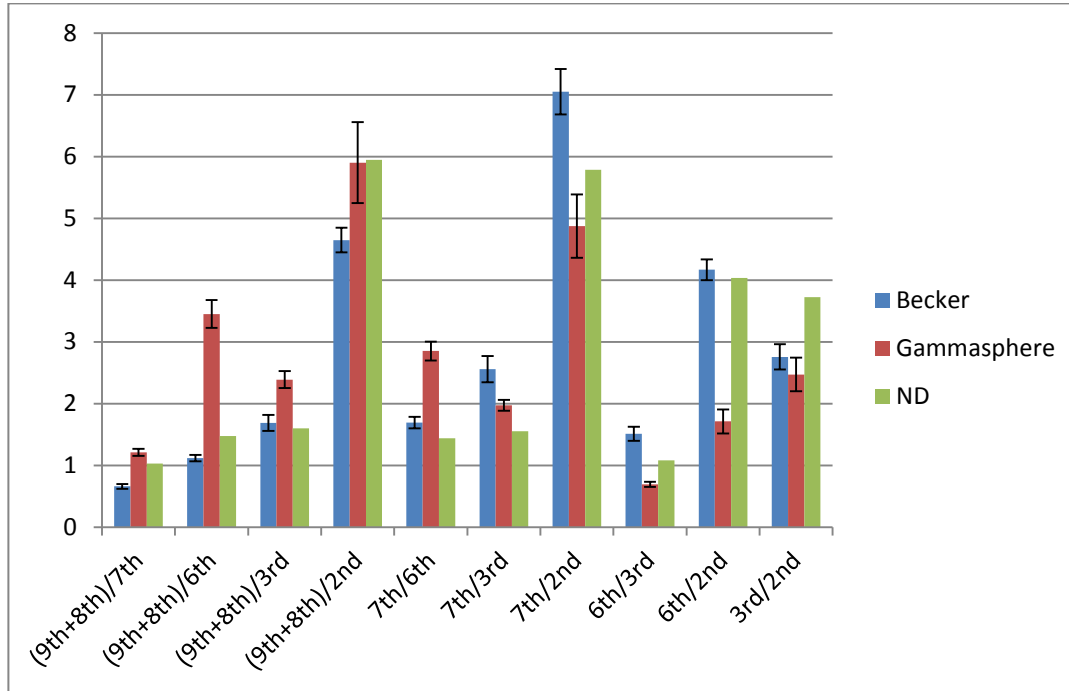


Figure 5: Graphic display of ratios of the individual excited state populations from the three sources.

2.4 ^{24}Mg Spin Population

Empire is a standard statistical model code developed by NNDC. It predicts the population of ^{23}Na using Hauser-Feshbach theory for a specific spin of ^{24}Mg : 0^+ , 2^+ , or 4^+ . We took that initial population and used it as input in another code, written by Professor Xiao-Dong Tang, which uses the known level scheme to simulate the gamma decay for a given ^{23}Na initial population and track the gamma rays emitted. It then displays these in the same format as the Gammasphere data, gating on the 440 keV line to produce a graph similar to Figure 2.

Taking these graphs, we get three different sets of peaks: one for each spin. We can set three undetermined constants, A, B, and C, to represent the percentage of each spin in the original spin population. To determine the values, I used Excel's Solver function to minimize the difference between the gamma yields from the Gammasphere and from the combination of ^{24}Mg spins as given by the statistical model. This gave a ^{24}Mg spin population with 7.33% spin 0^+ , 92.67% spin 2^+ , and 0% spin 4^+ .

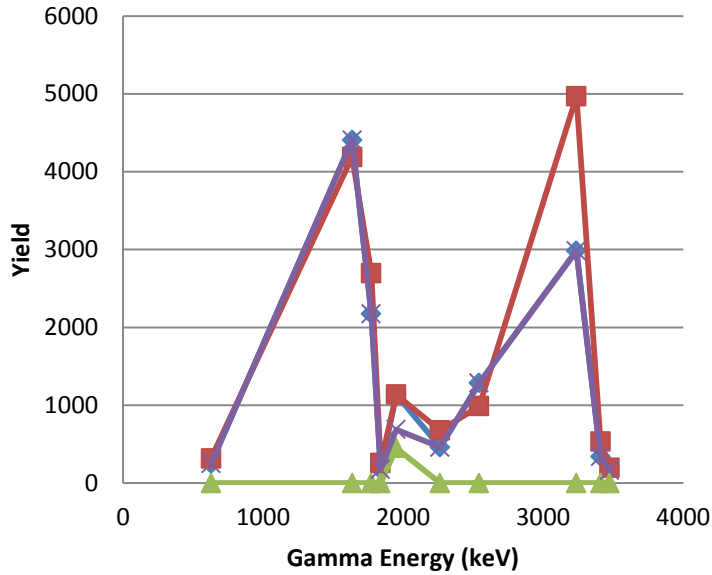


Figure 6: Yield versus Gamma ray energy (keV); Statistical model points include determined constants A, B, and C.

3 RESULTS AND DISCUSSION

The Gammasphere data does not match up entirely with the proton channel data from ND or the Becker data, however with an increase in the yield of the 6th and 7th excited states from the Gammasphere data, they would match within uncertainty. There could be states above the 9th excited level that cascade down to these which could be investigated by gating on other lines.

The statistical model and the Gammasphere data match with the 2⁺ spin assignment for the resonance at $E_{CM} = 5\text{MeV}$, however there is a large discrepancy for the 3237 keV line, corresponding to the transition from 7th \rightarrow 1st (see Figure 6). We can conclude that the statistical model is not perfect. With comparisons to data from the other channels of the Gammasphere experiment and the rest of the data from the Notre Dame experiment, we can hope to one day quantitatively understand how much the statistical model goes wrong and fix it for a better estimation of the fusion cross section at low energies.

4 ACKNOWLEDGMENTS

Support for this research comes from NSF Grants PHY-1068192 and PHY-0822648. A special thanks to Professor Xiao-Dong Tang, Brian Bucher, and Xiao Fang for their patience and many long hours of explanation, and to the Notre Dame Physics REU for a wonderful summer research experience.

5 REFERENCES

- [1] “Heavy ion reactions in Nuclear Astrophysics,” C.A. Barnes, S. Trentalange, and S.C. Wu, *Treatise on Heavy-ion Science*, edited by D.A. Bromley, Vol. 6, p.3 (Plenum, New York, 1985).
- [2] Gammasphere – Argonne National Laboratory:
<<http://www.phy.anl.gov/gammasphere/index.html>>
- [3] Becker, Hans-Werner. “Teilchenspektroskopische Untersuchungen Zur Absorption Unter Der Barbiere Bei Der $^{12}\text{C}+^{12}\text{C}$ Reaktion.” Ph.D. diss., Institut für Kernphysik Munster.
- [4] Kettner, K.U., “The $^{12}\text{C}+^{12}\text{C}$ Reaction at Subcoulomb Energies.” In *Zeitschrift für Physik A Hadrons and Nuclei*, 65-75. Springer Berlin / Heidelberg, 1980.
- [5] Empire code: <<http://www.nndc.bnl.gov/empire219/>>
- [6] Wang, Xiaofeng. “Exotic Collective Excitations at High Spin: Triaxial Rotation and Octupole Condensation.” Ph.D. diss., University of Notre Dame.
- [7] Evaluated Nuclear Structure Data File (ENSDF) – National Nuclear Data Center:
<<http://www.nndc.bnl.gov/ensdf/>>

Double Chooz and Neutrino Detection

Josh Ferguson

August 4, 2011

2011 NSF/REU Program

Physics Department, University of Notre Dame

Adviser: Dr. John LoSecco

Abstract

The Double Chooz experiment is designed to measure $\sin^2(2\theta_{13})$, which is a parameter of neutrino oscillations. The Chooz Nuclear Power Station produces anti-neutrinos as part of the decay of fission products with short half lives, and those anti-neutrinos react with protons in our detector, which in turn produce neutrons and positrons. Gadolinium captures these neutrons with a characteristic energy that we can use to eliminate much background. This is important because only about 1 in every 144,000 triggers recorded signifies the reaction of a neutrino. We can use the coincidence of neutron capture on Gadolinium and look back to find the energy of the annihilation of positron and electron to signify a neutrino. Given the known rate of neutrino production from the Chooz Nuclear Power Plant, the known squared mass difference of neutrino eigenstates, and the distance between the Power Station and our detector, theory gives us the rate at which we should receive neutrinos of the same flavor. In approximately three months of data taking we have found about 1,700 neutrino candidates.

1 Introduction

According to the standard model, neutrinos are mass-less leptons, traveling at the speed of light, each associated with a massive lepton and given a lepton family number, which is conserved. Unfortunately, in one of the biggest errors of the standard model so far, none of these statements are true. Neutrinos are seen to oscillate, or change flavor, which indicates that they have mass. Knowledge of this phenomenon began when it was noticed that only a third to a half of the neutrinos that were supposed to be coming from the sun due to H-He fusion (electron neutrinos) were observed. Some responses were to question the current solar model, but there was thought among the physics community that neutrinos might be able to oscillate. Further experiments were performed until from Super-Kamiokande, in Japan around 1998, we were given sufficiently convincing evidence that neutrinos oscillate. This experiment specifically tested the oscillation between muon and tau neutrinos, but later experiments confirmed neutrino oscillation for all flavors and also confirmed the ratios which neutrino oscillation would produce coming from the sun. Ever since the quest has been to discover the precise mixing angles of the neutrinos and

their mass differences. The Double Chooz Experiment is set up to determine $\sin^2(2\theta_{13})$ which is a mixing angle involving electron neutrinos.

2 Experiment

The Double Chooz experiment is located in the Champagne-Ardeaux region of France. The Chooz Nuclear Power Station is located on a peninsula-type intrusion of France into Belgium at the northeast corner of France. The detector is located a little more than a kilometer away from the nuclear reactors, which from the decay of products of the fission reaction produce electron anti-neutrinos. These anti-neutrinos react with protons in our detector, which produce neutrons and positrons.

The neutrons will capture on various atoms in the detector, but the two most common on which it captures are hydrogen and gadolinium. The detector is multiple layers of containers, only two of which contain photomultiplier tubes, the data-taking apparatuses of the experiment. Each layer contains a liquid made of organic molecules, some layers contain scintillator, some are simply oil, but each serve an important purpose.

The outermost layer is called the inner veto, whose job is to filter out cosmic muons. Muons are detrimental to the experiment because they have enough energy to simulate events which look like neutrinos. Neutrinos are detected by a coincidence event of a neutron capture on gadolinium, which has a binding energy around 8.2MeV, and a preceding event with slightly more ambiguous criteria, but it is essentially the gamma rays which come from the positron electron annihilation after the neutrino-proton interaction. While we know almost exactly the energy that the gamma rays from the annihilation should have, we don't know how much energy the neutrino had when it entered the detector, we can only know upper and lower bounds.

Muons can strike the outer rock surrounding the inner veto, which can produce showers of neutrons all capturing within a 500 μs window, simulating a coincidence event. The detector is buried far enough underground that the muon rate is not so high, approximately 10Hz, as to make data taking impossible, but it does present significant background. We have to exclude

events which trigger anything in the inner veto, which significantly decreases the number of possible events we can look at. For example, given the proper cuts (no inner veto signal in the early or late event being one of them) we see about 1700 neutrino candidates from about 1291 hours of running. If the same cuts are made, but force there to be something in the inner veto then you get about 5800 events, some of which might actually be neutrinos that we have to ignore.

The next layer is called the buffer. It is full of, quite simply, mineral oil. The job of this layer is to act as another layer of protection from any outside particles. There is no scintillating material, so it will not produce light when any particles move through, except for the very weak Cherenkov light. Another useful feature of the buffer layer is that the tank is made of steel so the photomultiplier tubes (PMTs) can be attached to it. The two inner-most layers, to be discussed later, have acrylic walls, so photons will pass through them easily and be caught on the PMTs. This makes the buffer layer, quite possibly, the most important layer, because it is able to mount the data-taking portion of the experiment.

The gamma catcher is the next layer. It is full of scintillating liquid which is designed to scintillate when any gamma rays from positron annihilation or gadolinium neutron capture escape the target. This is an important function, since we need to make sure to capture all of these possible, as so few indicate neutrino events.

Finally, contained inside the gamma catcher is the target. The main thing that separates this from any other portion of the detector is that it is loaded with gadolinium. As already explained, this is an extremely effective neutron capture atom. Gd-157, which makes up approximately 20% of the gadolinium has the highest thermal neutron capture cross section of any atom, 259,000 barns. To compare this with the other effective neutron capture atom in the experiment, hydrogen has a cross section of 0.3321 barns. Granted, there are many thousand times more hydrogen atoms than gadolinium-157 atoms, but the other benefit of gadolinium is that it has a very short capture time, about $30 \mu s$. Since the cross section is so high a neutron is not likely to travel very far before it gets captured. It is so short that we can make a cut three time constants out before we get close to the capture times of hydrogen. This makes it very effective for isolating only the

target region and only those neutrons which captured on gadolinium.

The experiment is then buried approximately 300 meters underground to protect it from background. As is obvious, the major challenge of the experiment is to reduce the background as much as possible, first done in the design of the experiment, and then in the post processing of the data.

3 Data Analysis

The brunt of my work this summer has been in data analysis. I came into the program only having a cursory knowledge of a couple programming languages and reasonably little knowledge of general terminal usage and scripting. As a result I had to spend much of my time learning ROOT, which is the data analysis program used by many high energy physicists, including those at CERN and Fermilab. I learned quite a few tricks about shell scripting and terminal usage, and improved my proficiency in C++. Unfortunately, I did not come into this REU with any particle physics classes under my belt. I regret that I wasn't able to learn more physics, but the computer science I learned will be invaluable to my future career as a physicist.

Some of the analysis that I was able to do this summer started out as work trying to analyze the dead time of our detector. It is known that our detector has some limitations as to the amount of data that it can take. One principle of our detector is that it only releases data every 32ns, so in that period the PMTs will collect all the energy they can from any photons that make it in and integrate it to output the total light for that time period in the form of a charge, which relates to energy. (Unfortunately, the detector is not calibrated, so we have to make our best guess as to how charge relates to energy.) 32ns is essentially only enough time for light to travel through the detector and reach a PMT from an event, so there is a high correlation between a single event happening and recording only the data from that event. Nevertheless, it is possible that multiple events could happen, by coincidence, within nanoseconds of each other and be combined in the same trigger. That means that we might throw out a useful event because it has the added energy of another event with it, but this would be impossible to distinguish, so

it is included as a small percent into the uncertainty of the experiment. One more noticeable bit of true dead time is following a trigger there is always at least a 146ns period where no data is taken. Fortunately, the data down there is almost entirely junk (meaning there is no physics that it could signify, it is just noise in the detector), but it still means there's a period of time where an important event could happen as we miss it. It means that at the very least there is this amount of dead time multiplied by the number of events that occur, which amounts to only about 0.002% of our run time. If this is the only dead time, then there is little reason to worry about it because that percentage is extremely small and well within the range of general uncertainty. There are some that believe that all the data taken up to 500 μs after a high energy muon passes through the detector must be completely ignored, and that amount of dead time would contribute significantly to the measurement of the neutrino rate. I don't see why that should necessarily be called dead time if we make our cuts correctly. In fact, with the cuts that are most likely to find neutrinos, including that constraint only reduces the number of neutrinos by 0.1%. In the time I've been here there has been no solid consensus on what criteria count as dead time, so it is a topic that I have not been able to work on much, as it is very complex and there are many points to the system that I am simply not educated in.

Another important thing I found, which was brought to the research group's attention, was that the trigger rate has increased by nearly 5% in 3 months of running. This has been explained as a slight temperature increase in the area of the detector, so the noise in the system has increased. My professor doesn't believe that this is a completely adequate answer, because the rate continues to rise all the time. I guess the only way that we'll know is as we approach winter the rate goes back down. This is my only original contribution to the experiment that I know of.

Another thing I worked on was rates based on certain cuts. A group at MIT developed a list of cuts on the data that they believed would be beneficial to the data analysis and my job was to double check their results. In the end things matched, but I haven't heard any news of further things that are planned to be done with those cuts.

The last thing that I have been working on is developing a program that will sort through the data and TTrees (a data class of ROOT) full of possible neutrinos from all the runs taken

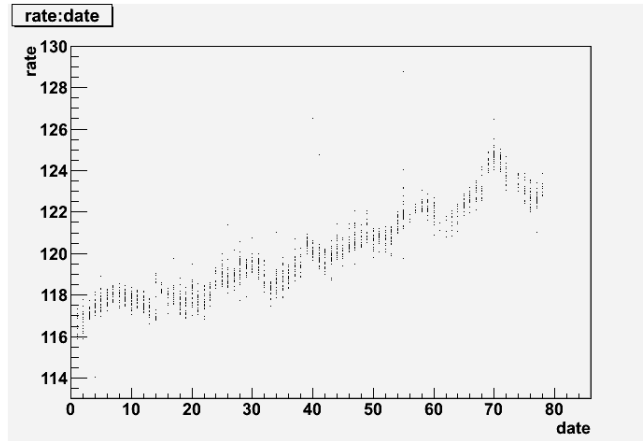


Figure 1: Raw trigger rates over time. The y-axis is triggers per second, and the x-axis is days from first run on April 13.

so far. It is designed to look for the coincidence events that I have discussed in detail so it cuts a good amount of the data. It reads in 1428 files and creates a single file that is very close to the same size as any one of those 1428 files. I was eventually able to create a graph showing probable neutrinos.

4 Conclusions

With the rough estimate of the number of neutrinos that we have we can make some premature conclusions about the current theory of the value of $\sin^2(2\theta_{13})$. The way that we attempt to reach these conclusions is through comparison with a simulation which simulates a year's worth of neutrino interactions in the detector. I first look at the amount of neutrinos from the simulation that are within my cuts, then I compare the ratio of the time of the live run and time of the simulation run with the ratio of the number of neutrinos from the real run to the number of neutrinos from the simulation.

$$\frac{\text{neutrinos from simulation}}{\text{neutrinos from real runs}} = \frac{\text{time of simulation}}{\text{time of real runs}} \quad (1)$$

If this is satisfied then the mixing angle matches that which is used in the simulation. Another way to compare the real data with the simulation is by looking at the shape of the neutrino

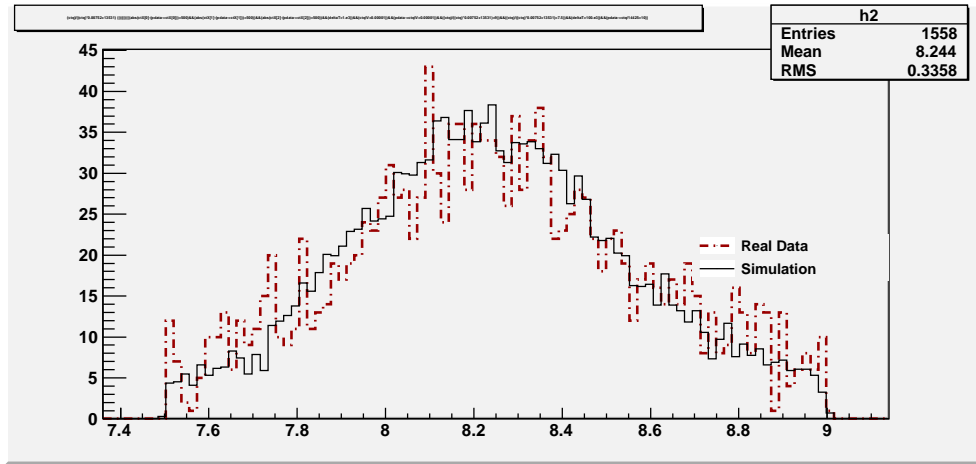


Figure 2: A comparison of the gadolinium capture peaks.

spectrum. The neutrino mixing angle will have an effect on the energy distribution that we are able to see, so by comparing the shapes we are able to get a value for the mixing angle. The following images are comparing real data to simulation data with identical cuts. The red dotted lines will be the real data with the black being simulation data. In figure 2 we start with comparing the Gadolinium capture peaks. The benefits of these peaks are discussed elsewhere as far as background is concerned, but for the sake of data analysis, these are the starting point for making sure the two sets of data are comparable. This is the set of data on which I matched up the peaks and scaled the simulation data to match the real data so that the area under each curve is the same. The reason we have to do so much comparison to begin with is because neither the simulation or the real data is calibrated. On the x-axis of Figure 2 and Figure 4 the measure is, to a close approximation, MeV, but this is done by dividing the total charge that comes out of our PMTs by a function. This function can be called the gain, and the gain for the simulation and the real data is different; it is not even constant. The gain appears to vary with the charge according to $gain = 0.00752 * ctq + 13531$, as a first order approximation. ctq is the name of the variable within the program, the “ct” stands for the name of the data processing program and the “q” stands for charge. I attempted to come as close as possible to obtaining a result where the two peaks matched up, but as can be seen, the shape of the gadolinium peaks is still different between the real and simulation data. One possible reason for this is that there is background in our data and no background in the simulation. That would mean that my scaling factor is

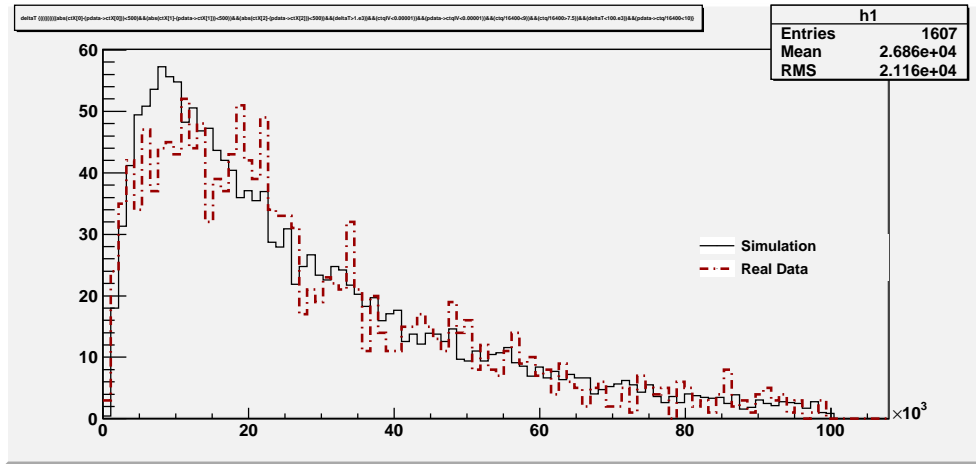


Figure 3: A comparison of the time between an annihilation event and a neutron capture event.

off, because by attempting to match the area under the curve I am assuming that my real data is all neutrinos, when they can only be called neutrino candidates. The simulation, on the other hand, is limited to only showing pure neutrino interactions.

Figure 3 is the spectrum of neutron capture times on gadolinium. It should be an exponential function with a time constant of $30 \mu s$, and if you make some comparisons, e.g. 37% of max at one time constant, 13.5% of max at two time constants, etc, it closely resembles an exponential. But more examination will show that it doesn't approach zero very well. Looking at the real data it can be seen that the shape does not match perfectly. At low times there is less, but the area under the two is still the same, because this plot is based on the same cuts as Figure 2. This likely reflects on the ability of our detector and the strength of our cuts.

The graph that most closely has a relation to the mixing angle is Figure 4. This graph shows the energies of the positron annihilation, which are directly related to the energies of the neutrinos as the reacted in the detector. All you need to do is subtract the energy from the positron, 0.511 MeV, to get the energy of the neutrino. The energy spectrum of the neutrinos is related to the mixing angle and squared mass difference, so from this last graph we can extract the mixing angle. The equation for the probability for an electron neutrino to be found at a different position as an electron neutrino again is:

$$P_{ee}(E_{\bar{\nu}_e}, L, \Delta m_{31}^2, \theta_{13}) = 1 - \sin^2(2\theta_{13}) \sin^2 \left(1.27 \frac{\Delta m_{31}^2 [10^{-3} eV^2] L [km]}{E_{\bar{\nu}_e} [MeV]} \right).$$

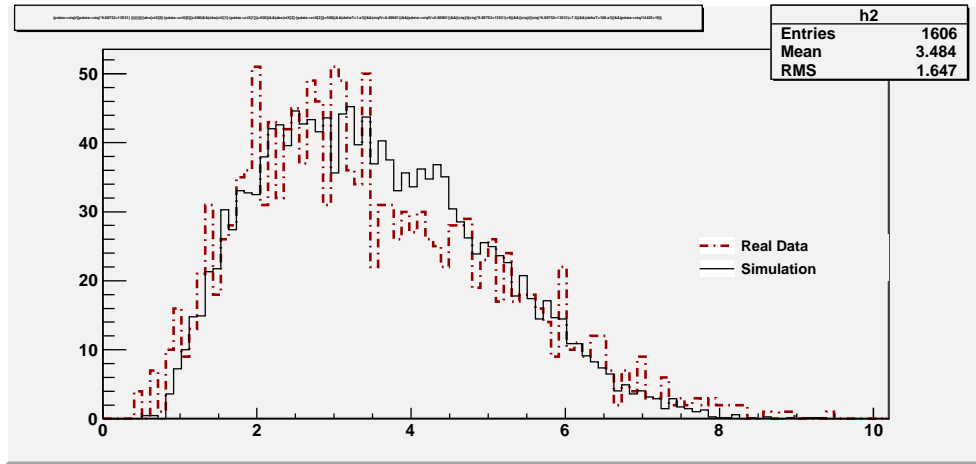


Figure 4: Comparison of neutrino peaks.

Δm_{31}^2 is the squared mass difference of the third and first mass eigenstate of the neutrino, L is the length between observations, and $E_{\bar{\nu}_e}$ is the energy of the anti-neutrinos. Unfortunately, I did not have the time to learn and put into practice the statistical tools which would allow me to make the comparisons between the graphs. Also, for the sake of a non-biased result, the scientists making these cuts shouldn't know the mixing angle put into the simulation. Another important piece of data to include is that the inverse from equation 1 is 0.163 for the ratio of times and 0.145 for the ratio of suspected neutrinos.

Other problems with the simulation vs. the real data is that every now and then one of the reactors have to be put offline for a while, so we get half the neutrinos we should. The simulation, on the other hand, assumes full power all the time. In addition, the simulation data that I have access to most likely does not take into account fuel evolution from mostly uranium to mostly plutonium. With all these errors to take into account I don't believe that there can be a statistically significant comparison between the data and the simulation. Nevertheless, the experiment will continue to run for years to come, and with more data comes more statistical significance. The experiment will continue to be refined and hopefully we can shed more light on $\sin^2(2\theta_{13})$.

Measuring the Half-Life of ^{60}Fe Data Analysis

Quinn Hailes
2011 NSF/REU PROJECT
Physics Department
University of Notre Dame
Advisor: Dr. Philippe Collon
Mentors: Will Bauder, Matthew Bowers, Karen Chamberlin,
Wenting Lu

August 5, 2011

Abstract

^{60}Fe is a galactic gamma-radioactive isotope that is a signature of stellar nucleosynthesis. It can be found in deep-sea crust and could be a signature of possible recent nearby supernovae activity. If the half-life of ^{60}Fe is accurately measured we can assess how far from the earth a supernova occurred and precisely date how long ago it transpired. The half-life of radioactive isotope ^{60}Fe has an accepted value of 2.62×10^6 yr. This new value measured at the Technical University of Munich is in contradiction to the previously accepted value of 1.49×10^6 yr. Our new experiment is to re-measure the half-life of ^{60}Fe through Accelerated Mass Spectroscopy (AMS) and a low level counting station to eliminate some of the background radiation and other error in the accepted value. In this paper I will discuss the data analysis for the activity of ^{60}Fe .

Introduction

A major key for understanding the development of our universe is looking at radioactive nuclei that are produced by astrophysical processes. Specifically ^{60}Fe is produced naturally in supernovas only. The half-life of ^{60}Fe plays a major role in multiple stellar investigations. The half-life is defined as the time for the radioactivity of a certain isotope to fall to half its original value. The new measurement for the half-life of ^{60}Fe is 2.62×10^6 yr has a significant amount of error in it. To measure a precise value for the half-life of ^{60}Fe , two different approaches are used, a low background activity measurement and accelerated mass spectrometry (AMS). A direct measurement of the half-life of ^{60}Fe cannot be done due to how long it is. So the goal is to look at the decay scheme of ^{60}Co to ^{60}Ni as shown in figure 1, because of the gamma rays emitted after the beta minus decay. It is much easier to measure the activity from ^{60}Co to ^{60}Ni because the gamma ray ejection can be measured by our detector. The β -minus decay of ^{60}Fe to ^{60}Co cannot be measured. A low level counting station can be used to measure the activity of the gamma-ray ejection.

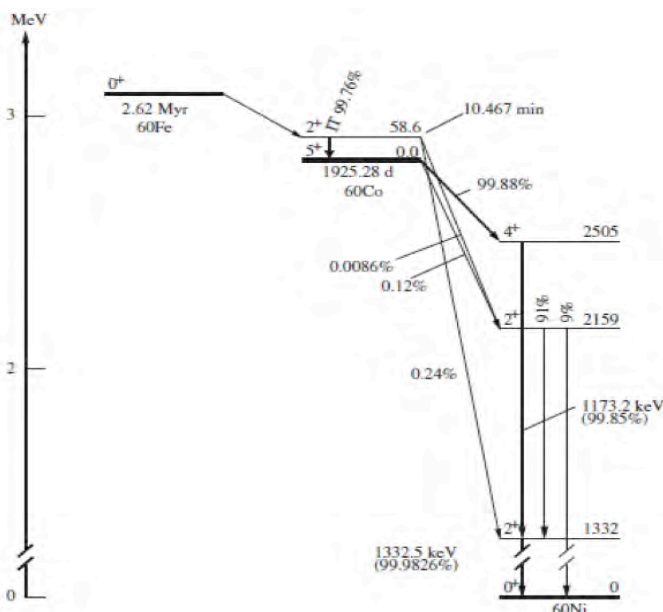


Figure 1 – Decay Scheme of ^{60}Fe

The activity of ^{60}Co is measured when a vial is placed into the low-level counting station. The activity of ^{60}Co is looked at rather than ^{60}Fe is because the decay of ^{60}Fe is such a long process and it would take too long to measure. Since ^{60}Co is the daughter nucleus of ^{60}Fe and has a known half-life of 5.27 years, it can be used to determine the activity of ^{60}Fe using equation 1.

$$A(t) = A(1 - e^{-\lambda(t)}) \quad 1$$

In this equation, $A(t)$ is the activity of ^{60}Co , t is time, λ is the decay constant of ^{60}Co , and A is the amount of ^{60}Fe activity, which is our unknown. The decay constant of Cobalt, λ_{Co} , is found through the use of equation 2, where $t_{1/2}$ is the half-life of ^{60}Co .

$$\lambda = \frac{\ln(2)}{t_{1/2}} \quad 2$$

The above equation 2 was derived from equation 1. From the activity and decay constant of ^{60}Co , the activity of ^{60}Fe can be calculated using equation 1. To determine the decay constant of ^{60}Fe the radioactive decay law (equation 3) is used to derive a formula for activity, equation 4.

$$\lambda = -\frac{(dN/dt)}{N} \quad 3$$

$$A = \lambda \cdot N \quad 4$$

In the radioactive decay law, N is the number of radioactive nuclei present at time, t and λ is the decay constant. In equation 4 which is used to find the decay constant λ of ^{60}Fe , A is the activity of ^{60}Fe and N is the amount of ^{60}Fe nuclei present. The amount of ^{60}Fe present is found through a process called AMS, which is a technique similar to mass spectroscopy where a particle accelerator is used to disassociate

molecules, ionize atoms, and accelerate the ions to be analyzed in a detector. With these two values from the AMS technique and the low level counting, the decay constant of ^{60}Fe can be calculated from equation 2. However instead of measuring ^{60}Co , ^{60}Fe values will be placed in the formula.

Our low level counting station consists of detector and lead castle. A Germanium γ -ray detector is a solid-state detector, which uses a crystalline scintillating material rather than an ionization chamber to detect and measure radiation. Germanium detectors must be cooled to liquid nitrogen temperatures to produce spectroscopic data. At high-temperatures, the electrons can easily cross the band gap in the crystal and reach the conduction band where they are free to respond to the electric field. The system will then produce too much electrical noise to be useful as a spectrometer. Cooling to liquid nitrogen temperatures reduces the excitation of valence electrons so that only a gamma ray interaction can give an electron the energy needed to cross the band gap and reach the conduction band. Since the detector cannot eliminate external or background radiation found in the surroundings a lead housing is built around the detector for improved results.

Data & Results

The lead castle was created in the summer of 2010. From then to the summer of 2011 there have been multiple runs. I have analyzed both runs 5 and 6. Each run takes about 14 days. There are two background runs each taking 24 hours each, then four ^{60}Co standards each taking 30 minutes, and then there is a 12 day run on a ^{60}Fe sample. The ^{60}Co standards are used for calibration and efficiency. A High-Purity Germanium detector (HPGe) measures the amount of activity in the ^{60}Co sample. The detector runs on software that can analyze the data and the background radiation in the running room. My data analysis focused on run 5, which occurred April 21, 2011, and run 6 which occurred May 28, 2011. The difference between run 5 and run 6 is that a different detector was used. In run 5 the efficiency of the detector was 1% and in run 6 the detector had an efficiency of 3%. In each run I was looking at the 6 different peaks. Peak 1 was ^{59}Fe with energy of 1099 keV, peak 2 was ^{60}Co with energy of 1173 keV, peak 3 was ^{59}Fe at a different energy level of about 1289 keV, peak 4 was ^{60}Co at a different energy level 1332 keV, peak 5 was ^{40}K with energy of 1465 keV, and peak 6 was ^{208}Ti with energy of 2615 keV. My main concern was the net count of the ^{59}Fe and ^{60}Co because this was the activity that needed to be measured. The elements ^{40}K and ^{208}Ti are in the data analysis from background radiation; they are present because of the bricks and concrete from the building. To make this background radiation as miniscule as possible a lead brick house was built around the detector. Lead bricks are used to block radiation because they are high in both density and atomic mass.

Run 6 results:

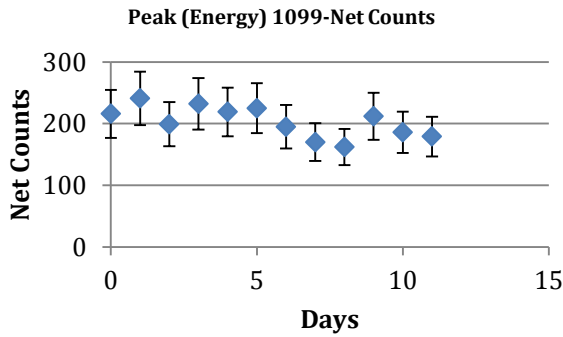


Figure 2 - ⁵⁹Fe at 1099 keV (Run 6)

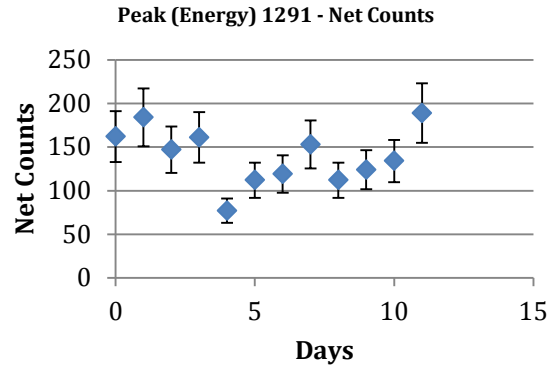


Figure 3 - ⁵⁹Fe at 1291 keV (Run 6)

The graphs above represent the number of counts per day, for run 6, of both energy levels of ⁵⁹Fe. Figure 2 is ⁵⁹Fe with energy of 1099 keV over a period of 12 days.

Figure 3 is ⁵⁹Fe with energy of 1291 over a period of 12 days.

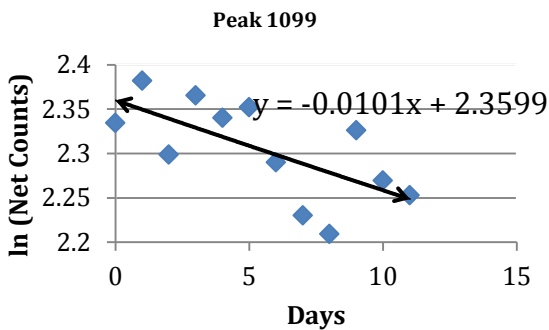


Figure 4 - Run 6 Fit Line (1099)

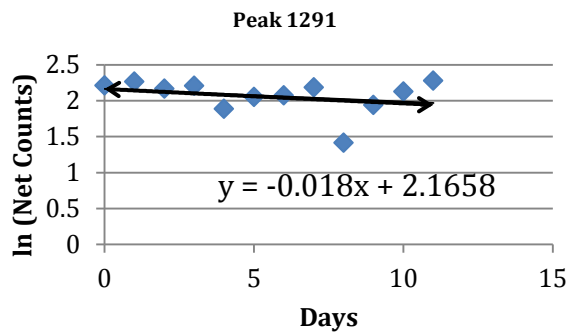


Figure 5 - Run 6 Fit line (1291)

Figure 4 as shown above shows a linear fit for the peak 1099 of ⁵⁹Fe for Run 6. The values on the y-axis for this graph are the natural log of the net counts. A linear line is easier to fit than an exponential curve. In other words the decay is a value, which will always be the same no matter how much material is present. Figure 5 is an linear fit for the peak 1291 of ⁵⁹Fe for Run 6.

Run 5 results:

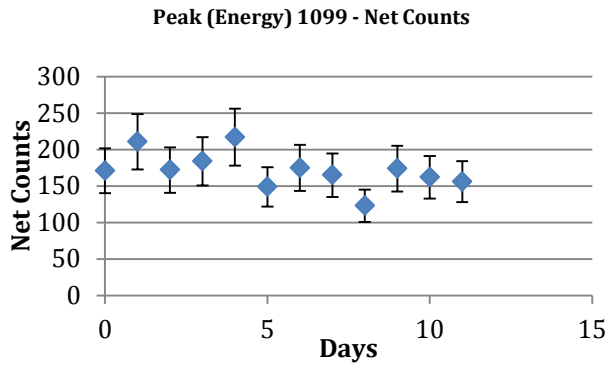


Figure 6 - ⁵⁹Fe at 1099 keV (Run 5)

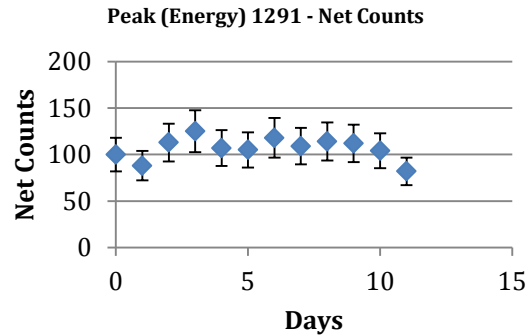


Figure 7 - ⁵⁹Fe at 1291 keV (Run 5)

The graphs above represent the number of counts per day, for run 5, of both energy levels of ⁵⁹Fe. Figure 6 is ⁵⁹Fe with energy of 1099 keV over a period of 12 days.

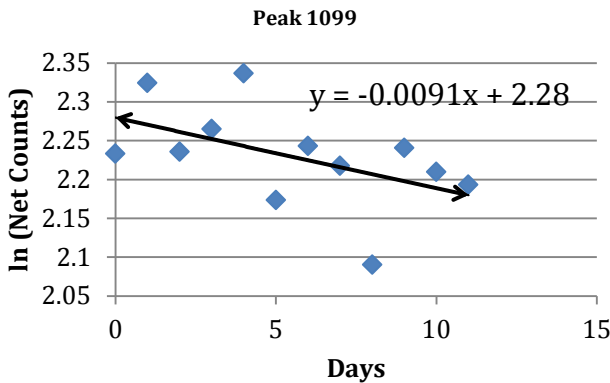


Figure 8 - Run 5 Fit Line (1099)

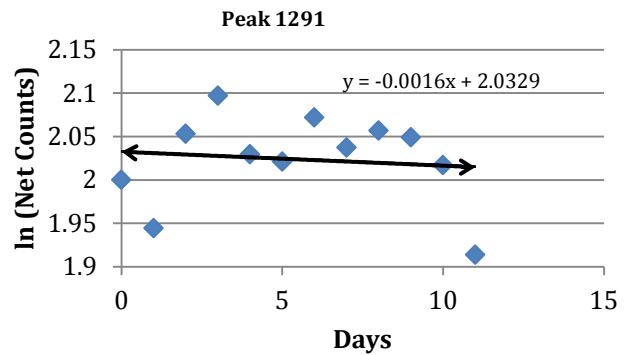


Figure 7 is ⁵⁹Fe with energy

Figure 9 - Run 5 Fit Line (1099)

of 1291 keV over a period of 12 days.

Both Figure 8 and 9 display the linear fit line for the different energies 1099 keV and 1291 keV. The theoretical value will always be higher than the value actually obtained from the experiment because the geometry of the detector. To take this

into account for a precise measurement of the activity I looked at the efficiency. For the detector the efficiency was calculated to be about 3%.

Conclusion

For this experiment a ^{60}Fe sample was placed inside the lead castle to obtain a measurement for ^{60}Co . The decay peaks at the energies 1099 keV and 1291 keV of ^{59}Fe was analyzed. The data displayed in figures 2-9 was measured and calculated for the activity of ^{60}Co . This activity will be plugged into equation 4. The number of ^{60}Fe nuclei, N , is currently being worked on too by graduate students in the process of AMS. When both λ and N is calculated and implemented into equation 4 the decay constant of ^{60}Fe will be measured. From this we can find the half-life of ^{60}Fe . The gamma energies for ^{60}Co have not come up yet because the ^{59}Fe hasn't decayed completely. Run 7 data was just analyzed and shows that ^{59}Fe is now background radiation. Since the ^{59}Fe has went to background the gamma energies of ^{60}Co will be analyzed as it starts to appear.

References

- [1] Rugel, G. et al., "New Measurement of the ^{60}Fe Half-Life." *Physical Review Letters*. (2009): 1-4.
- [2] Knoll, Glenn. *Radiation Detection and Measurement*. 2rd ed. New York, NY: John Wiley & Sons, Inc., 1989, 65-96, 387-397
- [3] Kutschera, Walter et al., "Half-Life of ^{60}Fe ." *Elsevier Science Publishers B.V.*. (1984): 430-435.
- [4] Krane, Kenneth. *Introductory Nuclear Physics*. John Wiley & Sons, Inc., 1988

Analyzing Potential Tracking Algorithms for the Upgrade to the Silicon Tracker of the Compact Muon Solenoid

Authors:

John HARDIN

Kevin MCDERMOTT

Advisors:

Professor Michael HILDRETH

Professor Kevin LANNON

2011 NSF/REU Program
Physics Department, University of Notre Dame
August 5, 2011

Abstract

The research performed revolves around creating tracking algorithms for the proposed ten-year upgrade to the silicon tracker for the Compact Muon Solenoid (CMS), one of two main detectors for the Large Hadron Collider (LHC) at CERN in Geneva, Switzerland. The proposed upgrade to the silicon tracker for CMS will use high-speed electronics to trace particle trajectories so that they can be used immediately in a trigger system. The additional information will be combined with other sub-detectors in CMS to distinguish interesting events from background, enabling the good events to be read-out by the detector. The algorithms would be implemented directly into the Level-1 trigger, i.e. the first trigger in a two-trigger system, to be used in real time. Specifically, by analyzing computer generated stable particles over various ranges of transverse momentum and the various tracks they produce, we created and tested various simulated trigger algorithms that would be hopefully used in hardware. As one algorithm has proved very effective, the next step is to test this algorithm against simulated events with an environment equivalent to LHC luminosities.

1 Introduction: The LHC Machine

In Geneva, Switzerland, home to the European Council for Nuclear Research (CERN), is the world's most powerful man-made particle accelerator. Located an average 100 meters below the surface, the Large Hadron Collider (LHC) accelerates protons and heavy ions in a 27-kilometer ring for collision. The LHC looks to answer some of the most fundamental questions concerning the nature of the universe. The Standard Model of Particle Physics is currently acknowledged as the most complete description of particle interactions between the electromagnetic, weak, and strong forces. However, under certain symmetries, the electromagnetic and weak forces can be unified under one electroweak force, but only if the particles mediating the weak force have no mass. Yet, the W and Z bosons are observed to have mass, and so something must be added to the theory. One explanation is the Higgs boson, which continues to remain elusive. Finding the Higgs boson is one of the main reasons behind the construction of the LHC and its detectors. In addition to solving the electroweak symmetry breaking, the LHC looks to answer questions concerning the nature of dark matter, dark energy, supersymmetry, and extra dimensions. All these questions seek to test physics beyond the Standard Model.

At design specifications, the LHC reaches a maximum of 14 TeV center of mass energy for proton-proton collisions. Each proton beam has an average energy of 7 TeV, which corresponds to approximately 7500 times the rest mass energy of a proton. Due to initial setbacks, the LHC is currently operating at only half of this energy. The current peak luminosity, or the number of particles per unit area per unit time, of the proton beam collisions is on the order of $1.25 * 10^{33} cm^{-2}/s$ [2]. Design specifications have bunch crossings occur every 25 ns, or 40 MHz, resulting in 2808 bunches in the entire LHC [1].

2 The CMS Detector

The Compact Muon Solenoid is the detector for one of two major particle physics experiments being performed at the LHC, the other being ATLAS. CMS gets its name from being small relative to ATLAS, from the solenoid inside of it which produces a 3.8T magnetic field, and from the muon detectors which sit outside the solenoid and make up a large percentage of the overall volume. CMS is designed for both flexibility in studying various results of particle collisions and especially for efficiency and accuracy in detecting muons. CMS has 4 layers, each consisting of a barrel and an endcap. See Figure 2 below for schematic layout. The layers are the silicon tracking layer, the electromagnetic calorimeter, the hadron calorimeter, and the muon detector when they are listed from innermost to outermost. The

solenoid is directly between the hadron calorimetry layer and the muon system. The barrel of each layer is optimized to detect events which are close to perpendicular from the beam line (low η , or pseudorapidity), while the endcap tends to be oriented perpendicular to the barrel and is optimized for higher η events. η is a measure of how close a particle is to being parallel with the beam. $\eta=0$ corresponds with a perpendicular, while $\eta=\infty$ describes a line parallel with the beam. $\eta=1.2$, the cutoff for most of the barrel detectors, is an angle 33.5° off the beam line.

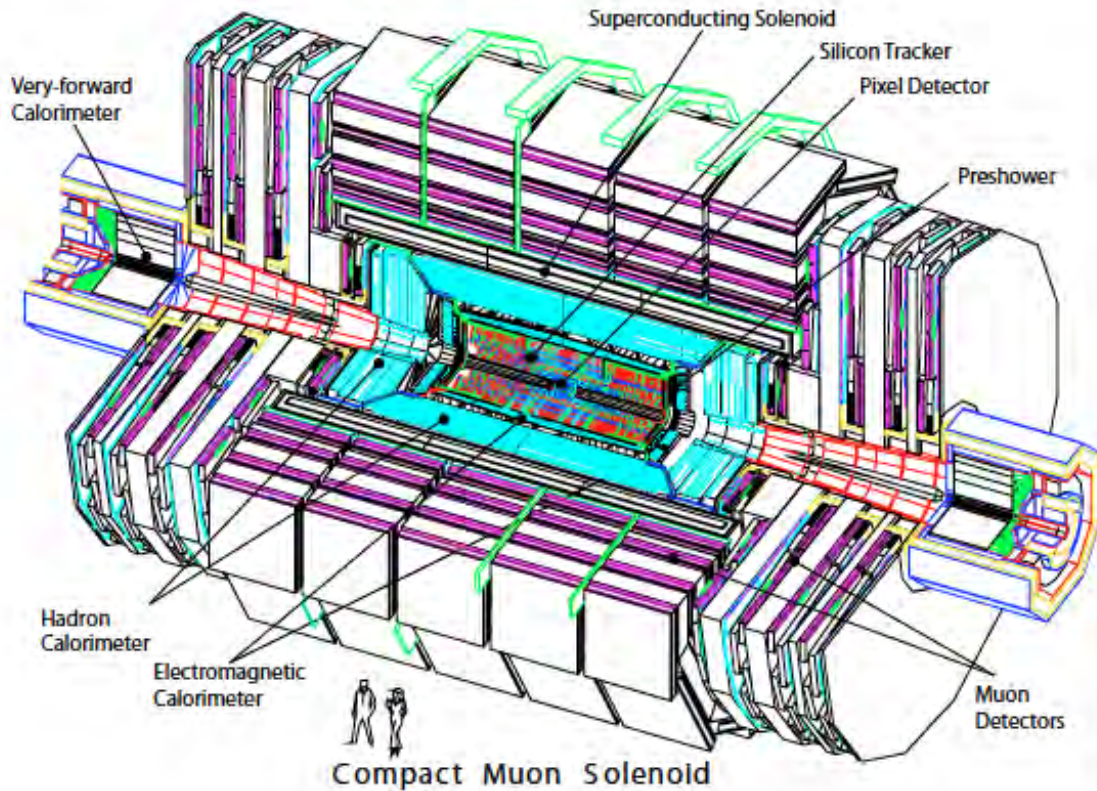


Figure 1: Inside of CMS. Picture Ref: CMS TDR [1]

2.1 Detectors in CMS

2.1.1 The Muon Detector

The outer shell of CMS is the muon detector. It is a detector array consisting of 3 different types of muon detectors: Drift Tubes, Cathode Strip Chambers, and Resistive Plate Chambers. For the details of the workings of these detectors, please see the section 3.1 of the CMS TDR [1].

2.1.2 The Solenoid

Directly inside of the muon layer is the super conducting solenoid. This produces a 3.8T magnetic field inside of it for the purpose of bending particles in order to investigate their momenta. The uniform magnetic field inside of this detector provides a method of converting a curvature of a particle into a momentum, which can then be translated to energy once the identity of the particle is known. The inner radius of this solenoid is about 3m, so the HCAL, ECAL, and the silicon tracking make up only about 15% by volume of CMS.

2.1.3 The Hadron Calorimeter

The HCAL lies inside of the solenoid and is used for finding the energies of hadrons resulting from different particle events. The HCAL barrel portion achieves this with layers of metal (mostly brass) plates sandwiching scintillating crystals. The HCAL also includes an outer hadron calorimeter; it is a thin layer of scintillating crystals placed just outside the solenoid. This outer layer is used to measure how much of the hadron shower is missed [1]. The hadron endcap contains similar detectors oriented in a direction consistent with capping the cylinder. The hadron detector layer is unique in its inclusion of a forward detector to cover angles even less perpendicular to the beam line than the typical endcaps ($3.0 < \eta < 5.0$ instead of $1.2 < \eta < 3.0$). muons will deposit very little energy in this layer and can therefore be tracked and measured in the outer muon layer.

2.1.4 The Electromagnetic Calorimeter

Below the HCAL is the electromagnetic calorimeter (ECAL), which is used to measure the energies of photons and electron resulting from events. The ECAL consists of many lead tungstate crystals that emit light with a short distance of interaction and in a short amount of time, but fail to produce much light per energy of incident particle. The light is therefore amplified and readout with 15 bits of precision (over a dynamic range) [1]. The endcaps of the ECAL are made of the same material. Both heavy hadrons and muons will deposit minimal energy in this layer, so that accurate readings can be taken as they move to the outer layers.

2.1.5 The Silicon Tracker

Closest to the beam line is the silicon tracking layer, which is a series of cylinders made from silicon strip detectors and, in the case of the innermost layers, silicon pixel detectors. This set of detectors extends to a radius of approximately 1.2m. Silicon detectors are strips of metal placed on top of two layers of alternately doped silicon making what is essentially a

very large diode this allows them to detect the current of charged particles passing through them, and this can be read out directly. The spatial resolution is limited by how small the metal plates can be created, as a voltage change only allows for the information that the particle hit somewhere on the plate. This can be improved somewhat if the particle goes in between two plates and leaves some charge on each, as then the charges can be shared to determine where in between the plates the particle passed. The silicon pixel detectors have three layers with radii 4.4cm, 7.3cm, and 10.2cm away from the beam line, and provide accurate 3 dimensional location data for charged particles passing through them. Between 20cm and 55cm are silicon strip detectors, which sacrifice one dimension of resolution in space for a large savings in readout electronics, and out wide of this range are still larger silicon strip detectors, for a total of ten layers. The problem of spatial resolution in strip detectors can be somewhat resolved if 2 layers are positioned closely together with the strips in an slightly off parallel and one event fired relatively few strips; this is performed by using the data in both layers to pinpoint the exact 3D location where the particle must have been if it went through both strips.

Despite being thick, which can cause a particle to change trajectory, silicon detectors can accurately measure positions of particles that pass through them. This high precision in position leads to another well-defined measurement: transverse momentum (p_T). Due to the solenoid's magnetic field being parallel to the beam, from electromagnetism, a charged particle will bend while moving in the transverse, or perpendicular, direction of the beam. A particle's radius of curvature can be determined based only on 2 points, and p_T can be directly found from magnetic strength and radius of curvature. Precisely, if CMS is in a cylindrical coordinate system with the beam line as the z axis, ϕ being the angle, and r the radius, then it is in the r direction (ϕ cross z). Since the transverse momentum is always oriented away from the middle of the detector, the sign of the momentum is used to indicate the charge of the particle (and therefore which direction it will curve in the magnetic field). It is possible to measure the total momentum, given the angle between the transverse plane and the particle. By measuring a component of the momentum, it is possible to obtain the full vector quantity of the momentum. These determinations can only be made if the particle's initial position is directly on the beam line, as the most energetic particles will be.

2.2 CMS: Triggering

At design specifications events occur in the center of the detector at a rate of 40MHz. Each event produces approximately 1 MB of detector data, which corresponds to a data rate of 40 TB/s. It is not feasible to write data out at this rate, much less store it. Therefore there

is a system of triggers which quickly identifies which events are interesting, and thus which events to store. These triggers are adjusted based on what kind of physics is being studied at a given time, but they eventually reduce this data to write rate to 100 Hz. As a quick note, currently write rate at CMS is 300 Hz. This reduction is done in two stages: the Level-1 (L1) trigger and the Higher Level Trigger (HLT). The L1 trigger brings the data rate down to 100kHz, but can only do so much, as it must make decisions at the full detector rate and is limited by processing time. In order to react this fast this trigger must be implemented in custom hardware, which limits the complexity of the algorithm, as complexity scales price and size of the component quickly. Triggered events are then passed to the HLT which is implemented in software, and so can run with more complexity at the slower rate. As an example, the L1 muon trigger takes data from all of the detectors in the muon layer and decides if a muon is likely, if so, the event is passed to the HLT, which then uses the data in the muon layer and the silicon tracking layer to reconstruct the muon track and determine its momentum and energy [1]. The HLT can implement different types of tracking algorithms on the data; many start first from the calorimetry layers and muon systems to reconstruct objects, creating partial tracks. If these hits are not rejected by the trigger, this information can then be combined with information from the tracking layer in order to get the exact path of the particle. This is a process known as tracking. Currently, the L1 trigger does not implement any form of tracking but leaves that process to the HLT. The reasons for not including a track trigger before the HLT are historical. When CMS was first envisioned back in the late 1980's, lower level triggers with track reconstruction were seen as ineffective. CMS also made a large gamble in only using two triggers, whereas almost all detectors use three. CMS projected the developments in computing would be ready to handle the large computational demands present for processing the high rates of events to the HLT by the time the LHC turned on. With an already robust calorimetry and muon system, and low amounts of interactions per bunch crossing, there was no immediate need to include another trigger or any sort of lower level tracking.

2.3 CMS: Tracking

By using all of the information on all of the layers together, CMS can identify tracks. Since this is done with the HLT, the algorithm can be relatively involved and, indeed, is a 5 step process. By first starting with the clusters of hits from the pixel and strip detectors, seeds, or two closely spaced hits, are generated from the innermost layer. By projecting the trajectory of the seed outwards, the tracker moves through a pattern recognition phase. After sorting out fake and duplicate tracks with combined data from the other layers, the tracker

finally assigns a fit to the track. The pattern recognition requires that a variety of possible paths through the hits be processed. The possible paths can be computed because the solenoid maintains an almost constant, well known magnetic field over the tracker volume. This whole process is effective, but its complexity necessitates that it be implemented in the HLT. For more information on the tracking process, see section 6.4 of the CMS TDR 2006 (p.240) [1].

3 LHC Upgrade in 2020: SLHC

After an extended period of continual operation, the LHC will be shutdown in order to upgrade the machine and its detectors. From 2010 to 2020, known as Phase 1, the LHC will work towards achieving design energy and luminosity. Two long shutdowns will occur in 2013 and 2017 to prepare the machine to reach full 14TeV energy and $2 * 10^{34} cm^{-2}/s$ luminosity. A more substantial upgrade to the machine and detectors will come around 2020, termed Phase 2, in which the machine will have another long shutdown to prepare the LHC and its detectors for a factor of 10 increase in luminosity. [2]

This upgrade in 2020 will move the LHC to the SuperLHC (SLHC). The upgrade will seek to increase luminosity from $10^{34} cm^{-2}/s$ to $10^{35} cm^{-2}/s$. This will significantly increase the number of particle collisions per bunch crossing, mainly by increasing the number of protons per bunch. Currently, CMS is operating at around 8 interactions per bunch crossing. At SLHC luminosities, there will be on average 200 interactions per bunch crossing, assuming bunch crossings will occur every 25 ns. CMS is not currently outfitted to handle such high collision rates. The L1 trigger rate as it is now at CMS flattens out with p_T threshold, due to a poor momentum measurement in the current L1 muon system. The detector components are not robust enough to distinguish so many particles at such high occupancy. At luminosities around $10^{35} cm^{-2}/s$, the current trigger fires at a rate well over 20 kHz for muons, which is hoped to be reduced by a factor of 100 [3].

After ten years of operation, the inner components of the detector, specifically the pixel detector and the silicon tracker, will have to be replaced anyway. At this time, these components will have been so significantly radiation bombarded that most of the electronics will no longer be fully operational. This is in part due to the fact that the radiation from the collisions will destroy the crystal lattice of the silicon, and thereby fry some of the electronics permanently. The shutdown will provide an excellent opportunity to replace the tracking layers.

As stated previously, the current trigger at CMS uses a two level triggering system, but the new tracking detector will require a new trigger. With SLHC luminosities, the L1

trigger would trigger on muons much more often, thus overloading the HLT in its ability to select the important events in which to save. To reduce the load placed on the HLT, there is significant interest in implementing track reconstruction in the L1 trigger for the upgrade. This presents a significant challenge, as the hardware necessary would have to be incredibly precise and fast to process the extremely high occupancies in the silicon trackers created by such large amounts of pileup, or additional interactions created per crossing.

Hardware is significantly faster than software in analyzing and computing transverse momentum given a set of hits, which gives a motivation for providing tracking information to the L1 Trigger. Once a collection of hits from each event is found, this information can be immediately passed to the L1 trigger composed of high-speed electronics. Through the use of field programmable gate arrays (FPGAs), the hardware could quickly sort out matched tracks from fake or incomplete tracks. FPGAs consist of an integrated circuit whose logic can be configured after production and any time after implementation. Depending on the physics that is being investigated, certain cuts can be placed on the trigger, in which many events can be rejected based on acceptance in p_T and location in ϕ and η of the actual hits by changing the logic in the FPGA.

4 CMS Upgrade Geometry

For the purpose of the upgrade, different geometries are being investigated for the silicon tracker than the one currently in place at CMS. The silicon tracker geometry that was investigated for this study was long barrel straw-man. [3] The long barrel extends the full length in the beam direction. In order to cover a complete circle around the beam, the cylinder is divided into alternating sliced layers. The full geometry is shown below.

In this geometry, there are no forward end caps. In order to catch near parallel tracks, four other forward barrel stack layers are added at 180cm in the z direction. The stacks are spaced radially at 32cm, 35cm, 48cm, 52cm, 98cm, 102cm, and with the forward barrel stacks at 64cm, 68cm, 80cm, 84cm. The tracker extends to 275cm in the z direction. Each layer in the above diagrams has two sides of sensors, together that layer makes a stack. A pair of connected hits in a stack is known as a stub. In the upgrade to CMS, there will not be silicon strip detectors, as all layers will use only silicon pixel detectors. The sensors to be used are silicon pixels that are $100\mu\text{m}$ by 1mm.

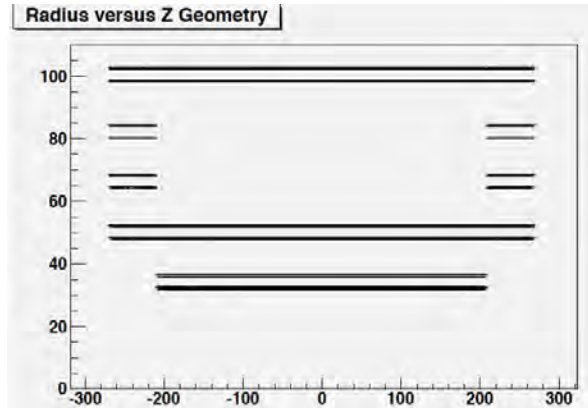


Figure 2: The geometry of the proposed silicon tracker in terms of Z-direction versus the radial distance in centimeters.

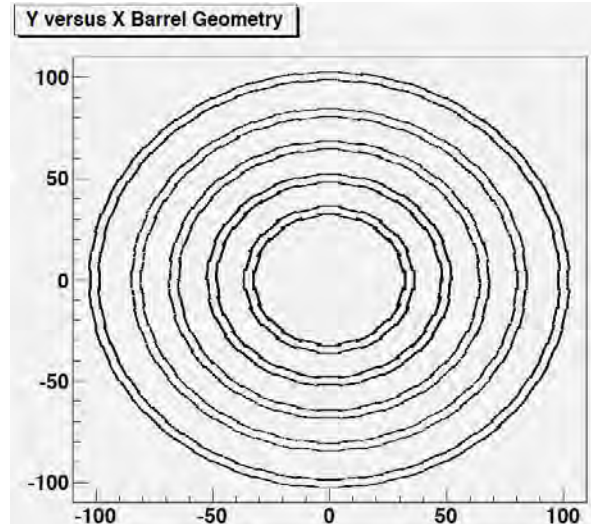


Figure 3: The geometry in terms of Y versus X, showing the concentric cylinder cross sections. Note that the 3rd and 4th double layers are only present on the forward barrels.

4.1 Path Computation

Using software release CMSSW_3.3.6, Monte Carlo simulation studies done in Fast Simulation were first performed as to how well this geometry could match actual hits with simulation truth information. This was first performed with single track events without pileup. For the sake of simplifying the study, η was restricted to 1.2 to exclude the forward barrels. The efficiency of finding all the stubs created for single track 5 GeV/c muons was very close to one hundred percent. Charged pions and electrons at 5 GeV/c were fairly similar to each other, staying around 97 to 93 percent per stub layer. Upon moving to real events, such as high p_T QCD events and Higgs to four lepton events, the efficiency remained exceptionally high. After this initial testing was completed, confirming the usefulness of the new geometry, a new algorithm was developed based on intersecting concentric circles. Charged particles in the detector are assumed to travel in perfect circles in the transverse direction due to the magnetic field of the solenoid. Due to the symmetry of the cylinders, it is possible to reconstruct the path of the particle in ϕ given a hit in any layer. For the purposes of this algorithm, it was assumed that tracks that were worth saving made it all the way to the furthest layer in radius, at 102cm, shown in the figure as r_6 , and high η events that left stubs in the forward barrel were ignored. From this, a position in ϕ is calculated per layer by projecting the track back to the vertex. See Figure 4 and Equations 1 and 2 for an example.

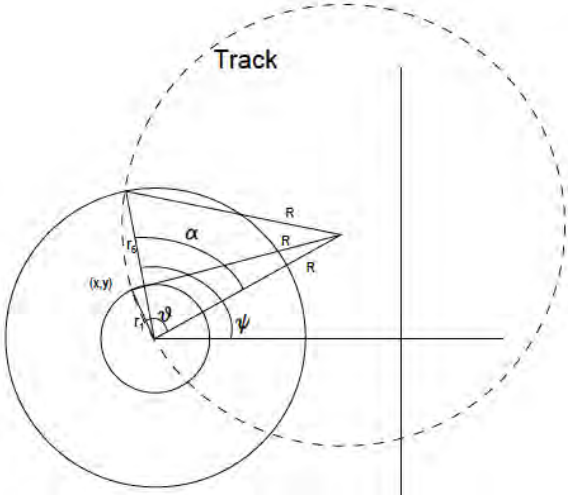


Figure 4: Calculating Tracks

$$x = r_1 \cos(\phi - \cos^{-1}(\frac{r_6}{2R}) + \cos^{-1}(\frac{r_1}{2R})) \quad (1)$$

$$y = r_1 \sin(\phi - \sin^{-1}(\frac{r_6}{2R}) + \cos^{-1}(\frac{r_1}{2R})) \quad (2)$$

This equation allows calculation of track position on a lower layer given only the position of the outer stub and R, the radius of curvature (or p_t).

X and Y can then be converted into a detector ϕ position.

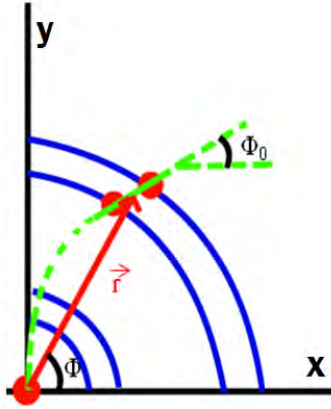


Figure 5: Calculating Stub p_T

$$p_T = \frac{(.3)(3.8)\frac{r}{2}}{\sin(\Phi_0 - \Phi)} \quad (3)$$

.3 is the value of the physical constants in front of that equation. 3.8 is the strength of the magnetic field in Tesla, while the other variables are defined as in the picture.

4.2 Stub p_T

Stub p_T is measured by taking the two closely spaced hits in a given stub, and by projecting a circular curve back to the vertex, the curvature from the magnetic field gives a transverse momentum. At higher momentum, tracks bend less, and the angle between the hits on a stub becomes significantly smaller, reducing the precision in the momentum measurement. At momenta above 50 GeV/c, the difference between angles becomes so small, the sign of the curvature actually becomes ambiguous, as positive and negative curvatures can no longer be accurately determined. Figure 5 shows how stub p_T is visualized.

As shown in Figure 6 (See online for color), momentum resolution quickly falls off towards higher momentum tracks, around 5 GeV/c, often considered the cutoff for high momentum. If cuts were to be placed on tracks, it is guaranteed that true 2 GeV/c tracks

will not be measured above 5 GeV/c, and true 5 GeV/c tracks will not be measured below 2 GeV/c. For the purposes of designing a tracking algorithm, using stub p_T measurement as a cut can greatly reduce both the possibilities of stubs for building tracks and thus reducing the chances of finding fake tracks. Additionally, although not shown, tracks that are 100 GeV/c, will never be measured lower than 10 GeV/c, which can be useful in placing cuts on tracks associated with high momentum used for track finding to reduce fake tracks.

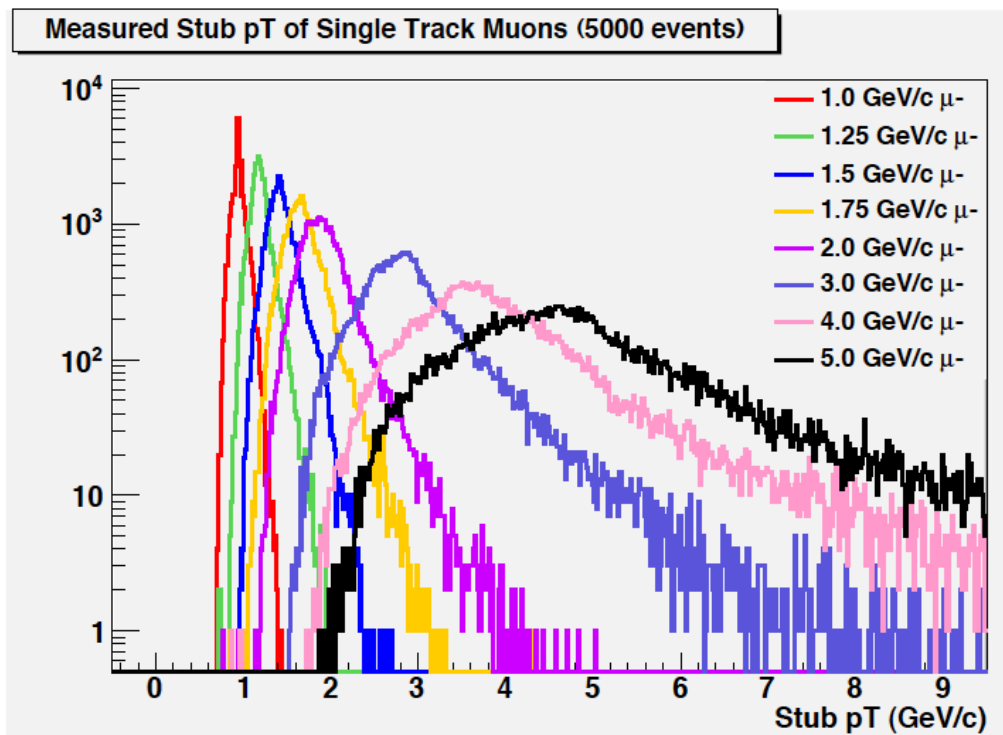


Figure 6: Range of stub measurements of p_T for different incident muon energies.

5 CMS Upgrade Tracking

Due to the increased luminosity (both instantaneous and absolute), the triggering system needs to be improved to handle the increase in detector occupation. The method which was investigated for this is an upgrade to the L1 triggering system which incorporates tracking, and, through this, p_T estimation. By incorporating track information into the L1 trigger, the rejection rate for the L1 trigger can be increased significantly, which would allow the amount of data being sent to the HLT to remain constant with the increased event rate entering the L1 trigger.

5.1 First attempt: Stub p_T Matching

The first method of track finding we attempted was matching stub p_T s from the sixth layer based on a computed uncertainty function in the measurement. For the purposes of this investigation, we are focusing only on the barrel portion of the long barrel, and so the sixth layer refers to the outermost layer. This attempt was not successful, as the momentum uncertainty was very large (and asymmetric) when measured, and so many of the stubs contained overlapping momenta. The uncertainty was so large because the layers forming the stubs are so close together, and so there is little ability to see the effects of the curvature of the particle in a magnetic field. This resulted in the algorithm being overwhelmed by the number of matches, and therefore producing little to no interesting information. The number of matches can be decreased substantially by requiring that the stubs lie, with some degree of uncertainty, on a straight line from where they were produced. This is a straight line in the r-z plane, and starts at a z value between -10cm and 10cm, narrowong to a point at the sixth layer. The SLHC interaction point is expected to have an error of 5cm in z.

5.2 Final Approach: Curvature Bins

Even using this z cut, matching stub measured p_T was unsuccessful in singling out tracks, so we decided to ignore the reported p_T at first and only use the location of the stubs for information. So instead we started from the assumption that any stub in the sixth layer was formed by a particle starting at the center which passed through all six layers and left stubs. We then set out to invesigate what p_T it might have had. This was done by creating ranges in p_T which, when converted to their corresponding curvature and intersected with the lower layers, corresponded to specific ranges in ϕ . These ranges in ϕ are refered to as ϕ bins. The cut in the z axis was left in, as it still is an effective way to shrink the stub space. We started by creating 100 bins spaced in momentum such that they subtended equal ϕ ranges. This caused the momentum resolution to decrease as momentum increased, but this was not unexpected, as particles tend to take paths that approach a straight line as momentum tends toward infinity. When these bins were implemented with no overlap, the efficiency vs p_T plot contained oscillations due to the fact that some particles with a momentum near the bin boundaries would fail to have all hits in one bin or the other, and so there would not be a hit on each layer in the bin. To fix this problem, we had to define overlapping bins, which was done by defining the bin centers with a given amount of slop. Slop is a quantity which scales the bin widths linearly in curvature. The lowest and highest curvature bins presented were exceptions, as 0.5 slop corresponds to bins, which completely fill momentum/curvature space, but have zero overlap, while 1.0 slop means that a bin will extend from the center of

the bin before it to the center of the bin after it. This slop value is a parameter which we adjust based on binning. Higher slop values will lead to a higher efficiency of track finding at the expense of a higher fake rate. This method of binning tended to slice the lower part of the momentum spectrum much too finely, to the point that efficiency was lost below 5 GeV/c depending on the exact parameters. If slop was increased to bring this efficiency up, then the resolution on the higher end of the p_T spectrum was decreased by too large of a factor to be useful.

Our first attempt to resolve this issue was to allocate a set number of bins for different parts of the momentum spectrum (while still keeping a total of 100 bins), but this merely resulted in the spectrum being sliced too finely in two spaces instead of one. As this indicated that 100 bins was too many, we decided to merge the lower bins until a specific threshold was met, but this either did not fix the problem, or created too few bins. Another tack we took was to plateau the p_T ranges of the smaller bins, or dynamically increase the slop such that these bin widths never got smaller than a given p_T or ϕ range, but this tended to result in absurdly wide bins at low momenta (the same ϕ point being covered by 10+ bins). Finally we came to the conclusion that we needed to decrease the number of bins to get efficient ϕ coverage. We used linear p_T steps (of varying size) on the low momentum end of the spectrum and switch over to the equal curvature slicing starting at 10 GeV/c.

In the final iteration of this custom binning, there was one bin from 0.1 GeV/c to 2 GeV/c, followed by linear steps of size 0.2 GeV/c from 2 GeV/c to 4 GeV/c, then linear steps from 4 GeV/c to 6 GeV/c of size 0.5 GeV/c. After this, the 100 bin equal curvature function from 2.0 GeV/c to 300 GeV/c is called for the last 33 bins (there are 33 bin between 6 and 300 GeV/c in that binning, which gives an estimation of how finely sliced the low p_T bins were before the linear step sizes). The final bin is from 300 GeV/c to -300 GeV/c. The very high momentum tracks all move straight through the detector, and so tracing continuously through ϕ space is equivalent to tracing through infinite momentum and coming back from negative infinite momentum. As such, the mid-

Bin:	Cent_pT:	LowpT:	HighpT:	Bin:	Cent_pT:	LowpT:	HighpT:
0	3000.00	-300.00	300.00	25	8.00	7.75	8.26
1	171.92	102.15	300.00	26	7.69	7.45	7.95
2	92.74	67.77	146.84	27	7.41	7.17	7.67
3	63.49	50.70	84.91	28	7.15	6.91	7.41
4	48.27	40.50	59.73	29	6.90	6.66	7.16
5	38.94	33.72	46.06	30	6.67	6.43	6.93
6	32.63	28.88	37.49	31	6.46	6.22	6.72
7	28.08	25.26	31.60	32	6.26	6.02	6.52
8	24.64	22.44	27.31	33	6.25	5.85	6.65
9	21.95	20.19	24.05	34	5.75	5.35	6.15
10	19.80	18.35	21.49	35	5.25	4.85	5.65
11	18.02	16.82	19.41	36	4.75	4.35	5.15
12	16.54	15.52	17.71	37	4.25	3.85	4.65
13	15.29	14.41	16.28	38	3.90	3.65	4.15
14	14.21	13.45	15.06	39	3.70	3.45	3.95
15	13.27	12.61	14.01	40	3.50	3.25	3.75
16	12.45	11.86	13.10	41	3.30	3.05	3.55
17	11.73	11.20	12.30	42	3.10	2.85	3.35
18	11.08	10.61	11.59	43	2.90	2.65	3.15
19	10.50	10.08	10.96	44	2.70	2.45	2.95
20	9.98	9.60	10.39	45	2.50	2.25	2.75
21	9.51	9.16	9.88	46	2.30	2.05	2.55
22	9.08	8.77	9.42	47	2.10	1.85	2.35
23	8.69	8.40	9.00	48	1.00	0.10	2.00
24	8.33	8.06	8.61				

Figure 7: Center and boundary values for p_T bins

dle bin contains very positive and very negative momenta. The bins are symmetric and there are a total of 48 bins on each side and 1 in the middle making 97 bins in total.

At first we used a slop of 1.2 to get a reasonable efficiency plot, but then we realized that we were using a magnet strength of 4.0T when we should have been using a strength of 3.8T. This caused errors in the proper p_T binning. We were then able to decrease the slop to 0.8 without a significant negative impact to the efficiency plot. One final upgrade to our algorithm was to remove all of the stubs which reports less than 2 GeV/c for their momentum. The current binning scheme is seen here in Figure 7.

6 Efficiencies and Fake Rates

In order to test the efficiency of our tracking algorithms we first tested them on a spectrum of single muon tracks. These tracks should be the easiest to find, as muons are one of the most penetrating particles through the detector material as evidenced by the enormous volume of the detector devoted to detecting only them.

Muons also have a small chance of interacting and being deflected, and their large mass means they radiate less, which makes their tracks very close to perfect circles and don't produce additional tracks due to radiation. The muon efficiency plot from 2 GeV/c to 1 TeV is seen in Figure 8. Note that the initial very low values for 2 GeV/c and 3 GeV/c are due to cutting out stubs which reported below 2 GeV/c. The uncertainty on the stub measurement, even at this large angle of curvature, ensures that many of these stubs will get cut and hurt the track efficiencies. The effect abates above 3 GeV/c because the uncertainty range does not reach that low for higher momentum tracks. Between 6 GeV/c and 10 GeV/c, there is a small dip due to the change of styles of momentum measurements. After 10 GeV/c, it remains flat save for 2 dips: one at about 200 GeV/c and about 400 GeV/c. These features of the efficiency plot are not well understood, but are likely due to how particles at these energies are deflected and where the bin cuts occur in curvature. Also see Figure 9 for a detail of the lower p_T range of the same plot.

As a test of how this would affect a trigger, "MinBias" events were analyzed. A minimum bias event is what we expect to constitute a pileup event. In order to get an estimate of how often this algorithm would find a nonexistent track at high p_T s, the algorithm was run on 200 thousand individual minimum bias events and the highest momentum fake for a given event (if there were any) was placed in a histogram. The overplotted histogram shows this without vetoing stubs less than 2 GeV/c versus the effect with vetoing Figure 10. Unfortunately, these fake rate do not scale linearly with detector occupancy, but this is a good starting estimate of algorithmic performance. Assuming it is possible to look at only

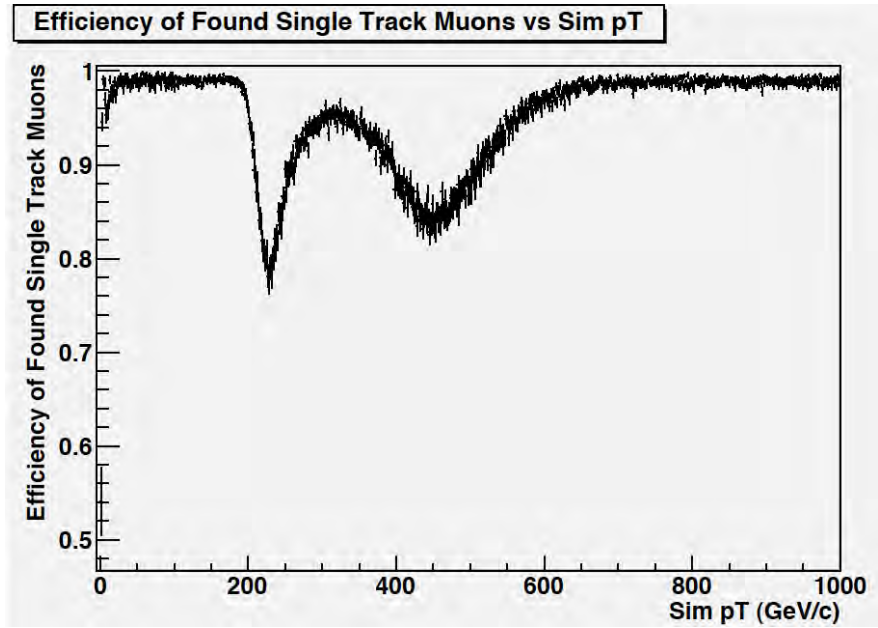


Figure 8: Efficiency of finding muon tracks in the range 2 GeV to 1 TeV

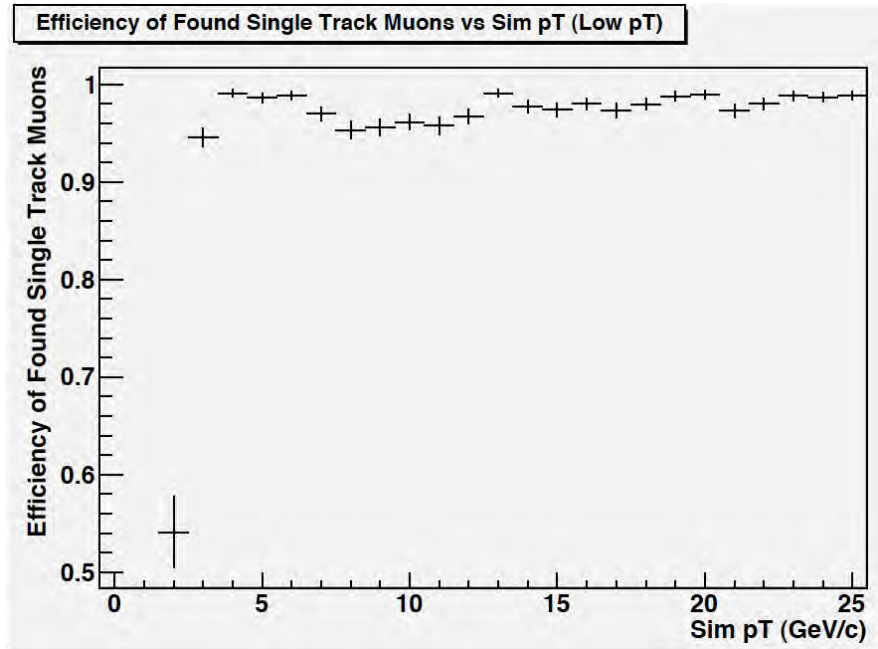


Figure 9: Efficiency of finding muon tracks in the range 2 GeV to 25 GeV

1 MinBias event in the detector, that these events occur with cross section 71mb , and that the LHC is operating at luminosity $10^{34}\text{cm}^{-2}/\text{s}$, then one fake on this plot corresponds to a readout rate of about 3.6kHz . This estimation needs to be taken with a grain of salt not only due to the nonlinearity of the effect, but also due to the fact that only a few counts are

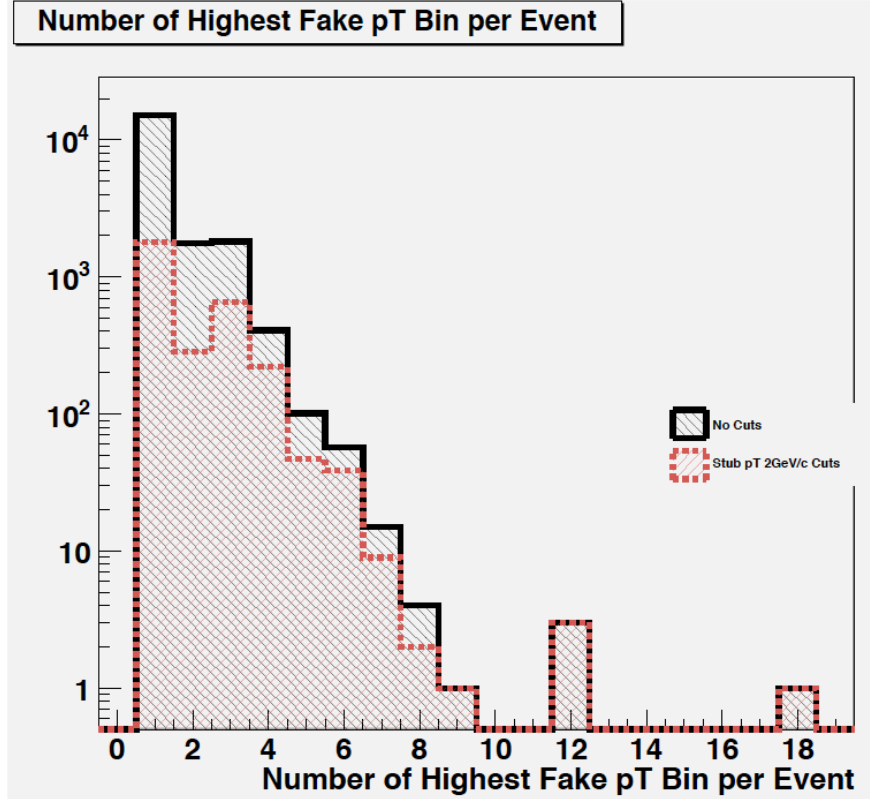


Figure 10: Highest p_T fake in 200 thousand MinBias events

obtained above 10 Gev, so the uncertainty on the rate of counts is quite high.

7 Future Investigation

The algorithm developed for the new geometry has performed well under single track events without pileup. The tuning of the algorithm presented a unique challenge; selecting the best types of ϕ bins, the proper amount of ϕ bins, and slop in ϕ each took time to compile and analyze. Due to the improper magnetic field constant being used in our algorithm, a significant amount of overestimation in slop was given for high momentum, resulting, initially, in very high fake rate. Further study is needed to optimize the algorithm, investigating different slop values, tuning the number of ϕ bins, and how to bin in ϕ . The algorithm should also account for high η tracks, and incorporate the forward barrels into the algorithm as well. In addition, once the optimal algorithm has been determined, single track events with pileup as well as realistic events with pileup will need to be studied. If the algorithm proves to operate well under high amounts of pileup, with high efficiency of finding real tracks and low fake rate, then this algorithm should be moved to a simulated FPGA code.

Upon successful implementation into hardware code, the algorithm should move towards actual production in hardware to be tested for integration into the new silicon detector for CMS.

8 Acknowledgements

We would first like to thank our advisors, Professor Michael Hildreth and Professor Kevin Lannon for all of their guidance and help. They both provided an excellent working environment through their experience and expertise, while maintaining a light-hearted attitude conducive to a healthy atmosphere.

We would also like to thank the graduate students, Jamie Antonelli and Sean Lynch, who were very helpful in answering questions related to NDCMS, the Condor computer cluster, concentric circles, and ROOT. They were great sources of entertainment when the computers were down.

Lastly, we would like to thank the University of Notre Dame, the REU program, and the Notre Dame Physics Department for their support in this research. We would like to thank NSF and COS-SURF donors for their funding to conduct this research over the summer.

References

- [1] “CMS Physics Technical Design Report Volume 1: Detector Performance and Software.” Ed. D. Acosta. Feb. 2006. Web. <http://cdsweb.cern.ch/record/922757/files/lhcc-2006-001.pdf>.
- [2] The CMS Collaboration. “Technical Proposal for the Upgrade of the CMS Detector Through 2020.” Spring 2011. Web. <http://cdsweb.cern.ch/record/1355706/files/LHCC-P-004.pdf>.
- [3] Mannelli, Marcello. “CMS from LHC to SLHCMotivation for L1 Tracking Trigger.” Feb. 2010. Web. <http://indico.cern.ch/getFile.py/access?contribId=11&sessionId=8&resId=0&materialId=slides&confId=74957>.

Recoil Mass Separator Hysteresis Measurements and Germanium Detector Development

By Robert Heitz

Virginia Tech

2011 NSF/REU Program

Physics Department, University of Notre Dame

Advisors: Michael Wiescher, Ed Stech, Manoel Couder

August 5, 2011

Abstract

A recoil mass separator, St. George, was proposed to study nuclear reactions that control the energy production and nucleosynthesis in stellar and explosive helium burning in inverse kinematics. Dipole magnets will be used to separate out the charged states of the reaction products and filter out background radiation. It is not possible to measure the full magnetic field within these dipole magnets without interfering with the ion beam. For this reason a hall probe was used to measure the magnetic field outside of the strongest magnetic field region of the dipole magnet. Data taken comparing the magnetic field reading on the hall probe to that on a nuclear magnetic resonance probe in the center of the magnet, show the hall probe is sufficient to determine the magnetic field inside the dipole magnet.

Complementing the St. George mass separator is the Georgina project. This project will be used to study stellar burning by efficiently detecting low energy gamma rays from in-beam experiments. In order for the germanium detectors to operate correctly they need to be cooled down to liquid nitrogen temperatures. This is done by filling the detectors with liquid nitrogen and refilling the detectors every six hours. To allow for continuous use of the Georgina project, Labview code was printed on a CompactRIO system to fill the germanium detectors at specified offset times.

Introduction

The Nuclear Science Lab at Notre Dame focuses on nuclear astrophysics. This is the field of study that links nuclear physics to astrophysics by studying the nuclear processes that occur in stars and supernova. The Nuclear Science Lab is specifically interested in studying stellar nucleosynthesis. This is the process in which most elements heavier than hydrogen are formed. The goal of the lab is to determine the origins of elements and to further understand the universe [3].

The Strong Gradient Electromagnetic Online Recoil separator for capture Gamma Ray Experiments or St. George was designed to study stellar helium burning. St. George is a recoil mass separator located in the Nuclear Science Lab at Notre Dame. This separator will be used to study low energy reactions in inverse kinematics for beam masses with an atomic number as high as 40. Alpha capture reactions are important in stellar helium burning and affect the formation of heavy nuclei through nucleosynthesis. Low energy proton or alpha particle beams are traditionally used to study these reactions. The St. George provides the possibility to use heavy ion beams to bombard a ^4He jet gas target; the heavy ion recoil nuclei produced by alpha capture reactions in the gas jet are separated from the intense primary beam by the St. George separator. St. George is made of six dipole magnets, eleven quadrupole magnets, a Wien filter, and a detection system [1]. The project is broken into three sections. The first section chooses a certain charged state from the heavy ion recoil beam. Once the heavy ion beam collides with the helium gas target, the small percentage of heavy ion recoil products are of many different charged states. The first section on the St. George allows only the selected charged state to pass. This is done using dipole magnets to bend the other charged states too little or too much. Section two separates the heavy ion recoil from the original heavy ion beam by selecting only particles of a certain velocity. Due to conservation of momentum, the heavy ion recoil and the original heavy ion beam have the same momentum after the initial collision with ^4He jet gas target. The recoil product, however, has a higher mass and therefore a slower velocity than the starting ion beam. This makes it possible to separate the two beams by using perpendicular electric and magnetic fields. The final section of St. George is the detection stage. This section uses two targets to further filter the heavy ion recoil from the beginning heavy ion beam. The first target starts timing once the total beam collides with it and the second target, a distance away from the first target, determines the energy of the total beam. The amount of heavy recoil can then be

determined, using the time and distance to get to the second target along with the energy of the beam.

Georgina, which stands for Ge-detector Online aRray for Gamma ray spectroscopy In Nuclear Astrophysics, was designed to efficiently detect gamma rays from in-beam experiments. Georgina will also be a part of the Nuclear Science Lab at Notre Dame. The Georgina project will give additional data on low energy stellar burning experiments, which St. George cannot supply. Georgina can be used in alpha capture reactions along with St. George, and Georgina can collect data on proton capture experiments, which St. George cannot supply information on. Georgina consists of five germanium detectors which can be arranged in different formations to reduce background interference and more efficiently detect gamma rays [2]. Georgina and St. George will broaden the experimental techniques at the Nuclear Science Lab and help further understand fundamental concepts of the universe.

Georgina Code

The Georgina computer code is written to start experiments, continuously run experiments, and be accessible anywhere in the Notre Dame network. This code is written in Labview using a while loop to ensure the program runs continuously. The code also consist of a series of nested while loops to starting filling tanks with liquid nitrogen, set an offset time between the time the liquid nitrogen tanks are filled, indicate if a failure has occurred, and to reset the program. The program is written to fill the five germanium detectors one at a time, and then wait a set amount of time before refilling the detectors. LEDs are used as sensors to tell the program when the tanks are full of liquid nitrogen. When liquid nitrogen cools the LED sensors the resistance across the LEDs decreases which raises the voltage read by the program. Once the voltage is above 2.2 volts the program reads the tanks as being full. To ensure that the LEDs do not falsely indicate that the tanks are full, the program requires the tanks to fill a minimum amount of time before they can be considered full. This means the LED sensors must go off and the minimum amount of time specified must be reached before the next tank can fill. Additionally if the tanks take too long to fill, meaning a problem with the filling has occurred, the program will skip through any tanks left unfilled and indicate a failure has occurred.

Failure

The failure loop was written to prevent liquid nitrogen from being wasted in the case that a tube unconnected or an LED breaks. The failure indicator can be undone by pressing the reset button. The program will run in the failure loop until the reset button is pressed allowing for time to fix problems with the filling system.

Start and Reset

The start and reset button was added to allow for manual changes in the program during the filling process. Upon starting the program the start or reset button will need to be pressed to start the tanks filling. No offset time occurs between start and the first filling. After the first filling is started the start button becomes a reset button. Pressing the reset button after a failure occurs starts the program at the beginning of the offset time. This means the program will take the specified offset time to start filling tanks again. Pressing the reset button during the offset time of the program starts the first tank filling again. This means pressing the reset button twice after a failure will cause the tanks to start filling again. Pressing the reset button while the tanks are filling stops the tanks from filling and sends the program back to the beginning of the offset time.

Labview Functions

Loop timer 

The loop timer function begins timing in milliseconds upon being called and continues timing throughout the duration of the program. When entering a new loop the loop timer continues to count but will not display the counting change in the new loop. This means a loop timer in a previous loop will only display the time at the start of the new loop on an indicator in the new loop. When using multiple loop timers, once the first loop timer is called all future loop timers also begin timing. This timing function only keeps track of the amount of milliseconds after it was called and does not work for determining the time of the day.



The FPGA I/O Nodes are used to either monitor the voltage in series with the LED or to turn on an LED indicator on the CompactRIO. Modulus 1 is used to monitor voltages using AI0 through AI4 to determine if the tanks are full and AI16 as the start and reset button. Modulus 2, channels 0 through 3 and modulus 3, channel 0 are used to indicate that a tank is filling.

St. George Dipole Magnets

The six dipole magnets on the St. George will be water cooled to 55 degrees Celsius and will be able to provide a magnetic field up to 0.6 tesla [1]. This will ensure that all the heavy ion recoil charged particles, remaining in the beam, have the correct charged state. The Lorentz force is responsible for bending the moving particles and the first two dipole magnets are used to ensure the Lorentz force thoroughly filters the ions. The particles with the specified charge state will be bent an angle of 26 degrees while all other charged states will be bent more or less and not make it through the exit aperture [1].

St. George Hysteresis Measurements

It was proposed to use a Hall probe to determine the magnetic field that influences the charged particles within the dipole magnet. To prevent the Hall probe from interfering with the ion beam, the Hall probe will be permanently mounted a fixed distance outside the region where the particles travel. The Hall probe will be placed approximately 5.5 inches from the center of the magnet. This position was chosen because a strong magnetic field still resides there while deflected particles will not collide with the probe there. To map out the change in the magnetic field with respect to the distance from the center of the dipole magnet and determine the magnetic field at the position the Hall probe will be mounted, a Hall probe was attached to a linear positioner. The magnetic field was then measured in 0.2 inch increments, up to ten inches, from the center of the magnet. These measurements were performed at five currents corresponding to five different magnetic fields. These currents started at a maximum of 120 amperes and decreasing by 20 percent of the maximum current down to 24 amperes. As shown in figure 1 the magnetic field is uniform near the center of the magnet and then drops off nonlinearly. The region of homogeneous magnetic field is the region where the ion beam will

travel. The position where the Hall probe will be mounted is in the nonlinear region of the magnetic field and is outside the region where the ion beam will travel. The nonlinearity of the magnetic field, in this region, makes it impossible to replace the Hall probe with a more precise Nuclear Magnetic Resonance (NMR) probe. This is because an NMR probe cannot resonate and give accurate results in a nonlinear field.

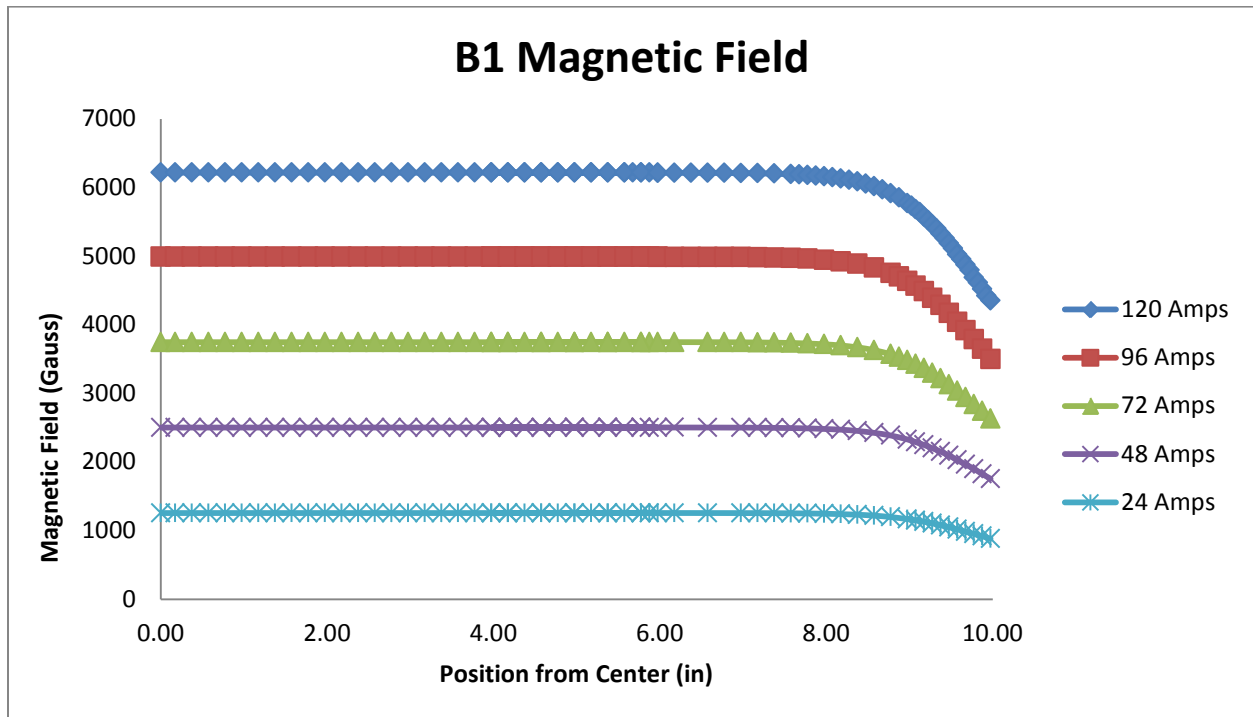


Figure 1. This shows the change in the magnetic field of dipole magnet B1 with respect to the distance from the center of the magnet. The different line graphs represent different currents.

The magnetic field, inside the dipole magnet, does not vary perfectly linearly with the current through the magnet. This is due to the hysteresis of the dipole magnet. In order to stay on one hysteresis curve and make measurements on the dipole magnet, it was proposed to vary the current in one direction only. This means the current must either start at zero amperes and always increase or the current must be increased to the maximum current and then always decreased. When varying the current, the magnetic field must first stabilize at the most extreme current before increasing or decreasing the current.

To determine if a Hall probe mounted 5.5 inches from the center of the dipole magnet is sufficient to determine the magnetic field charged particles experience in the center of the dipole magnet, an experiment was conducted with an NMR probe in the center of the magnet. For this

experiment an NMR probe was held fixed at the center of the dipole magnet and a Hall probe was held fixed in its permanent position approximately 5.5 inches from the center of the magnet. The current through the dipole magnet was then varied and the magnetic field readings on the Hall probe and the NMR probe were recorded. To show the hysteresis of the magnet, the current was varied by decreasing from the maximum of 130 amperes to the minimum of 0 amperes and by increasing from the minimum current to the maximum current. This procedure was done by varying the current in 2 ampere units. This experiment was conducted on the B1 and B2 dipole magnets of the St. George. Figures 2 and figure 3 show that on both magnets the field reading on the Hall probe varies linearly with the reading on the NMR probe. This means that a Hall probe mounted approximately 5.5 inches from the center of the magnet is sufficient to determine the magnetic field within the center of the magnet.

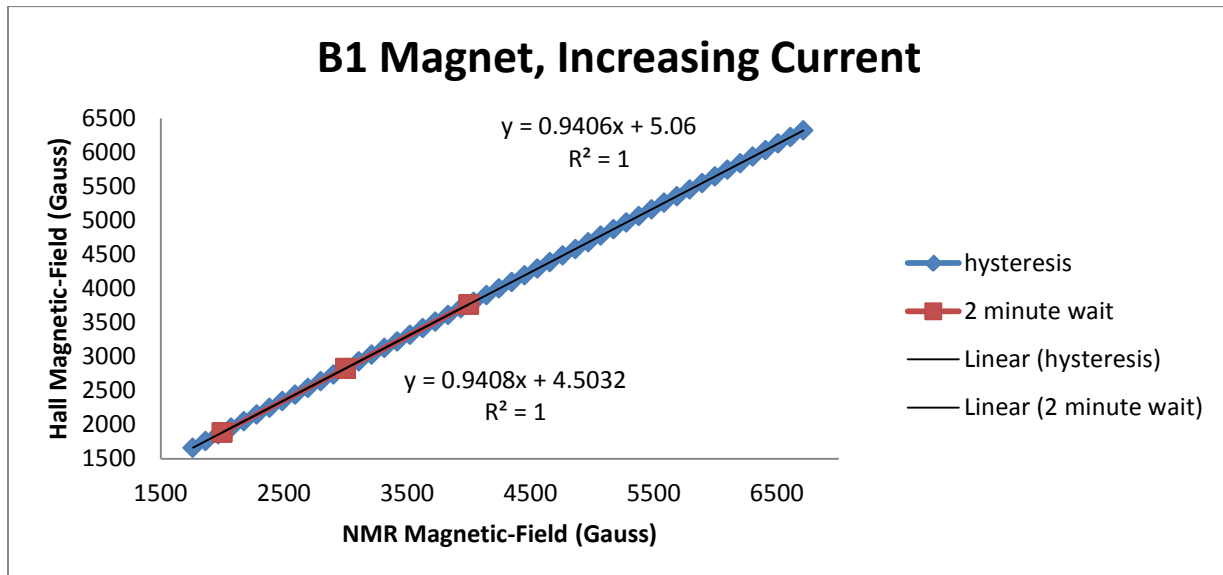


Figure 2. Magnetic field reading on an NMR probe versus the magnetic field reading on a Hall probe and corresponding linear fits of the B1 magnet. 2 minute wait plot corresponds to waiting two minutes at zero current before increasing the current to the chosen magnetic field.

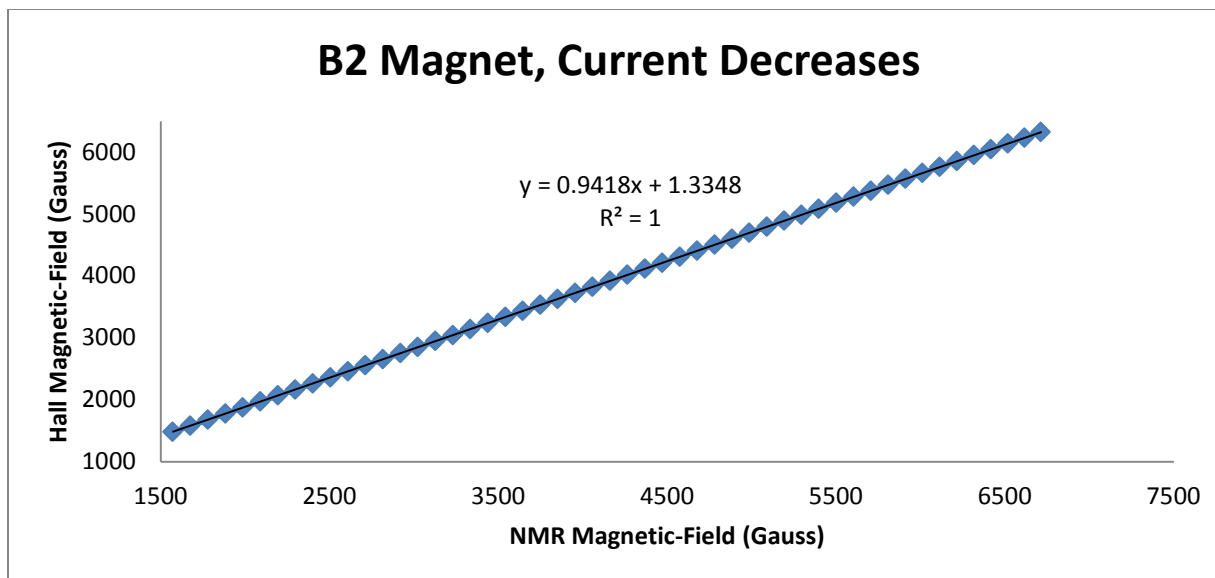


Figure 3. Magnetic reading on an NMR probe versus magnetic field reading on a Hall probe and corresponding linear fit of the B2 magnet. The current always decreased in developing this figure.

An additional experiment was conducted to determine the amount of time needed to allow the magnetic field within the dipole magnet to stabilize. This experiment was performed to find the minimum amount of wait time needed to stabilize the dipole magnetic field. This was done by starting at either 0 or 130 amperes and waiting a specified time before increasing or decreasing to a desired magnetic field. This process was repeated several times waiting ten minutes, five minutes, and two minutes before changing the current. The process was repeated twenty five times for a two minute wait. Figure 2 shows the data from waiting two minutes falls on the hysteresis curve and has a linear fit close to the linear fit of the hysteresis curve. This means waiting at 0 or 130 amperes for two minutes is sufficient time to ensure accurate readings on the magnetic field probes.

Conclusion

The Georgina project is ongoing due to equipment needs and further testing. With the code written for Georgina however, the project only needs minor equipment assembling to begin experiments. St. George is also an ongoing project. Equipment malfunctions have slowed down the development of the project. However, with experimental evidence validating the use of a permanently fixed Hall probe and the hysteresis data on two of the dipole magnets, experiments can be conducted much quicker once the project is completed. Once the Georgina and St. George projects are fully operational the Nuclear Science Lab will be able to perform a wider

range of tests and will have a combination of experimental techniques incomparable to that of any other lab in the world.

References

[1] M. Couder et al. "Design of the recoil mass separator St. George." *Science Direct*. (2007): 35-45. Print

[2] Garg, Umesh et al. "Development of GEORGINA." (2009): Print

[3] "Experimental Research, Institute for Structure and Nuclear Astrophysics (ISNAP), University of Notre Dame." University of Notre Dame. Web. 18 July 2011. <http://www.nd.edu/~nsl/html/research_exp.html>.

Magnetic Fields in a Supernovae-driven, Stratified Disk

Janie Hoormann
2011 NSF/REU Program
University of Notre Dame, Physics Department

Advisor: Professor Dinshaw Balsara

Abstract

It is known that the interstellar medium is highly turbulent, but understanding the effects of that are still an active area of research. Possible sources of turbulence include supernovae explosions, solar winds, and the magneto-rotational instability, but as one of the main contributors, this simulation focuses on the effects of supernovae explosions. These are set up by injecting spheres of high energy near the midplane of the disk. This model sets up a stratified disk, as the interstellar medium varies in temperature with regions of cold gas ($T < 2000\text{K}$), warm gas ($2000\text{K} < T < 10^5\text{K}$), and hot gas ($T > 10^5\text{K}$). The stratified disk is kept in both hydrostatic and thermal equilibrium to prevent the disk from initially collapsing. The size of this disk is set to be $0.5 \times 0.5 \times 3.0 \text{ kpc}^3$. A shearing sheet approximation is used to account for the galactic rotation and the periodic boundary conditions. This research aims to see how the magnetic fields in the interstellar medium are affected by turbulence. To this end, a small initial magnetic field is set up using ABC flows. Preliminary results indicate that the magnetic field is amplified after the supernovae explosions cause turbulence.

Introduction

The Milky Way Galaxy has a radius of 20 kpc with a height of a couple hundred parsecs. However, of that, only a small percentage of the mass of the entire galaxy is from the interstellar medium, or ISM, with most of the matter being confined to the disk (Lequeux 2005). Along with ordinary matter, the ISM contains cosmic rays and magnetic fields. These three components are bound together by electromagnetic forces with comparable pressures (Ferriere 2001).

This matter can be further classified into three temperature groups: cold ($T < 2000\text{K}$), warm ($2000 < T < 10^5\text{K}$), and hot ($T > 10^5\text{K}$). A stratified model takes this temperature distribution into account (Gent 2010).

Turbulence

In a typical spiral galaxy the ISM is highly turbulent (Gressel 2008). This is caused by energy sources such as differential rotation, stellar radiation, high-energy particles, and energy given off from supernovae explosions (Lequeux 2005). Turbulence changes the balance of pressure and gravity to sub cloud scales as opposed to galactic scales, which then may regulate star formation (Joung MacLow 2006). These turbulent fields are established due to the presence of the driving mechanisms mentioned above as well as large length scales and low viscosities (Balsara 2005). During a supernova explosion a shock wave, driven by the pressure of an expanding, hot gas bubble, is set up and moves into the surrounding area, sweeping up gas as it goes (Dyson 1997). Gas in the ISM which has temperatures around a million Kelvin can be created by these explosions. However, this hot gas is confined in bubbles which are a result of clustered supernovae (Brandenburg 2007). Superbubbles can also be formed by stellar winds and supernovae explosions, and chimneys are formed when the expanding bubble runs into the stratified medium (de Avezil 2001).

Magnetic Field

The study of magnetic fields in the ISM is a very active area of research. There are many questions that need to be answered, including what could be potential mechanisms for amplifying the field. Typically, in clouds the magnetic field has a strength of around $12\mu\text{G}$ while in the ISM it is closer to $3\mu\text{G}$ (Passot 1996). The magnetic field is somewhat organized on the galactic scale but, for the most part, the irregular components will dominate. The gravitational

attraction of the disk needs to balance the pressure from high-energy charged particles and magnetic pressure at large scales (Lequeux 2005). The field on large scales is developed by a mean field dynamo but on smaller scales there are faster ways of generating fields (Balsara 2005). The correlation of small scale turbulence and a magnetic field leading to EMF can be described by the generation of a mean magnetic field explained by the α effect (Gressel 2008).

Heating and Cooling

Another aspect that needs to be considered is the heating and cooling of the ISM. The cooling is done by emitting radiation. An atom, ion, or molecule gains energy from collisions and the energy is then radiated as a photon. The gas is heated by processes such as frictional heating, novae and supernovae, stellar winds, x-rays, cosmic rays, and starlight (Dyson 1997).

Description of the Model

When setting up the stratified disk, the model needs to be in hydrostatic and radiative equilibrium. If not, the disk will collapse down to the midplane and be built back up until the pressure caused by turbulence is able to balance the process as done by Gressel (2008). To do this, the gravitational acceleration from Kuijken and Gilmore (1989) is employed such that

$$g_z = \frac{az}{\sqrt{b^2 + z^2}} + \frac{cz}{d} \quad (1)$$

where $a = 4.4 \times 10^{-14} \text{ km s}^{-2}$, $b = 0.2 \text{ kpc}$, $c = 1.7 \times 10^{-14} \text{ km s}^{-2}$, $d = 1 \text{ kpc}$. Following Gent et. al (2010) a temperature function, T , was chosen so that $\frac{\partial \ln \rho}{\partial z}$ could be integrated analytically as

$\frac{\partial T}{\partial z} \propto g_z$ which implies that $\ln \rho \propto -\ln T$ when using

$$T = \frac{T_0}{ab} \left(a\sqrt{b^2 + z^2} + \frac{c}{2d} z^2 \right) \quad (2).$$

This is particularly useful as the hydrostatic equilibrium condition is given by

$$\frac{\partial \ln \rho}{\partial z} = -\frac{g_z}{R_{gas} T} \quad (3)$$

with the thermal equilibrium being described by

$$\Gamma = \rho \Lambda \quad (4)$$

where Γ is the heating function and Λ is the cooling function.

It can be seen in Figure 1 that temperature increases as the distance from the midplane increases, while both pressure and density decrease.

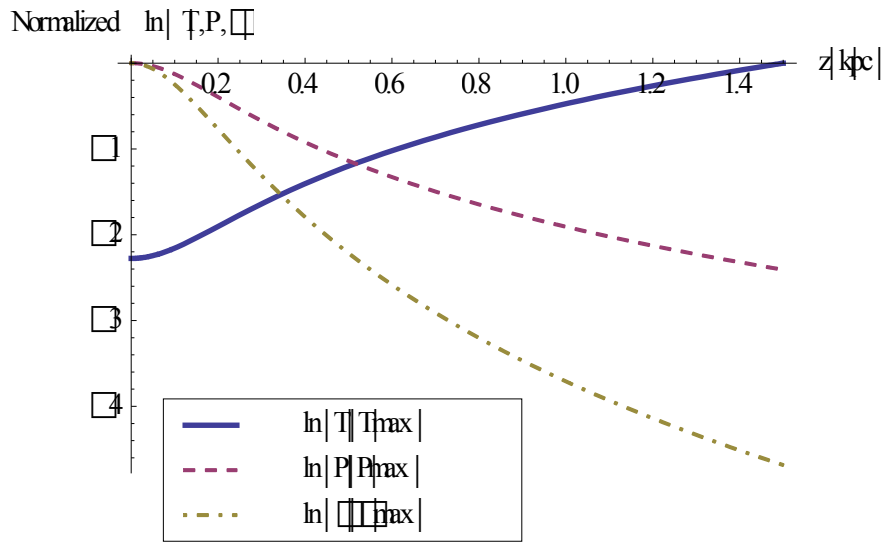


Figure 1: Illustrates the relationship between the normalized temperature, pressure, and density of the stratified model with a distance z from the midplane.

A small, initial magnetic field is set up using an ABC flow which sets the x, y, z components to be

$$\begin{aligned} v_x &= A \sin\left(\frac{2\pi z}{\lambda}\right) + C \cos\left(\frac{2\pi y}{\lambda}\right) \\ v_y &= B \sin\left(\frac{2\pi x}{\lambda}\right) + A \cos\left(\frac{2\pi z}{\lambda}\right) \\ v_z &= C \sin\left(\frac{2\pi y}{\lambda}\right) + B \cos\left(\frac{2\pi x}{\lambda}\right) \end{aligned} \quad (5)$$

where $\mathbf{v} = \nabla \times \mathbf{v}$. (Dombre 1986). This is used to set up the magnetic field by defining the vector potential, \mathbf{A} , using

$$\mathbf{A} = \mathbf{v} e^{-\left(\frac{z}{H}\right)^2} \quad (6)$$

where \mathbf{v} is the vector defined in equation 5, H is the scale height, and z is the distance from the midplane of the disk. The magnetic field can then be found using the fact that $\mathbf{B} = \nabla \times \mathbf{A}$, which provides for a divergence free magnetic field (Balsara 2009).

To model the galactic rotation the values $A = 14.82 \pm 0.84 \text{ km s}^{-1} \text{ kpc}^{-1}$, $B = -12.37 \pm 0.64 \text{ km s}^{-1} \text{ kpc}^{-1}$, and $R_o = 8.5 \pm 0.5 \text{ kpc}$ are used and the shear parameter and rotation rate are found by using

$$\Omega_o = A - B \quad (7)$$

$$q = \frac{\partial \ln(\Omega)}{\partial R_o} \quad (8)$$

with the values of A and B being given by

$$A = -\frac{1}{2} R_o \left(\frac{d\Omega}{dR} \right)_o \quad (9)$$

$$B = \Omega_o - \frac{1}{2} R_o \left(\frac{d\Omega}{dR} \right)_o \quad (10)$$

(Feast 2008).

Supernovae explosions are modeled by injecting spheres of high energy, on the order of 10^{51} ergs, around the midplane of the disk, and the resulting shockwave provides the necessary turbulence.

Periodic boundary conditions are employed to map conditions at one boundary onto the corresponding boundary. This simulation models a section of the galactic disk which has dimensions of $[-0.25, 0.25] \times [-0.25, 0.25] \times [-1.5, 1.5] \text{ kpc}$ and a resolution of $75 \times 75 \times 450$ zones.

Results and Conclusion

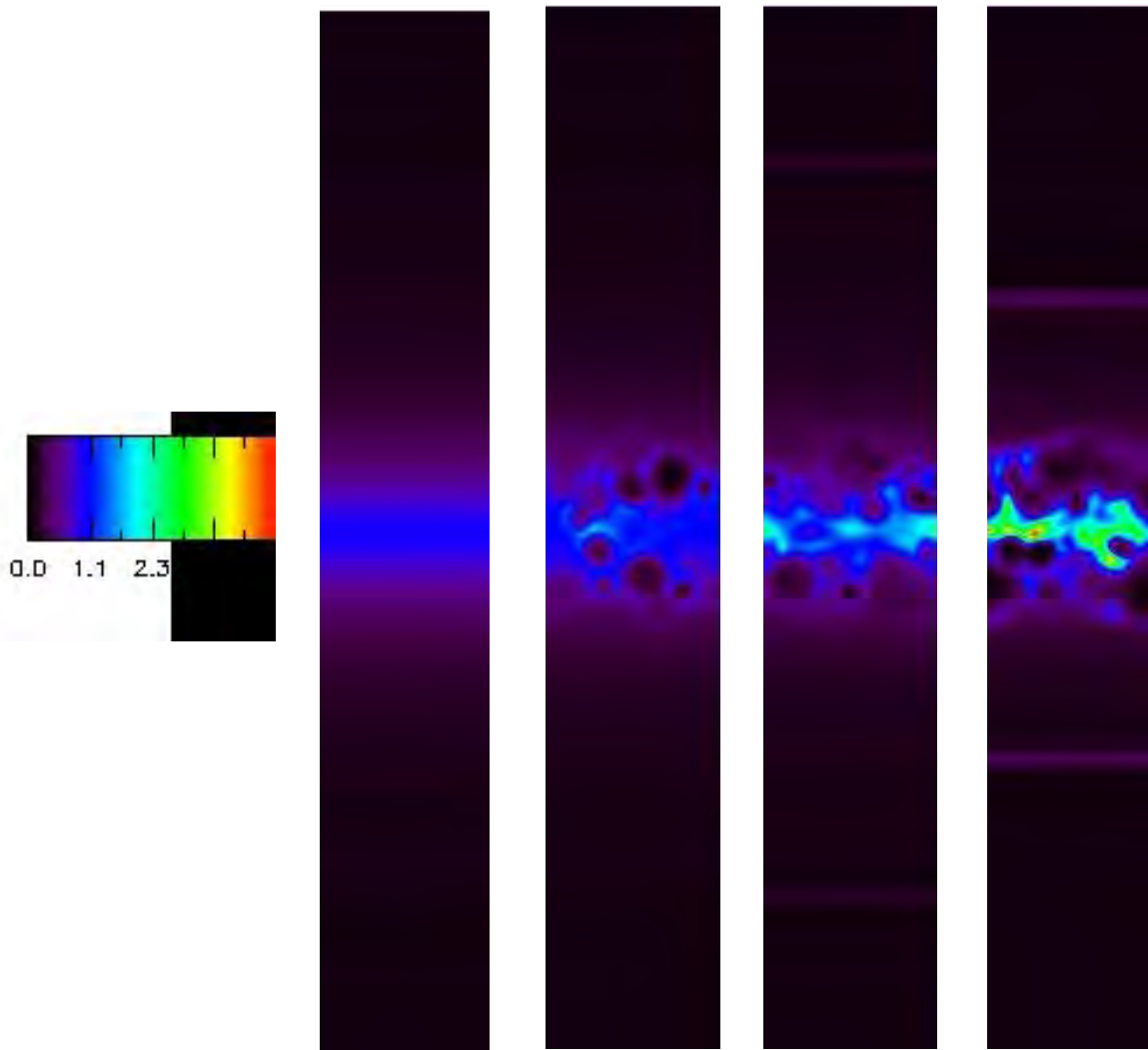


Figure 2: This cross-section of the disk shows the density distribution at various time points after the supernovae explosions were set off.

With the preliminary results from the first run, graphs of the density were obtained. These graphs were taken from a cross-section of the disk over a time period of 20 Myr. At the beginning it can be seen that the density was very uniform. After some of the supernovae were set off it can be seen in the second image that there are some bubbles of lesser density, but on the whole the density is starting to increase around the midplane. The third image shows this

further, as there is an area of high density beginning to form at the midplane which grows in size by the fourth and final image.

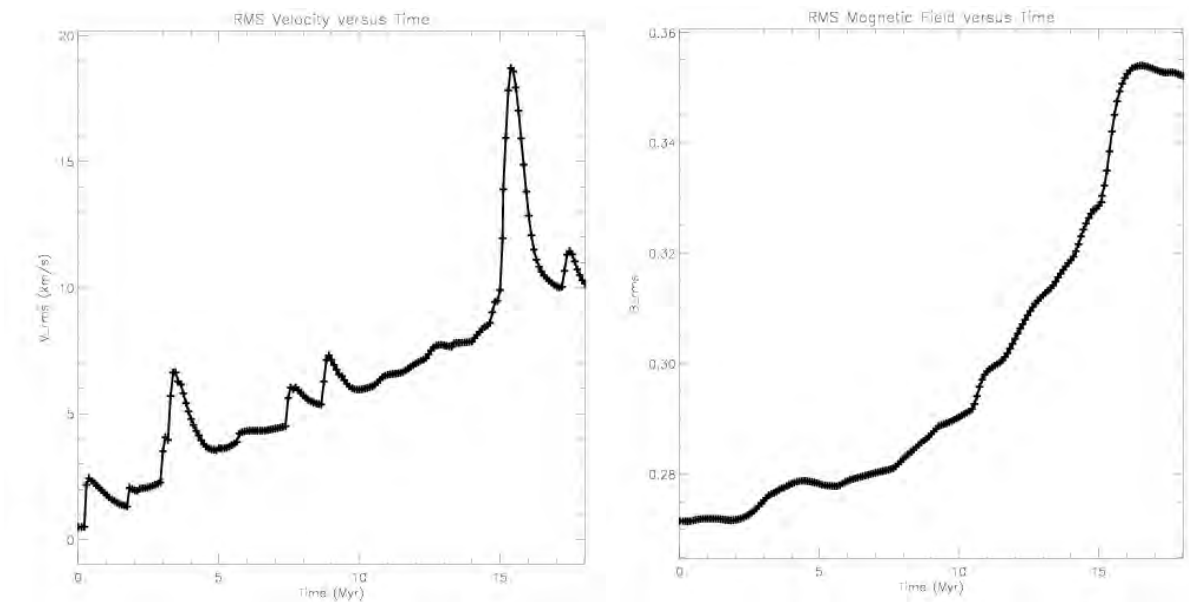


Figure 3: a) This shows the rms velocity as a function of time and b) shows the rms magnetic field as a function of time.

Figure 3a shows that as the time increased, the rms velocity increased as well. Similarly, in Figure 3b the rms magnetic field increases as time increases, indicating that turbulence caused by supernovae explosions in a stratified disk does amplify the magnetic field. In further research, more runs should be done at an increased resolution after some existing issues with the boundary conditions are addressed.

Acknowledgements

I would like to thank my advisor, Professor Dinshaw Balsara, for his guidance during the summer, as well as his graduate student, Christopher Matthews, for his work. I would also like to thank the 2011 NSF/REU Program and the University of Notre Dame for their support of this research

References

- Balsara D.S., Kim J., 2005, ApJ, 634, 390-406
- Balsara D.S., Tilley D.A., Rettig T., Brittain S.D., 2009, MNRAS, 397, 24-43
- Brandenburg A., Korpi M.J., Mee A.J., 2007, ApJ, 654, 945-954
- De Avillez M.A., Berry D.L., 2001, MNRAS, 328, 708-718
- Dombre T., Frisch U., Greene J.M., Henon M., Mehr A., Soward A.M., 1986, J. Fluid Mech. vol 167, 353-391
- Dyson J.E., Williams D.A., IOP Publishing Ltd. 1997, ISBN: 0-7503-0306-9
- Ferriere K.M., 2001, Reviews of Modern Physics, v73
- Gent G.A., Mantere M.J., Shukurov A., Fletcher A., Sarson G., 2010, MNRAS
- Gressel O., Elstner D., Ziegler U., Rüdiger G., 2008, A & A, 486, L35
- Feast M., Whitelock P., 2008, MNRAS
- Joung M.K.R., Mac Low M., 2006, ApJ, 653, 1266-1279
- Kuijken K., Gimore G., 1989, MNRAS, 239,605649
- Lequeux J., Springer-Verlag 2005, ISBN: 3-540-21326-0
- Passot T., Vazquez-Semaden E., Pouquet A., 1996, ApJ 455,536

Magnetotransport of Topological Insulators: Bismuth Selenide and Bismuth Telluride

Justin Kelly

2011 NSF/REU Program
Physics Department, University of Notre Dame

Advisors: Prof. Malgorzata Dobrowolska, Prof. Jacek Furdyna, Prof. Xinyu Liu

Abstract

Topological insulators are recent and exciting discovery in the field of condensed matter physics. In this paper, we measure some of the properties of two topological insulators: Bismuth Selenide (Bi_2Se_3) and Bismuth Telluride (Bi_2Te_3). Using a cryostat and a super conducting magnet, we are able subject the samples to a variety of magnetic fields and temperatures. We then measure the magnetoresistance and hall resistance of the samples. Each sample type varied in size and thickness, and was tested at multiple fields, temperatures, and angles.

The samples show interesting effects when subjected to the magnetic fields. In several of the samples, the magnetoresistance is proportional to square of the B field. The Hall Resistance has several features of interest that are explained in more depth in this paper. Low-Field Weak Anti-Localization also manifested itself in nearly every trial we did. We found that at high fields, the magnetoresistance of many samples would oscillate slightly. This ends up being the result of the Shubnikov-de Haas Effect.

Introduction

Topological insulators (TI) are an exciting, new topic in condensed matter physics.

The discovery of TIs was unusual for the field of condensed matter, in that they were predicted theoretically before they were observed in the lab. Several papers were published in 2005 and 2006 that predicted the existence of a type of material that would permit the movement of electrons only on its surface^{[1],[2]}, and TIs were observed later in 2007^[3].

We in the field are interested in Topological Insulators because of their unique conductive properties. The bulk of a TI acts as an insulator, while the surface allows the flow of electrons^[4]. You can therefore think of a TI as a piece of rubber or plastic with a thin layer of metal, only it achieves this conductive behavior by itself. You can achieve a similar effect through the Quantum Hall Effect. The (non-quantum) Hall Effect states that when you subject an electron current to a magnetic field, the carriers will tend toward one side of the

conductor, creating a potential difference laterally within the material. In high quality samples at low temperatures, you can start to measure quantum effects on the carriers. The Quantum Hall Effect states that, due to quantum effects, the carriers that have collected along the edge will move along the surface. This is similar to the behavior in TIs, but they are able to do this without the use of an external magnetic field.

TIs also have a unique effect on electron spin. The carriers that move along the surface of a TI are spin-locked^[4]. This means that the spin of each electron is perpendicular to its momentum. Figure 1a shows this as compared to a conventional insulator, and Figure 1b shows the band structure of a topological insulator.

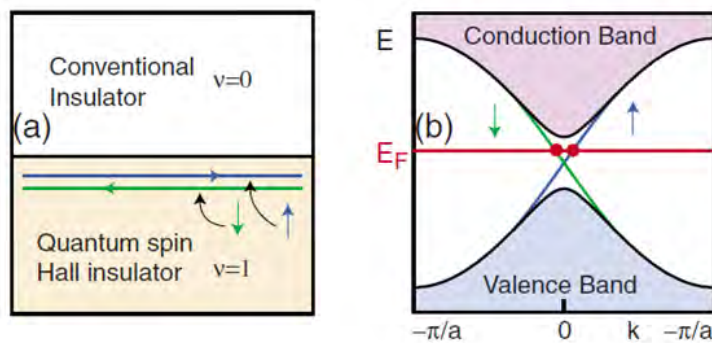


Figure 1 – a) A visual representation of the quantum hall effect b) the band structure of a topological insulator

As the electrons move to the right at the top of the material, their spins must be directed upwards. Those that move left have their spins reversed. These velocity-spin relationships would be switched for electrons at the bottom surface of the material. One effect of being spin-locked is that the electrons have a very high mobility, because scattering the carriers would require flipping their spin. This is impossible to do because that state is simply not available. These unique properties of TIs make them promising materials for research; there is great interest for applications in spintronics and quantum computing^[4].

Experimental Setup

In order to learn some of the basic properties of our TIs, which were grown in the MBE lab at Notre Dame, we performed magnetotransport on Bi_2Se_3 , Bi_2Te_3 , and $\text{Bi}_2(\text{TeSe})_3$. We accomplished this by soldering samples of various materials, size, and thickness to a sample holder. The sample holder was wired to instrumentation that would measure the magnetoresistance and the hall resistance of each sample. The sample holder, inserted to the top of the cryostat, was placed right next to a super conducting magnet. Using liquid helium and liquid nitrogen to cool the magnet, we were able to subject the samples to magnetic fields anywhere between 6 and -6 Tesla. By controlling the flow of liquid helium through the sample space, along with the help automatic internal heater, we were able to stabilize the temperature of the samples within a range of 2 K to about 200 K. The angle of the samples with respect to the magnetic field was easily adjusted by twisting the top of the sample holder. Thus for every sample we tested we measured a full sweep of the magnetic field for an assortment of angles and temperatures.

Magnetoresistance Data

When subjected to a magnetic field, certain materials have a tendency to change their resistivity. This property is known as magnetoresistance. From Kohler's Rule, the resistance of a material is proportional to the square of the magnetic field. This is shown in Eq. 1:

$$\frac{R(B)}{R(B=0)} \approx 1 + (\mu B)^2 \quad \text{Eq. 1}$$

By measuring the resistivity of the sample longitudinally (along the direction of the current) we are able to determine the magnetoresistance. Figure 2 shows the resistivity of $\text{Bi}_2(\text{TeSe})_3$. This sample is a particularly good example of the resistance and B^2 relationship.

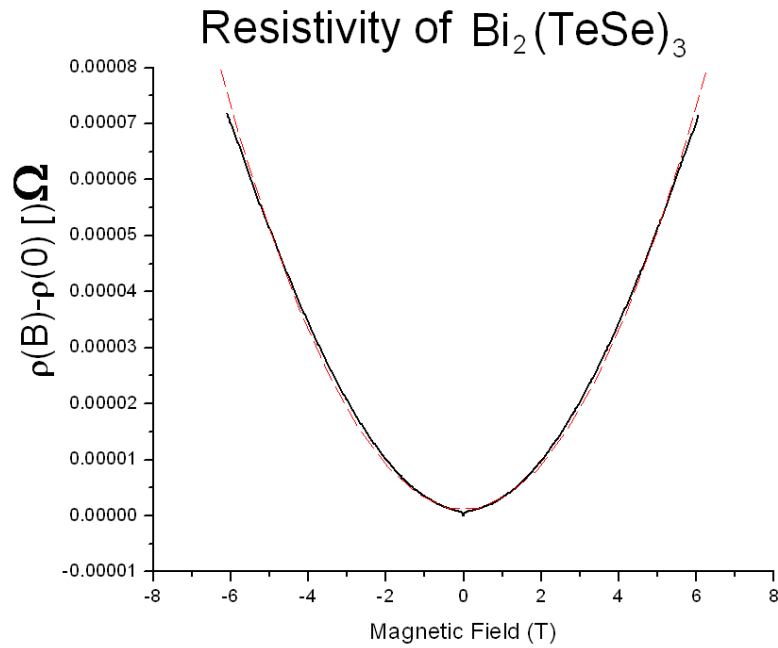


Figure 2 – The resistivity of a sample of $\text{Bi}_2(\text{TeSe})_3$ at 2.03K and its second order fit

Hall Data

As stated earlier, conductors in the presence of a magnetic field undergo the Hall Effect. Our topological insulators are no exception. Refer to Figure 3.

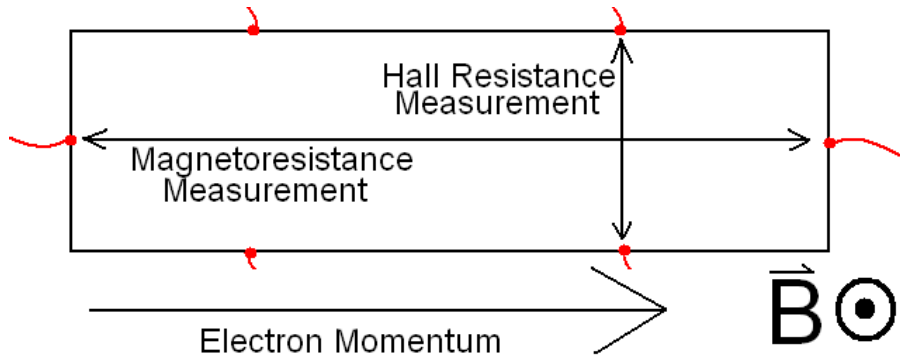


Figure 3 – A general diagram of each sample that we measured. The dots show the contact points where wires were soldered, and the arrows in the box indicate where each resistance was measured.

As the electrons flow longitudinally through the sample, they are pushed downward by the B field. This results in the expected potential difference, which in turn creates a Hall Resistivity. We measure this laterally according to the figure. For an example of a typical result, refer to Figure 4, which plots the Hall Resistivity versus the field strength for a sample of Bi_2Se_3 at various temperatures.

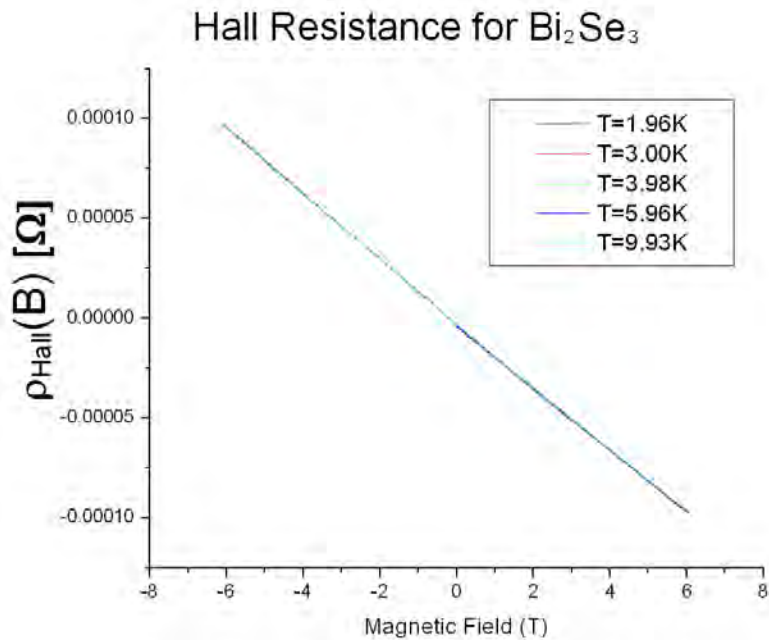


Figure 4 – Hall resistance for Bi_2Se_3 at various low temperatures

The equation for Hall Resistivity is listed in Eq. 2.

$$\rho = \frac{B}{nq} \quad \text{Eq. 2}$$

This equation predicts a linear function, which matches our shown results. However, linearity is not always the case. If an anomalous Hall Resistivity is introduced, then there will be a B^3 term present. Notice too, the slope of the Hall Resistivity. The fact that it is a negative slope confirms that the carriers are electrons, as opposed to electron holes which have positive charge. From this data, it is possible to calculate the carrier concentrations and mobility in the sample. The carrier concentration is result of linear regression. The program we used calculated the concentration and mobility for each, and results are listed in Table 1.

Temp (K)	Carrier Concentration (cm ⁻³)	Mobility (cm ² /V*s)
1.96	-3.89E+19	-270
3.00	-3.89E+19	-270
3.98	-3.90E+19	-269
5.96	-3.89E+19	-270
9.93	-3.92E+19	-268

Table 1 – Carrier concentration and Mobility for Bi₂Se₃ at various temperatures

Low Field Weak Anti-localization

Most if not all of the trials we did had an interesting dip in the graph near the zero Tesla mark. Sometimes these “features” were so small that you had to zoom in to see them, other times they dominated nearly the entire B field range. Figure 5 has an example of a sample with moderately sized features (Figure 2 also has an example of a very small feature).

Examples of WAL in Bi₂Se₃

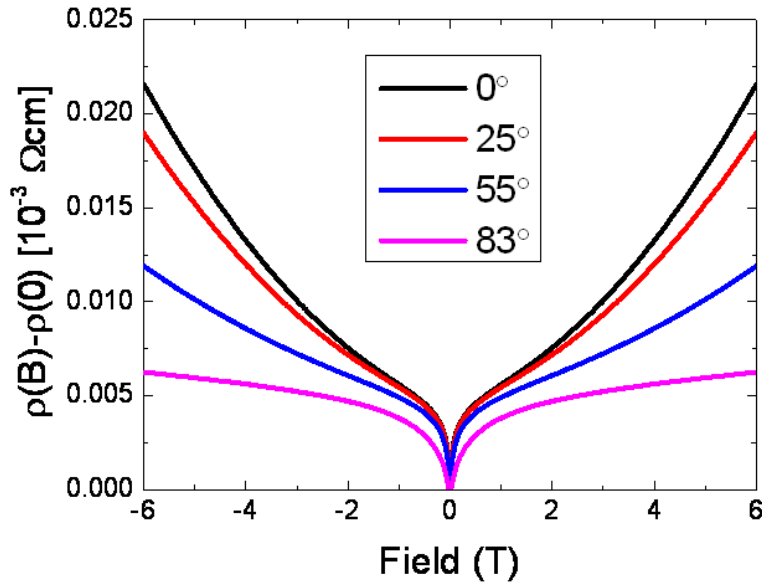


Figure 5 – Bi₂Se₃ at several different angles. This graph shows an interesting “feature” that is the result of the Low Field Weak Anti-Localization

These artifacts in the resistivity can be attributed to a phenomenon called Weak Anti-Localization (WAL) Effect. WAL is the suppression of backscattering due to impurities^[5]. Less backscattering means more mobility, and less resistivity. This effect mainly manifests in the low field, which is why the features of low resistivity always center on the zero field point. Eq. 3 characterizes the WAL Effect.

$$\begin{aligned} \Delta\sigma_{2D} &= \sigma_{2D}(B) - \sigma_{2D}(0) \\ &= -\frac{\alpha e^2}{2\pi^2 \hbar} \left[\ln \frac{\hbar}{4Bel_\phi^2} - \psi \left(\frac{1}{2} + \frac{\hbar}{4Bel_\phi^2} \right) \right] \end{aligned} \quad \text{Eq. 3}^{[5]}$$

Shubnikov-de Haas Effect

If you were to zoom in on the graph in Figure 2, you would notice that the line does not follow a perfectly parabolic line, but instead wavers around it. Though it would be very easy to attribute this to slight error or imprecision, it is actually due to a phenomenon called the Shubnikov-de Haas Effect. Figure 6a shows the same data as in Figure 2, but limited to the range of 1T to 6T.

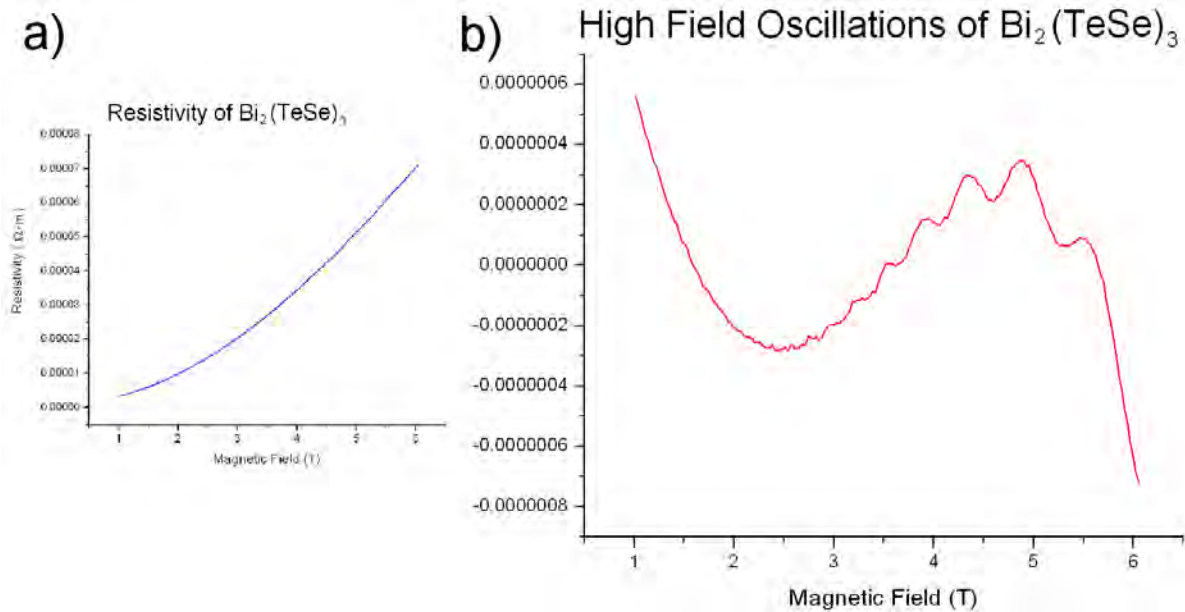


Figure 6 – An example of high field oscillations. a) A segment from Figure 2 b) The data from Figure 6a minus Figure 6a's second order fit

By taking a second order fit of that data, and subtracting that fit from the original data, we get Figure 6b. These oscillations, are not the result of error, but instead are the manifestation of the Shubnikov-de Haas Effect^[6]. This effect, which only occurs at low temperatures and high magnetic fields, is the manifestation of quantum mechanics at the macroscopic level. The peaks in these oscillations occur at quantized Landau levels.

Conclusion

In this experiment we set out to measure the magnetoresistance and hall resistance of our Bismuth Selenide and Bismuth Telluride samples. In doing so we were able to confirm properties that are expected in TIs. For example, our hall resistance data supported the idea that electrons were the carriers involved and not holes. We were also able to identify several interesting (though already known) phenomena in our samples. These include the oscillations caused by the Shubnikov-de Haas Effect in some of our samples, and the features created by the Weak Anti-Localization Effect in nearly all of our samples. Overall, we've collected a lot of data for various sample sizes, temperatures, and angles which we think will be beneficial as research on Topological Insulators progresses.

References

- [1] Kane, C. L., and Mele, E.J., 2005, " Z_2 Topological Order and the Quantum Spin Hall Effect", *Physical Review Letters*, v. 95, Issue 14
- [2] Bernevig, B. Andrei, et al., 2006, "Quantum Spin Hall Effect and Topological Phase Transition in HgTe Quantum Wells", *Science Magazine*, v. 314 no. 5806 pp. 1757-1761
- [3] König, Markus, et al., 2007, "Quantum Spin Hall Insulator State in HgTe Quantum Wells", *Science Magazine*, v. 318, no. 5851 pp. 766-770
- [4] Krumrain, J., et al., 2011, "MBE growth optimization of topological insulator Bi_2Te_3 films", *Journal of Crystal Growth*, 324 (2011) 115-118
- [5] Hong-Tao He, et al., 2011, "Impurity Effect on Weak Antilocalization in the Topological Insulator Bi_2Te_3 ", *Physical Review Letters*, 106, 166805 (2011)
- [6] Eto, Kazuma, et al., 2010, "Angular-dependent oscillations of the magnetoresistance in Bi_2Se_3 due to the three-dimensional bulk Fermi surface", *Physical Review B* 81, 195309 (2010)

Magnetic Properties of $\text{La}_{0.7}\text{Sr}_{0.3}\text{Mn}_{1-x}\text{Ni}_x\text{O}_3$ Perovskites

Ruben Medina

2011 NSF/REU Program
Physics Department, University of Notre Dame
Advisor: Prof. Howard A. Blackstead

Abstract:

Using the SQUID magnetometer, we studied the magnetic properties of $\text{La}_{0.7}\text{Sr}_{0.3}\text{Mn}_{1-x}\text{Ni}_x\text{O}_3$ ($x=0, 0.05, 0.10, 0.20$ and 0.30) perovskites. Both temperature dependent and field dependent magnetic properties show that Curie temperature decreases as a function of doping, ranging from 380K to 300K. Both magnetic measurements and neutron diffraction data hint at long-range magnetic ordering in samples at low temperature and transition phases from paramagnetic to ferromagnetic to antiferromagnetic ordering in samples at room temperature.

1.Introduction

1.1 Paramagnetism

The magnetic moment of an ion is given by

$$\mu = \gamma \hbar J = g \mu_B J$$

where g is the Landé g -factor, $\mu_B = 9.274 \times 10^{-21}$ erg/Oe is the Bohr magneton, and J is the angular momentum. All atoms have $2J+1$ energy levels. For an electron g is usually approximated to be 2.00, which is the spectroscopic splitting factor. Magnetization is the magnetic dipole moment per volume. Using the methods of statistical mechanics, the paramagnetic magnetization of a solid is given by

$$M = N g J \mu_B B_J(x); \quad (x = g J \mu_B H / kT)$$

where N is the number of ions per unit volume, H is the applied magnetic field, and k is the Boltzmann constant. B_J , the Brillouin function, is defined as

$$B_J(x) = \frac{(2J+1) \coth((2J+1)x/2J) - \coth(x/2J)}{2J}$$

The equation for M above describes the magnetization of an “ideal” paramagnet. In the classical limit, in which J can have any value, the Brillouin function simplifies to the Langevin function:

$$L(x) = \coth(x) - 1/x$$

If we study the equation for magnetization, we study using Pierre Curie's approximation, which deals with high temperatures and low magnetic fields, that when we increase the temperature and decrease the magnetic field. When we set $x = \mu_B/k_B T \ll 1$, in the Brillouin function, the magnetization reduces to

$$M = N J (J+1) g^2 \mu_B^2 H / 3kT$$

and further to

$$M = C * H / T$$

where C is the Curie constant, defined as

$$C = NJ(J+1)g^2\mu_B^2/3k$$

The magnetic susceptibility is

$$\chi_p = M/H = C/T$$

The lower the temperature, the higher the magnetization gets, and vice-versa.

1.2 Ferromagnetism

Ferromagnetism is the spontaneous magnetization of magnetic moments lining up with each other due to the influence they have on each other. The mean-field approximation derives from the assumption that every ion experiences a field proportional to the magnetization:

$$B_E = \lambda M$$

where λ is a material-specific constant that is independent of temperature. The mean-field approximation is temperature dependent. \mathbf{B}_E is assumed to be the equivalent of an exchange field, which is an internal interaction lining up the magnetic moments parallel to each other.

Above the Curie temperature, T_C , the spontaneous magnetization vanishes and the material is paramagnetic. Below the Curie temperature, the material is ferromagnetic. The magnetization is a complicated function of temperature and applied field. We can find T_C by observing λ from the mean-field approximation.

Looking at the paramagnetic phase, we have

$$M = \chi_p (B_A + B_E)$$

where χ_p is the magnetic susceptibility, and B_A is an applied magnetic field which causes a finite magnetization. Assuming that the material is in the paramagnetic phase, we can take Curie's Law for paramagnetic susceptibility to be

$$\chi_p = C/T$$

where C is the Curie constant. If we substitute this into the previous equation, we get

$$MT = C (B_A + \lambda M)$$

and rearranging the variables we can simplify it to

$$\chi = M/B_a = C/(T - C\lambda)$$

We see that the denominator is zero when $T = C\lambda$, in the above equation. At that temperature and below, the magnetization is spontaneous, and because of that we can have a finite magnetization for $B_a = 0$.

From this we get the Curie-Weiss Law

$$\chi = C/(T - T_C); \quad T_C = C\lambda$$

which describes the susceptibility variation in the paramagnetic region above the Curie point.

With this information we can define λ to be

$$\lambda = T_C/C$$

1.3 Antiferromagnetism

Antiferromagnetism is like ferromagnetism where instead the magnetic moments line up anti-parallel to each other.

If we begin by assuming separate Curie constants C_A and C_B for ions at two different sites A and B, we will have two interactions as $\mathbf{B}_A = -\mu\mathbf{M}_B$ and $\mathbf{B}_B = -\mu\mathbf{M}_A$; μ is a positive mean field constant. With the mean field approximation we would have

$$M_A T = C_A (B_a - \mu M_A) \quad M_B T = C_B (B_a - \mu M_A)$$

here, the B_a is the applied field. We solve this system of equations using a matrix, by assuming the applied field is zero. The susceptibility to at $T > T_C$

$$\chi = \frac{(M_A + M_B)}{B_a} = \frac{[(C_A + C_B)T - 2\mu C_A C_B]}{(T^2 - T_C^2)}$$

Now, for an antiferromagnetic limit we have $C_A = C_B$. Antiferromagnetism occurs below the

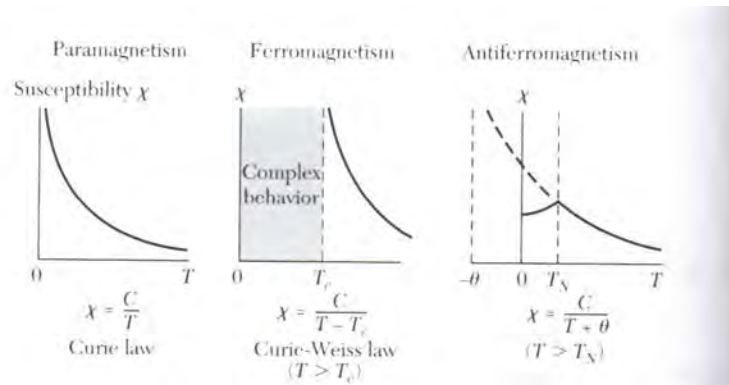
Néel temperature T_N . The Néel temperature is defined by

$$T_N = \mu C$$

after some substitution in the susceptibility equation above, we get

$$\chi = \frac{2C}{(T + \theta)}$$

where θ is $T > T_N$. A summary of all of the magnetizations is shown in the figure below. Note that at T_C for a ferromagnet the magnetization is a singularity, whereas at T_N of an antiferromagnet the magnetization peaks.



2. Methods

For this experiment, we used the SQUID (superconducting quantum interference device), which uses Josephson junctions to measure magnetic fields in samples of $\text{La}_{0.7}\text{Sr}_{0.3}\text{Mn}_{1-x}\text{Ni}_x\text{O}_3$. Small samples were obtained from pellets of bulk material of different Ni contents ($x=0, 0.05, 0.1, 0.2, 0.3$). The samples were prepared via solid-state reaction methods. 100 mg bars were cut using a diamond bladed saw. The sample was mounted with cotton into a pill capsule to protect it from moving around. After that, we sewed the capsule into place inside a straw, three-quarters of the way down. We inserted the straw into the SQUID.

3. Results

Magnetization data was obtained using both constant field and variable temperature, as well as varying field at constant temperatures. This data is plotted in two graphs for each sample composition: magnetic susceptibility[χ] vs. Temperature [T], and magnetization[M] vs. applied field[H]. The applied field was in the range of 0-70 KOe. Three sweeps were performed consecutively in the susceptibility measurements: Zero-field cooled (ZFC) where the sample is cooled in 0 field then warmed in a field while taking measurements, field cooled (FC) where the sample is then cooled in the same field while taking measurements, and field cooled warming (FCW) where the field is then turned off and measurements are taken as the sample warms.

As shown in Figures 1, 3, 5, 7 and 9, the transition temperature of the $x=0$ composition is approximately 375K, while for $x=0.05$ it is 330K, for $x=0.1$ it is 350K, for $x=0.2$ it is 300K and for $x=0.3$ it is 300K.

If we look at Figures 2, 4, 6, 8 and 10, we see that there is saturation at the $x=0$ state (at both 5K and 300K), at $x=0.05$ (at 5K, but not at 300K), at $x=0.1$ (at both 5K and 300K), and at $x=0.2$ (at 5K, but not at 300K).

Figure 4 shows a mixture of phases, at the higher temperatures, which can be seen through the combination of saturation and flatness. One point of interest, is that at the $x=0.2$ state, the 300K measurement was the only one we took above the transition temperature. Another point of interest, is at the $x=0.3$ state, there is no saturation at either temperature, even up to 70 KOe. All of the M vs T graphs seem have have comparably similar shapes, however by the time we have 30 percent doping, we see it has a different shape. The properties begin to change and there is a great suppression of the order of magnitude of magnetization, which can be seen on the y-axis, due to doping.

Based off Figure 11, it seems like there is no strong correlation between doping and transition temperature, however it does trend towards T_C suppression as Ni-doping increases.

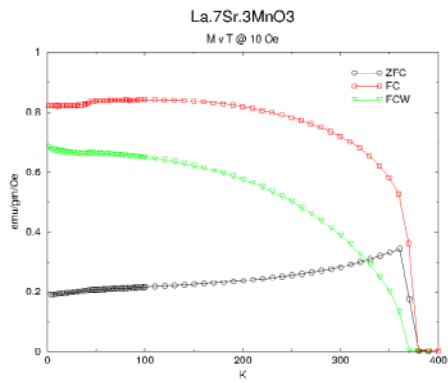


Figure 1: Temperature dependence of susceptibility for $x=0$ measured in a 10 Oe field

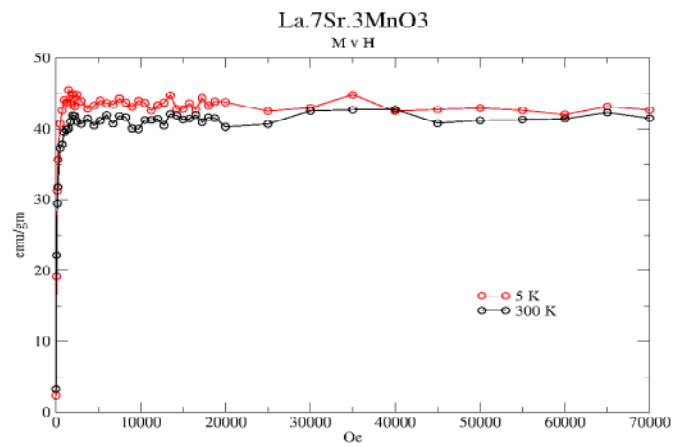


Figure 2: Field dependence of susceptibility for $x=0$ measured in a 10 Oe field

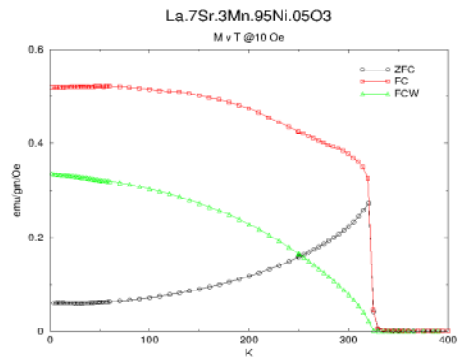


Figure 3: Temperature dependence of susceptibility for $x=0.05$ measured in a 10 Oe field

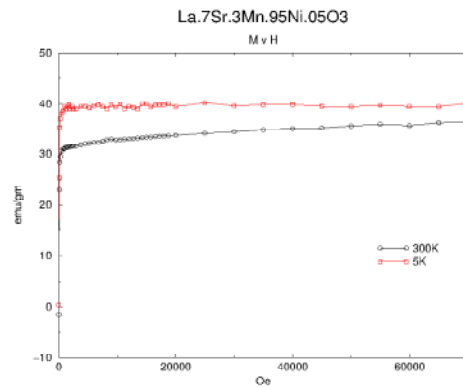


Figure 4: Field dependence of susceptibility for $x=0.05$ measured in a 10 Oe field

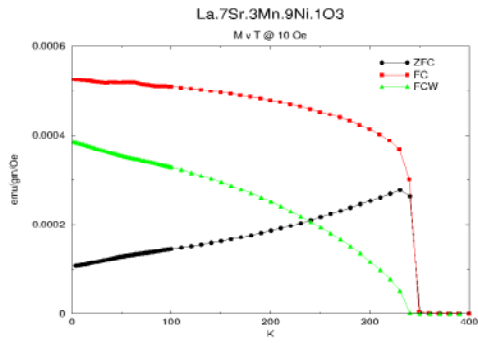


Figure 5: Temperature dependence of susceptibility for $x=0.1$ measured in a 10 Oe field

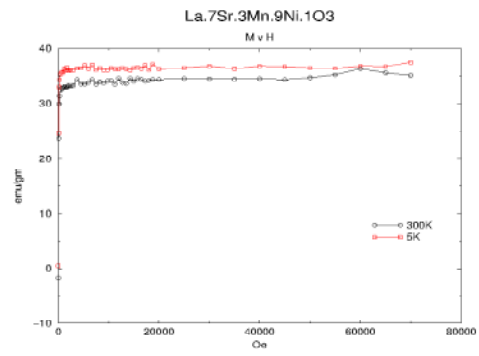


Figure 6: Field dependence of susceptibility for $x=0.1$ measured in 10 Oe field

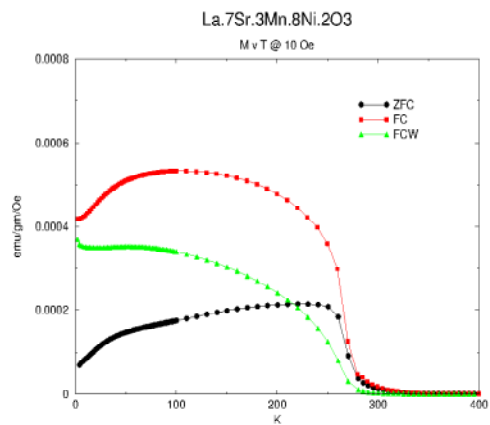


Figure 7: Temperature dependence of susceptibility for $x=0.2$ measured in a 10 Oe field

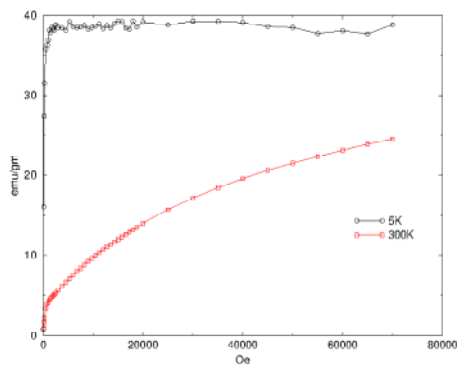


Figure 8: Field dependence of susceptibility for $x=0.2$ measured in a 10 Oe field

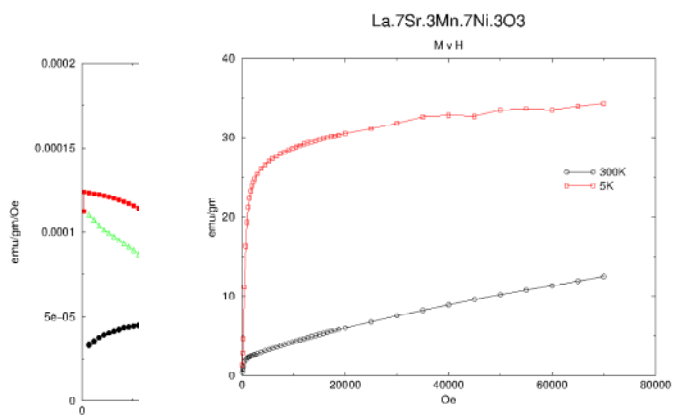


Figure 9: Temperature dependence of susceptibility for $x=0.3$ measured in a 10 Oe field

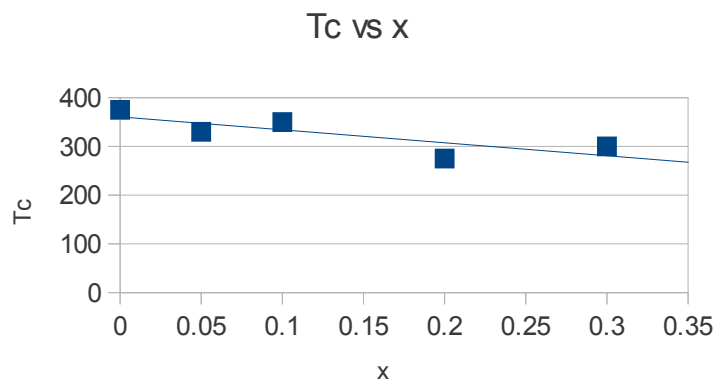


Figure 11: transition temperatures vs x

Energetics in Ice VI

Nishanth Sasankan

2011 NSF / REU PROJECT

Physics Department

University of Notre Dame

Advisor: Dr. Kathie E. Newman

Abstract

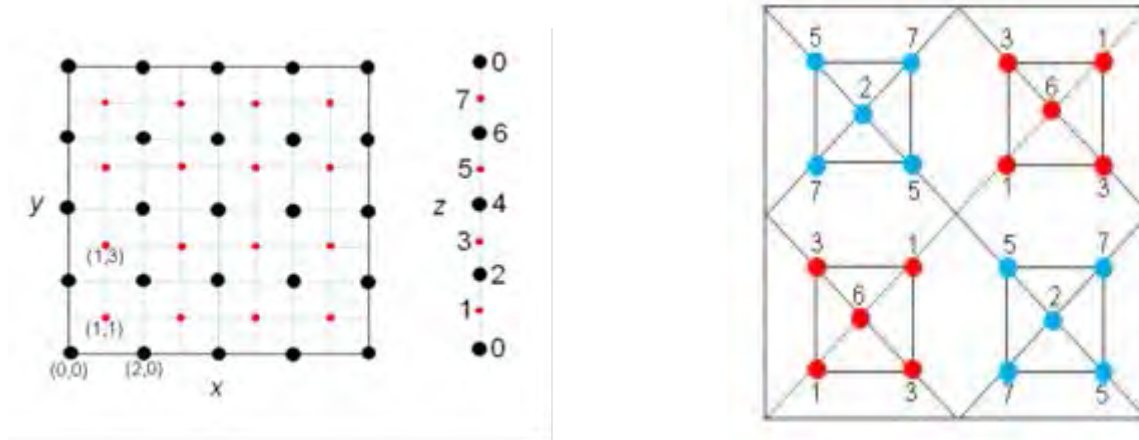
There are many different phases of Ice, which exist in different pressure and temperature combinations. The effort of my research is to study the phase transition between Ice VI and Ice VII, building upon the research done on previous REU student, Dawn King. I use the lattice framework of Ice VI-VII transition created by Dawn King and apply a Stillinger – Weber model of Monoatomic water as developed by Molinero and Moore. Taking a King’s lattice as a unit cell containing 512 sites, I simulate $3 \times 3 \times 3$ unit cells and take the central unit cell to calculate the energy. The central unit cell is chosen because it is surrounded by other unit cells and we do not have to apply periodic boundary conditions. Further work needs to be done on applying the periodic boundary conditions and develop the Monte Carlo simulations, in order to be able to do statistical calculations.

1. Introduction

Ice exists in about ten different crystalline forms. The effort of this research is to understand the processes involved in the phase transition of Ice VI to Ice VII. Ice VI and Ice VII both are self clathrate crystal structures, which means that these structures consist of interpenetrating sub-lattices. The effort of my research is to study the phase transition between Ice VI and Ice VII, building upon the research done on previous REU student, Dawn King[1]. I use the lattice framework of Ice VI-VII transition created by Dawn King and apply a Stillinger – Weber model of Monatomic water as developed by Molinero and Moore[2]. We use King's lattice and assume that atoms can only occupy discrete locations in the lattice. Also we use the idea of water being modeled as an intermediate element between carbon and silicon to understand the energy distribution in the lattice[2]. We try to understand the different kind of energetics that occur in the process of phase transition in order to create a Monte Carlo simulation that would explain the processes involved.

2. The Model

King's lattice framework for ice VI consists of 20 atoms, ten from each sub-lattice. The entire lattice consists of 512 discrete sites. Ice VI is shown in the second figure.



The numbers associated with each atom the height of each atom on the z-axis. The pattern follows in all x,y and z directions for a bigger lattice. The dimensions of the lattice are $(\sqrt{2}/8)a \times (\sqrt{2}/8)a \times (1/8)c$, where a and c are 6.27 Å and 5.79 Å.

Molinero and Moore[2] consider water as a monatomic substance that consists only oxygen. They compare the properties of water to other monatomic materials like silicon and germanium. These materials also form tetrahedral structures like Ice. Similar to Ice, their crystalline forms are also less dense than their liquid forms. The energy function used is called a Stillinger- Weber silicon potential and it is given by

$$E = \sum_i \sum_{j>i} \varphi_2(r_{ij}) + \sum_i \sum_{j \neq i} \sum_{k>j} \varphi_3(r_{ij}, r_{ik}, \theta_{ijk})$$

$$\varphi_2(r) = A\varepsilon \left[B \left(\frac{\sigma}{r} \right)^p - \left(\frac{\sigma}{r} \right)^q \right] \exp\left(\frac{\sigma}{r - a\sigma} \right)$$

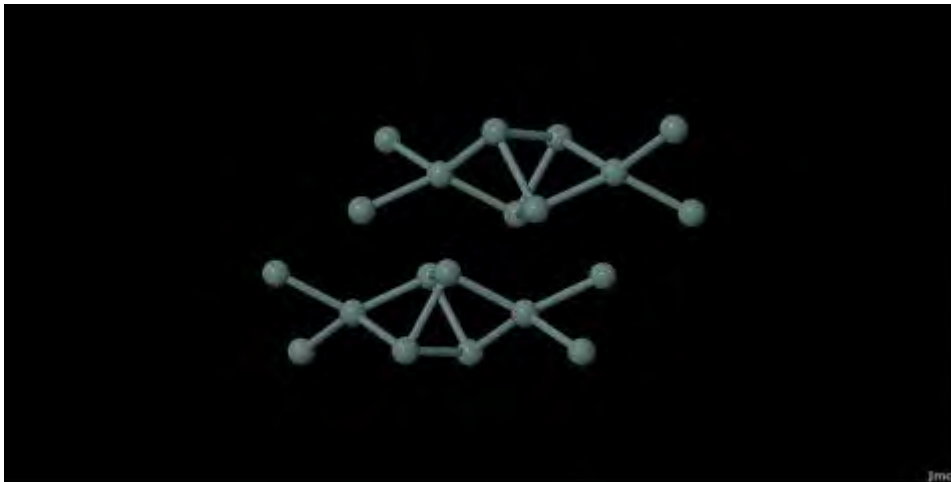
$$\varphi_3(r, s, \theta) = \lambda \varepsilon [\cos \theta - \cos \theta_0]^2 \exp\left(\frac{\gamma\sigma}{r - a\sigma} \right) \exp\left(\frac{\gamma\sigma}{s - a\sigma} \right)$$

The values of all the parameters are given in [2]. The first part of the energy is obtained from the pairwise interaction between the atoms in the lattice. The second part of the energy is due to the angle formed by triplets of atoms in the tetrahedral units. The parameter λ determines how tetragonal the structure is. For water the value of λ is 23.15, which is higher than silicon (21) and germanium (20). We only consider interactions within a cutoff distance of 4.306 Å. The value of energy for both part of energy beyond this cutoff is zero.

3. Energy Calculation

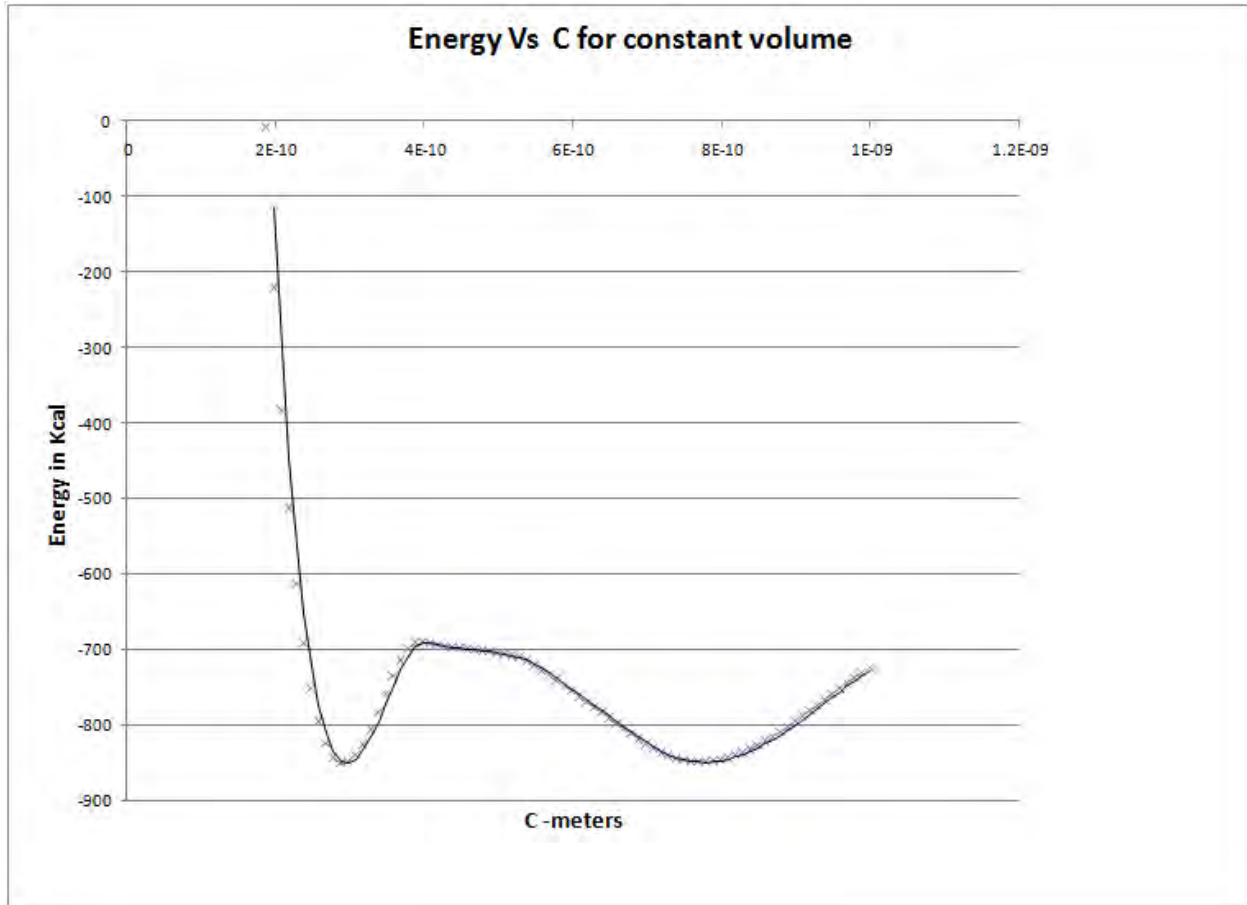
Initially, for testing the programming of the energies we compared it with the results produced in [3]. For developing a Monte Carlo simulation, we need to apply periodic boundary conditions to the lattice. The periodic boundary condition is applied so that all atoms have a bulk environment. There are basically two different environments for the atoms in the sub-lattice. One in which the atom is bonded to another chain in the same sub-lattice, another in which the atom is bonded to only atoms in the same chain. The atoms on each faces other than the faces formed by z-plane require one more atom to complete the set of four atoms bonded to it. When the atom is on the faces formed by the z-plane, two atoms are required to

complete the set of four atoms. For each corners and edges other than the ones on the z-plane, we require two more atoms to complete the set of four atoms. All other edges and corners would need one more atom to complete the set of four. Atoms on edges that are parallel to x and y axis are bounded to the corresponding parallel edge on the same plane while the edges that are parallel to z-axis are bounded to diagonal edges. The figure below shows the chains of the two sub-lattices extending in the z direction. Connecting bonds to other chains are not shown.



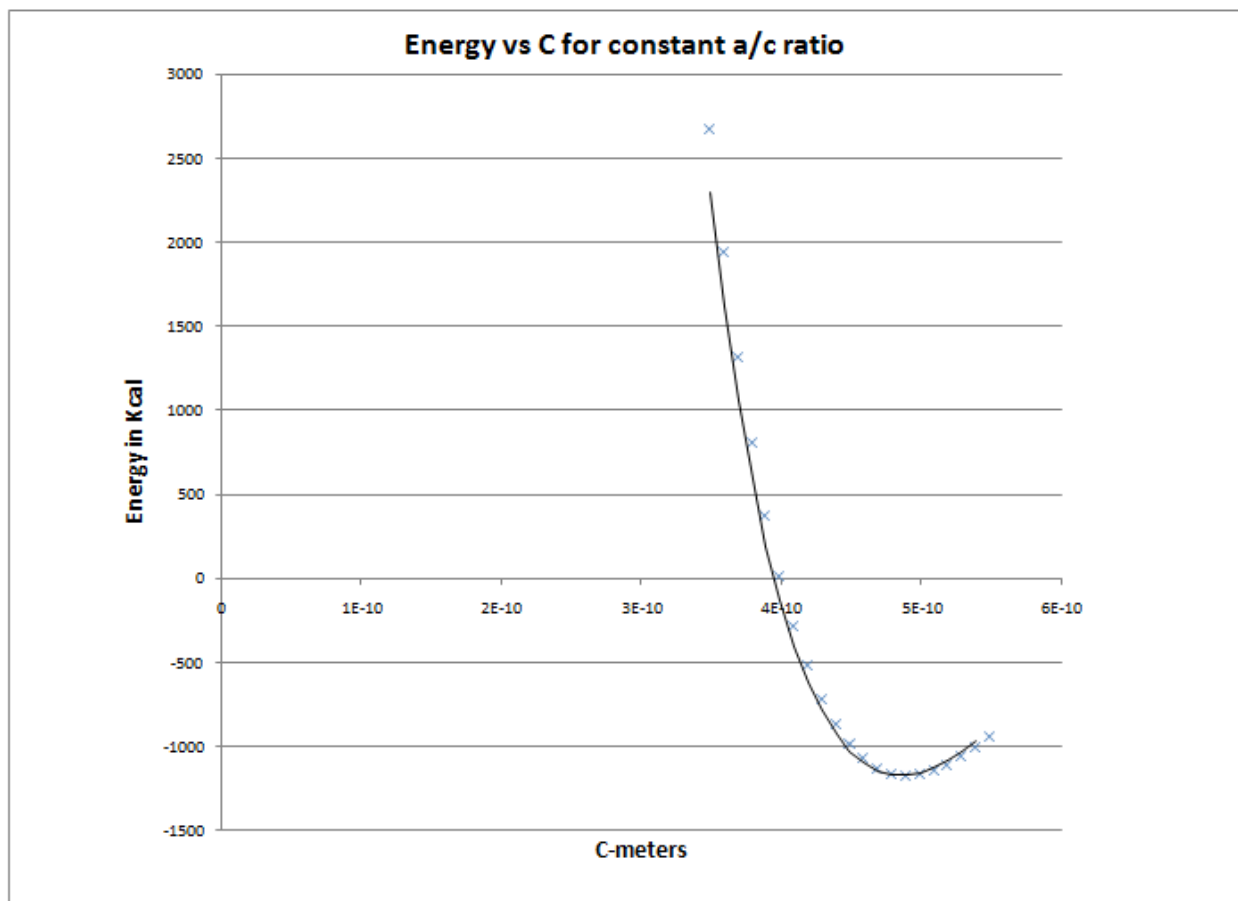
We do a static energy calculation on a unit cell. We create a $3 \times 3 \times 3$ unit, where each unit is King's lattice. For energetics, the central unit cell is chosen because we don't have to apply periodic boundary conditions to it. All atoms in it are bounded to a set of other four atoms.

We check the variation in energy for the unit cell with respect to different length and height values, keeping a^2c constant. The plot of the energy with respect to decreasing c -value is shown below



For constant volume the plot shows that there exists other configurations of atoms for which the energy of the unit cell is lower. The values for c and a at the lowest energy configuration are 7.69 Å and 5.44 Å respectively, the lattice is more cubic in this configuration. The second c and a value for which the energy is lower are 2.88 Å and 8.89 Å. The lattice is compressed in the z direction for this configuration.

We also calculate how the energy varies if we keep the a/c ratio constant. The plot energy with varying a and c with constant a/c is given below.



We can see that there is a better configuration of atoms for which a/c is constant. The value of c for which the energy is lower is around 4.79 \AA . If we increase the value of c instead of decreasing, then the energy reaches zero since atoms become further apart from each other and there are no interactions or bonds.

4. Further Work

More work need to be done in applying the periodic boundary condition to the lattice. Once periodic boundary condition is applied we could apply the Monte Carlo Metropolis algorithm. We should be able to check the Monte Carlo trajectories and see how the Ice VI structure changes to Ice VII. Or if it does not transition to Ice VII, we could conclude that the Stillinger-Weber model would not be sufficient to simulate the transition of Ice VI to Ice VII.

5. References

- [1] http://physics.nd.edu/assets/25212/king_dawn_modeling_phase_trans.pdf
- [2] V. Molinero and E.B. Moore, "Water Modeled As an Intermediate Element between Carbon and Silicon," J.Phys. Chem B113, 4008-4016 (2009).
- [3] M. Laradji and D.P. Landau, " Structural Properties of Si, Ge alloys: A Monte Carlo simulation with the Stillinger-Weber potential," Phy. Rev. B 51,8 (1995).

The Effects of an Accretion Stream on the Period and Spectra of a Cataclysmic Variable

Branden Summa

2010 NSF/REU Program
University of Notre Dame

Advisor: Peter Garnavich

Abstract

The star CSS 081231:071126+440405 is a variable star located in the constellation Auriga. The star system is composed of a main sequence star and a denser white dwarf that accretes mass from the main sequence star. While in most cases the infalling matter forms an accretion disk surrounding the white dwarf, the high magnetic field of this star instead causes the ionized gas to fall through the Lagrangian point and follows the magnetic field lines of the white dwarf, creating a stream of particles. This stream, in addition to stabilizing the period of the system, impacts the surface of the white dwarf, creating a hot-spot that dominates the emission from the star.

Observations taken by members of the AAVSO (American Association of Variable Star Observers), as well as data acquired by the VATT telescope in Arizona, allowed us to track the magnitude changes of CSS 081231 across a multitude of periods spanning months. Using this data, we calculated an average orbital period for the star of approximately 117.18279 minutes, with eclipse averaging around around 5.776 minutes. Additionally, we determined what relationship the hot-spot had on stars' orbit. Furthermore, the magnitude of the system experiences a large change outside of the eclipse that appears to be wavelength dependent, and we determine the effect of this on the star's orbit. Using data obtained with the 4 meter telescope at KPNO, we then performed spectral analysis on the star to determine how the emission varies between eclipses, focusing the $H\alpha$, $H\beta$, and He II lines. Finally, we used the total flux in various filters to determine color variations.

1 Introduction

While our solar system contains only a single star, most stars in the universe are part of a binary system. One particular type of binary system is a cataclysmic variable, composed of a white dwarf and a main sequence star. In a cataclysmic variable, the two stars are close enough to each other that the gravitational pull of the white dwarf is able to accrete matter from the surface of the main sequence star. One particular sub-division of cataclysmic variables is polars. This kind of system occurs when the white dwarf has a high magnetic field, causing the accreting matter to follow the magnetic field lines. Polars come in two varieties:

1. AM Herculis stars have a high magnetic field, causing all of the accreting matter to all fall into the same place on the dwarf.
2. DQ Herculis stars have weaker magnetic fields, causing some of the matter to accrete onto a hot-spot while still creating an accretion disk.

CSS 081231 is a polar located in the constellation Auriga, discovered by the Catalina Sky Survey(CSS) on Dec 31, 2008 in outburst. Initial observations of the star indicated that it was an AM Herculis star with a period of around 0.813 days[1]. In March of 2009, the AAVSO sent out a notice to astronomers asking for further observations following a reported rapid increase in brightness[1]. While a large amount of data was obtained, much of it still has yet to be analyzed. Our analysis provides further refinements on the period as well as spectral analysis of the accretion stream and hot-spot.

2 Procedure

2.1 Period and eclipse width determination

Using light-curve and spectroscopic data provided by the AAVSO, VATT (Vatican Advanced Technology Telescope), and the KPNO (Kitt Peak National Observatory), we set out to determine how the period and the base magnitude of the system has changed over time. We started by finding an average orbital period for the star, using a list of 23270 observation times and magnitudes provided by the AAVSO. After changing the observation times into Julian dates, we then used the IDL program “helio_jd” to convert to the heliocentric Julian date to remove any variations caused by light travel time. Finally, we subtracted off a constant so that the data began on day zero, corresponding to the Julian day 2454833.

In order to get an average period, we first created a program which identifies local maxima in the magnitude and then plotted area around the maximum. If it was clear that the maximum corresponded to an eclipse and not simply noise, we then used IDL’s cursor program to hand-select the maximum and store the time and magnitude into arrays. We used dates where we had several subsequent eclipses to derive an initial guess by averaging out the distance between them. We further refined this estimate by selecting one well-surveyed eclipse and defined that as the zeroth eclipse. Every other eclipse’s date was then subtracted from this and then divided by the initial guess of the period and rounded to the nearest integer. Then gave the epoch, i.e. how many eclipses away from our zeroth eclipse each eclipse was. By using the program `poly_fit`, we created a best fit line between these epochs and the Julian dates, the slope of which gave us a better estimate of the period.

2.2 Pre-eclipse magnitude change

In many of the orbits the star experience decrease in luminosity before the primary (For an example see Fig.6). We first recorded the date and magnitude of this decrease using the same methods as we did for the eclipse. We did this both for the AAVSO data as well as data obtained during two separate runs of

After obtaining an average period, we next decided to see how this period varied over time. To do this we first found the base magnitude of the system (magnitude outside of eclipse). The hot-spot is the dominant source of light for the system, and the brightness of the hot-spot increases as the amount of matter falling onto it increases. Thus the base magnitude gives us information about the accretion rate. By subtracting this base magnitude, we subtracted off the base magnitude and put all the eclipses in the same phase and plotted the results. We then examined the graph to see if there was any significant changes over time. In addition we determined the relationship between the accretion rate and the period of the star using the base magnitudes.

Once we determined that there was no significant change in the period, we used this information to better identify more eclipses. We started by plotting the area around the first period and used the cursor program to record each eclipse by moving through the plot in increments of our original period estimate. This allowed us to increase from our original sixty-seven eclipse data point to one-hundred and forty. We then used these new data point to make a final adjustment on the period using the same method described above. Once we had the period defined, we next decided to determine the average length of the eclipse. To do this we again used the cursor program to mark the date of the beginning and end of the eclipse as well as the dates when the eclipse reached half-minimum.

the VATT telescope in Arizona. Once this was done, we determined what effect this decrease had on the light-curve of the system, particularly it’s effect on the width of the eclipse. After analyzing the data and identifying the cause of any outliers, we then plotted the results and looked for trends.

2.3 Spectral analysis

After the analysis of the AAVSO data, we performed spectral analysis of the star. Using data obtained from KPNO, we analyzed the emission spectra over two separate nights using the `splot` feature of IRAF. In particular, we were interested in the equivalent width (a measurement of the integral flux compared to background) of the $H\alpha$, $H\beta$, and He II lines. After saving the equivalent widths into arrays, we used “`hselect`” to obtain the time of observation plotted their changes over time.

After reading the fluxes and wavelengths into arrays (See Fig.1 for an example of a spectrum in IDL),

we used IDL to calculate the total flux in the U, B, V, and R bands (binned according to the Johnson-Morgan / Cousins system). Next, we then used the equation: $-2.5 * LOG(flux) - 12$ to turn the flux into something resembling magnitude, with any elements with flux less than 0 being set to 999. Finally, we looked at the color changes of the hot-spot by comparing the U-B, B-V, B-R, and V-R magnitudes. Noticing a possible rise in the B-R data just before eclipse, we took the parts of the B-R magnitude and created a best-fit line, which we then subtracted from the data in order to better highlight this trend.

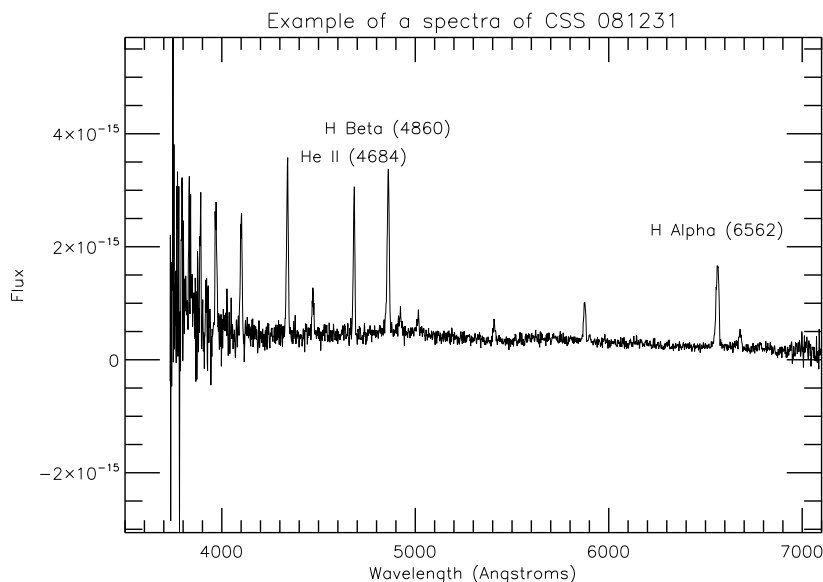


Figure 1: An example of a spectra showing H alpha (6562), H Beta(4860), and He II (4684) lines

3 Results / Analysis

3.1 Period and Magnitude changes over time

Our initial investigation of the period, using eclipse estimates obtained visually using the cursor command, revealed no significant change in period

(See Fig.2). Using a linear fit on our first set of eclipses gave us an estimate for the heliocentric Julian day(HJD) of eclipse:

$$\text{HJD} = 55127.42411 + 0.081376839 \pm 3 * 10^{-7} * E \quad \text{Where } E = \text{Epoch} \quad (1)$$

After including more eclipses, we obtained an HJD for eclipse of:

$$\text{HJD} = 55126.44660 + 0.081376865 \pm 4.6 * 10^{-7} * E \quad (2)$$

Both of these values are in agreement with each other as well as previous estimates of 0.081 and 0.813 from time-series photometry by D. Denisenko and S. Korotkiy and the AAVSO[1]. After determining the period, we next plotted the base magnitude (magnitude of the system outside of eclipse) as a function of date in order to see how the magnitude of the

system varied over time. The results of this can be seen in Fig.3. The brightness of the system appears to drop by 2 magnitudes and then to rise back up again in a relatively short period of time, however there is not enough data to ascertain how regularly this may occur.

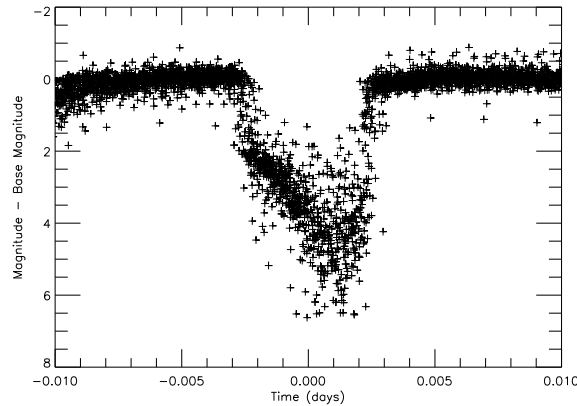


Figure 2: Periods Superimposed

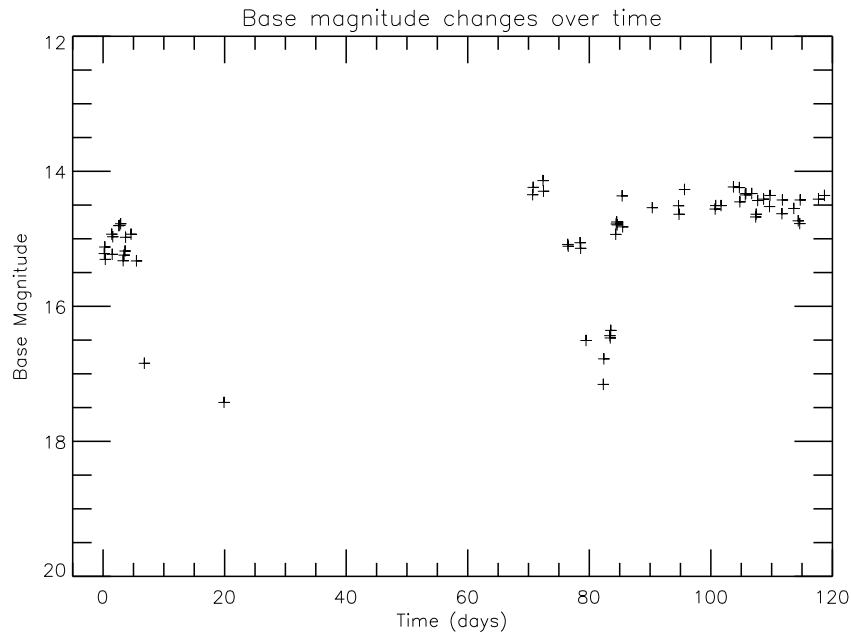


Figure 3: Base Magnitude vs. time (days)

3.2 Pre-eclipse Dimming

As mentioned earlier in this paper, the system experiences a significant change in magnitude unrelated to the eclipse. However, this pre-eclipse dimming does not appear in every eclipse in the data set, including some of the VATT data. We surmise that this is due to the use of different filters for different observations as the dip appears to be heavily wavelength dependent. In particular, this dip is very strong in blue wavelengths while it is unnoticeable in red (See Fig.6). We hypothesize that this dimming is caused by the accretion stream. We believe that the dip occurs when the hot-spot is blocked from the view of earth by the stream, thus diminishing the total emission.

We next decided to see if there was any correlation between the magnitude of this dip and the width of the eclipse. First, we determined an average width of the eclipse of 0.00401 days(5.776 minutes). Then, we selected certain eclipses with well defined lightcurves and plotted the eclipse width vs. the magnitude of the dip (See Fig.4). From this graph, we determined that there was no significant correlation between the magnitude of the dip and the width of the eclipse. Additionally, we plotted the difference between the timing of the dip and the rise in magnitude out of the eclipse and determined there was no significant correlation (See Fig.5)

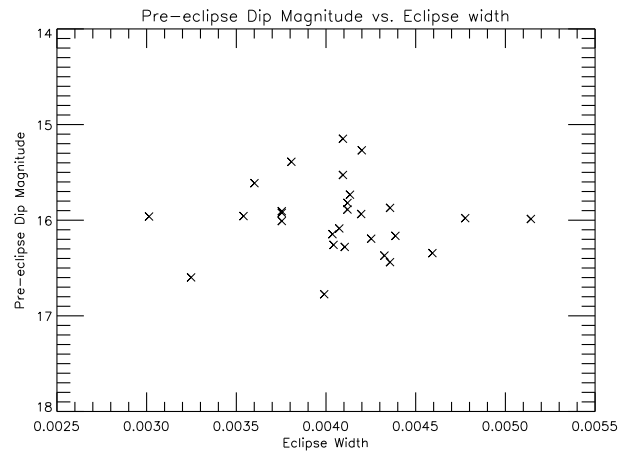


Figure 4: Eclipse width (days) vs. dip magnitude

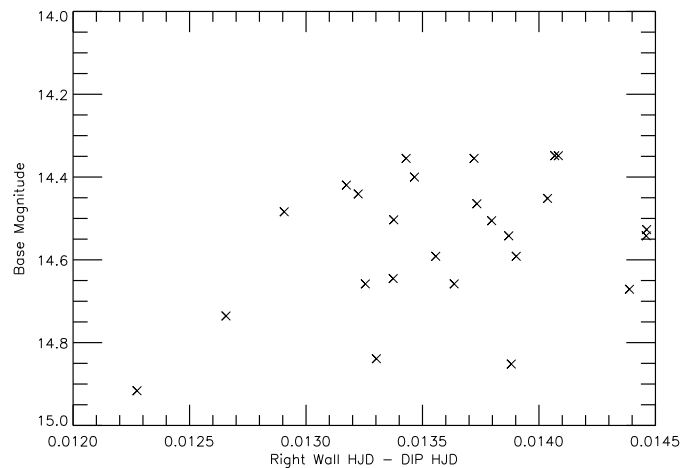


Figure 5: Time between dip and eclipse (days)

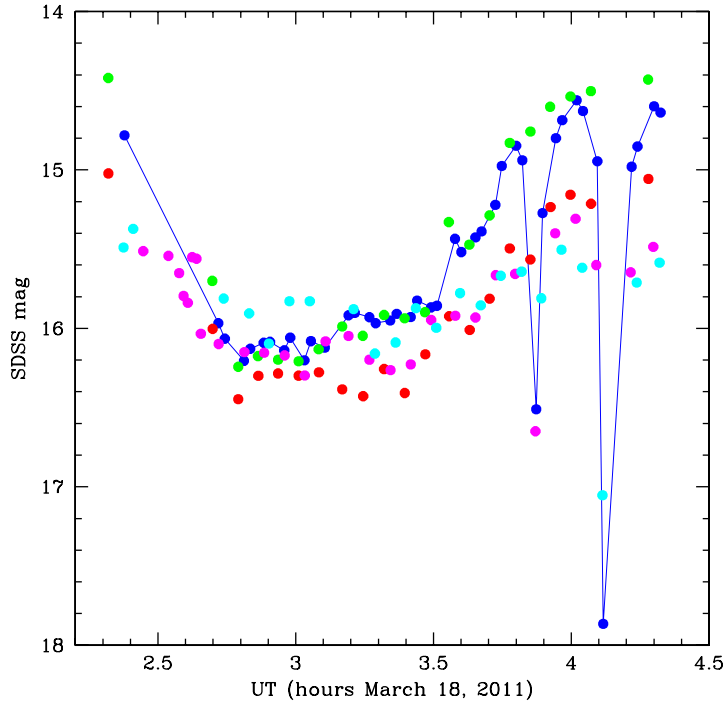


Figure 6: Figure showing wavelength dependence of dip

3.3 Emission Spectra and Color Variation

3.3.1 Emission / Absorption of $H\alpha$, $H\beta$ and He II

Using spectroscopic data from KPNO, we analyzed the emission spectrum of the hot-spot using the equivalent widths of $H\alpha$, $H\beta$ and He II. Fig.8 displays the data over two separate nights (the second of the three nights was too cloudy to observe) while Fig.9 shows the same data over-plotted and phased. There are several differences of note between the two nights.

The equivalent width of all the lines appears to rapidly increase after eclipse and continue to get stronger until rapidly dropping before the next eclipse. The third night in contrast has roughly the same equivalent width throughout the time between eclipses. Additionally, the data on the third night shows a leveling off and then extremely rapid decrease right before full eclipse that is not present on the first night. Furthermore, both nights have times where there exists both emission and absorption. The absorption tends to happen just after eclipse. A previous study by Schmidt, G. et al. also noted absorption and pre-eclipse dips, however in that case

the dip and absorption happened around the same time while ours occur at different points[2]. We hypothesize that the accretion stream is causing this effect by blocking the emission of the hot-spot, and the fact that this star has the dip and absorption at different times is due to the hot-spot being on the other side of the dwarf than the accretion stream's original direction unlike the star in the other study (See Fig.7).

Of particular note, several of the eclipses (especially on the third night of observation) show a massive increase in the equivalent widths of all lines. While the large equivalent width can be partially attributed to the low total flux, the peaks are clearly discernible. Additionally, the repeated existence of this peak in all three emissions makes it highly unlikely to be caused by cosmic ray hits or fluctuations. We hypothesize that this increase in flux is caused by the accretion stream not fully being eclipsed and emerging around the star.

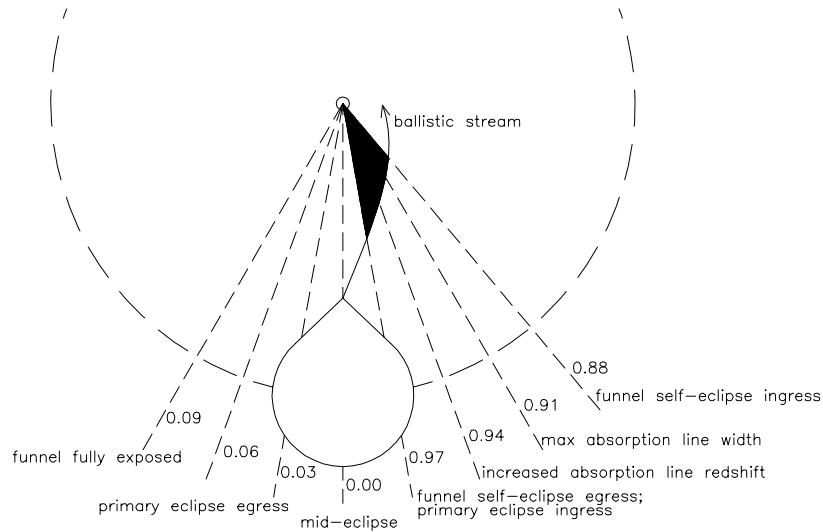


Figure 7: Representation of another polar by Schmidt et al.

3.3.2 Color Changes

In order to determine the color of the hot-spot, we analyzed the difference in magnitude in several bands. The data that showed the least amount of noise was the B-band and the R-Band. Fig.10 show the B-R data for both nights while Fig.11 shows that

same data over-plotted in terms of the fraction of the period. The third night data seems to show a reddening of the hot-spot just before eclipse, however, there is too little data and the data is too noisy in order to make any definitive conclusions.

4 Conclusions

We have produced a more accurate measure of the period of CSS 081231 over a time-span of several months. In addition, the small error on our period estimate puts bounds on variation on that period. In particular, we have shown that neither the timing nor the magnitude change of the dip affects the period or base magnitude significantly. As the dip is thought to be caused by the accretion stream, the evidence suggest that the amount of matter being accreted does not substantially effect the orbit of the stars. Additionally, the difference in timing of the dip and the absorption lines in contrast to other polars, as well as the sharp peak during eclipse indicates that the shape of the stream may play an important role in determining the emission from the star.

References

- [1] AAVSO Special Notice #142 The new eclipsing cataclysmic variable CSS 081231:07126+440405, January 3, 2009
- [2] [Schmidt et al.(2005)]2005ApJ...620..422S Schmidt, G. D., et al., 2005, Astrophysical Journal, 620, 422

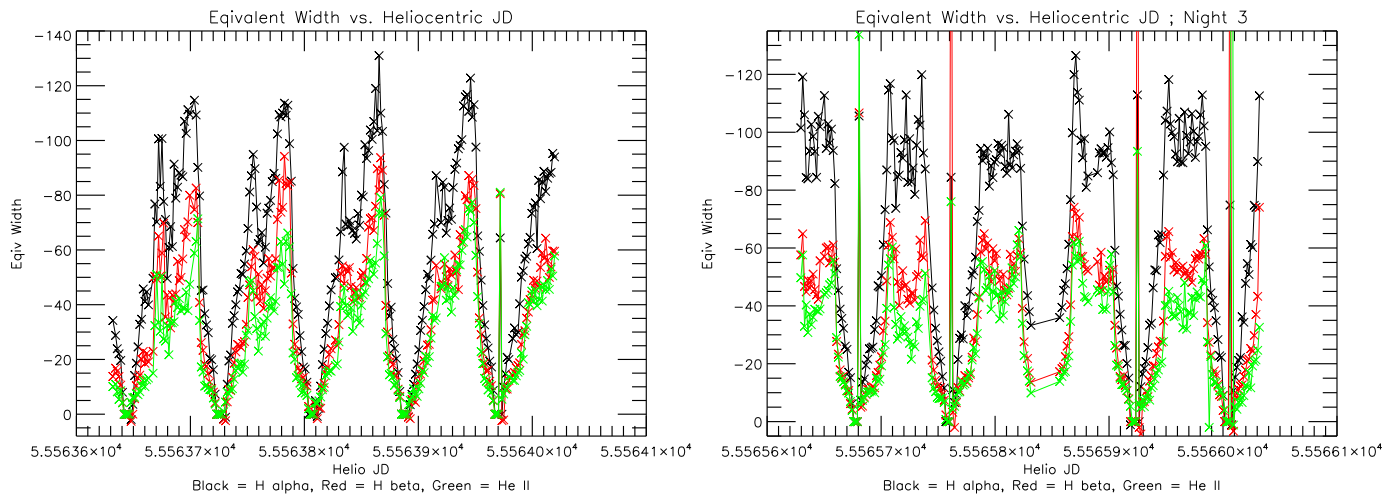


Figure 8: Nights 1 and 3 equivalent widths vs HJD

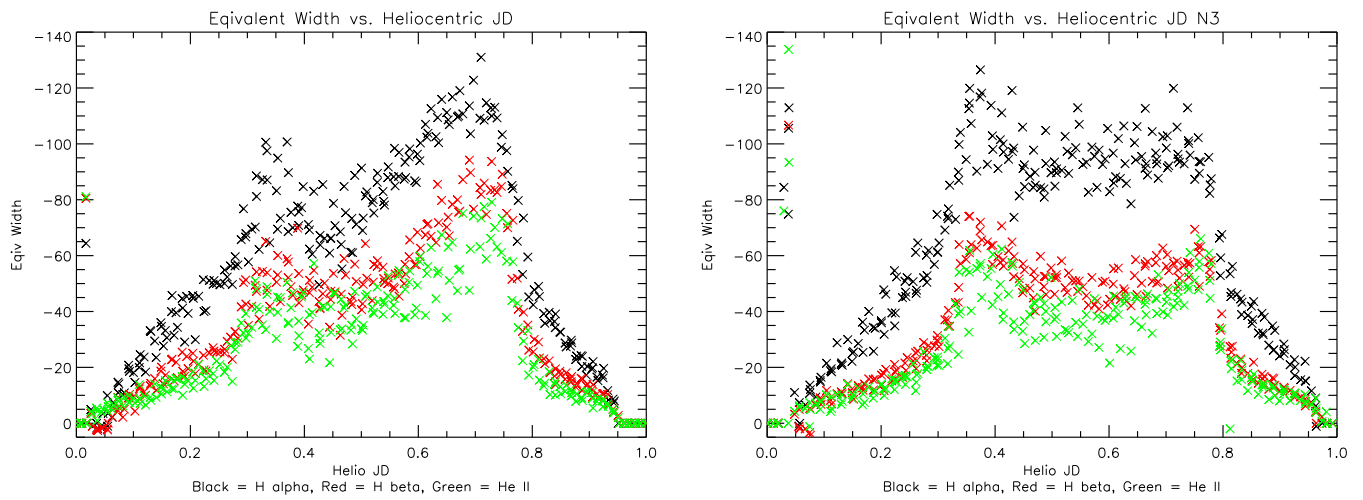


Figure 9: Nights 1 and 3 phased equivalent widths

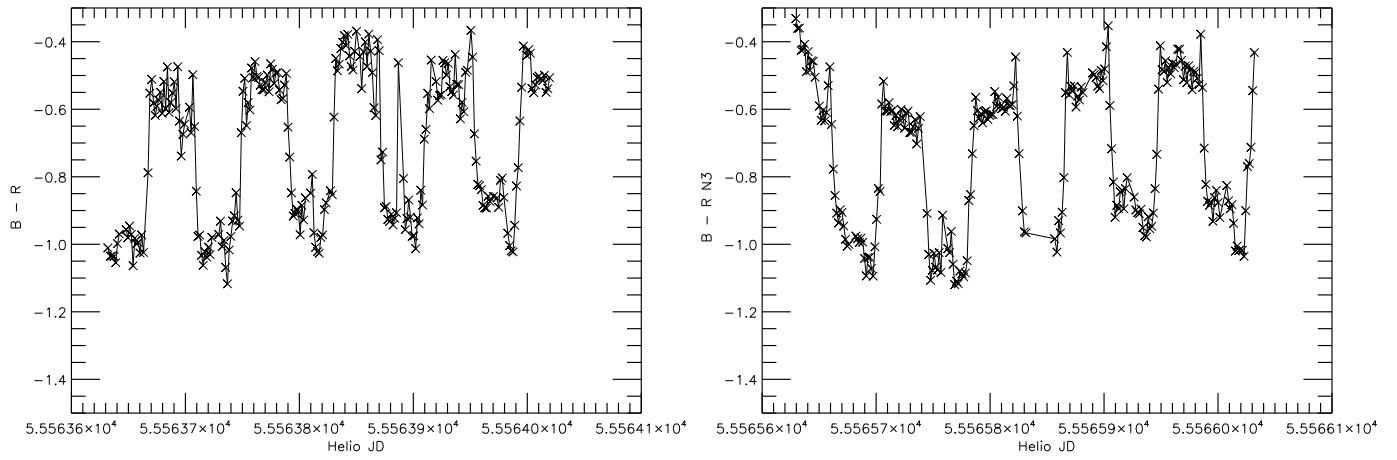


Figure 10: B-R magnitude vs. HDJ, night 1(left) and night 3(right)

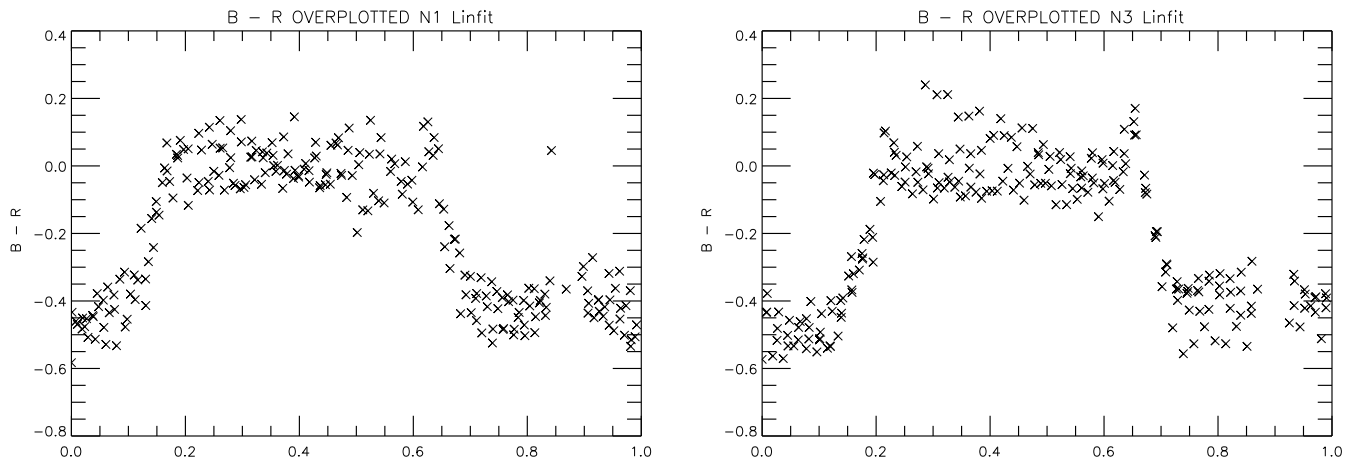


Figure 11: B-R phased night 1(left) and night 3(right)

Searching for Transients in the Kepler Mission Data

Bryant Vande Kolk
Ripon College

2011 NSF/REU Program
Physics Department, University of Notre Dame

Advisor: Dr. Peter Garnavich

Abstract: *Since early 2009, the Kepler spacecraft has continuously monitored over 150,000 stars in a 115-square degree field of view located in the constellations Cygnus and Lyra. Though the goal of the Kepler mission is to find extra-solar planets, another use of the Kepler data includes studying the behavior of normal and variable stars in the field. Every month Kepler downloads a full-field image consisting of 84 charge-coupled device channels. In this research, images acquired at the beginning of the mission have been subtracted with later images to search for transient astronomical events, such as novae and supernovae, and variable stars not yet identified from this field. Approximately 1000 variables have been found, with a number of these being possible transients. These candidate variables and transients are compared with known variable star catalogs to determine which are newly discovered objects. A fraction of these new objects will be selected by Kepler for continuous study in Cycle 3.*

Keywords: *Kepler, transient, variable, supernova,*

Introduction

Launched in March 2009 to estimate the number of Earth-sized planets within and near the habitable zone of solar-type stars, National Aeronautics and Space Administration's (NASA's) Kepler Mission tracks over 150,000 stellar objects continuously in a field of view within the constellations Cygnus and Lyra. NASA finds these planets by searching for transits, astronomical events that take place when one celestial body, such as an Earth-sized planet, crosses in front of - or what appears to be in front of - another celestial body, or in this case, a star. Currently, those working on the Kepler Mission have identified 997 stars containing a sum of 1235 planetary candidates (Borucki, W. J., et al. 2011).

The array of CCD imagers has a wide field of view - 115 square degrees - specifically so that Kepler keeps a constant eye on an area with a high stellar density of dwarf stars. The photometer

was designed based on a modified Schmidt telescope; more information about this can be found in Borucki, W. J., et al. (2010) and Borucki, W. J., for the Kepler Mission (2010). There are 42 charge-coupled devices (CCDs) that are 1024 rows by 2200 columns. With two amplifiers per CCD, Kepler runs 84 channels; furthermore, the CCDs are mounted as pairs, meaning there are 21 modules. This can be seen in Fig. 1.

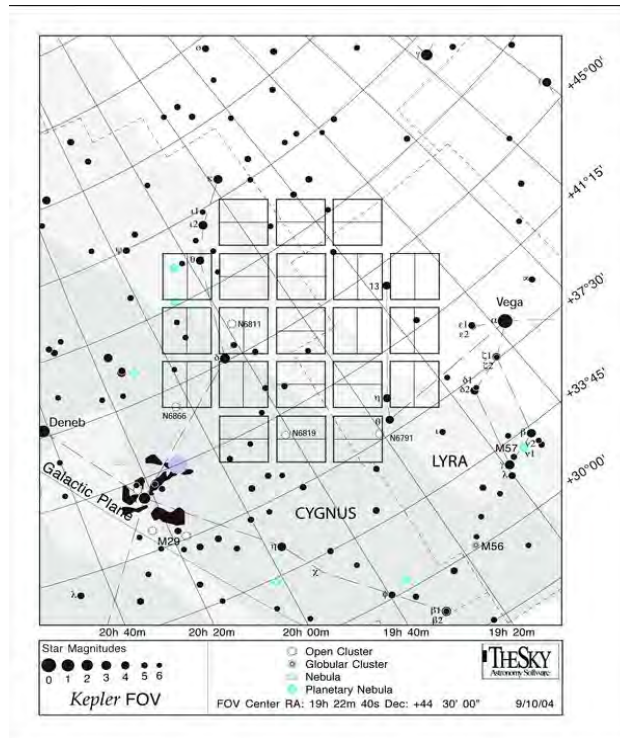


Figure 1: This image¹ displays the 42 CCDs paired into 21 modules in an image of the sky.

The data collected by Kepler is recorded in segments of quarter-years, as it is necessary for the spacecraft to rotate consistently and sequentially 90 degrees in order to illuminate the solar arrays and keep power running on the spacecraft. Due to the quarterly rotation of the spacecraft, the images of the stars are recorded on a different set of detectors (Borucki, W. J., et al.

¹ The original image can be seen at <http://kepler.nasa.gov/multimedia/Images/photogallery/?ImageID=12>. Software Bisque is credited with the information given on the webpage.

2011). As is noted in Gilliland, R. L., et al. (2011), if an object begins at Quarter 2 in channel 1, it will move to channel 53, 81, 29, and then back to channel 1 for Quarters 3, 4, 5, and 6, respectively. Also note that during Quarter 4, two CCDs - or four channels - were damaged in module 3: channels 5-8. These channels were not used in our data.

A second application of the Kepler Mission data is to detect and observe variable stars and transient astronomical events, or transients. Common transients include novae and supernovae, the latter being an important and desired find. We have an active program with Kepler to look at ~100 galaxies in the Kepler field of view in order to search for supernovae.

The purpose of this paper is to describe the process and results of searching through the Kepler Mission data to find possible variable stars, transients, and ultimately, supernovae. If a supernova is discovered in the data, we can access the images that recorded the beginning of the explosion. In certain kinds of type Ia supernovae, it is expected that a shock emission can occur less than a day after the explosion (Hayden, B. T., et al. 2010). This shock emission is due to some of the ejecta of the supernova smashing into the companion star. Simulations of this shock have been made and analyzed, though very few actual shocks have been observed. By looking through the Kepler data, we have the possibility of discovering a supernova with this characteristic in order to better study and understand the event.

Experiment

Utilizing the link to .fits full frame images (FFIs) provided by NASA's Kepler Data Analysis webpage, we accessed the monthly image downloads from Quarters 1 through 9. Due to the

orientation changing each quarter by 90 degrees, we determined it best to choose similarly-oriented quarters; in this manner, we ensure that as few stars as possible leave the frame or change CCDs. This process makes it manageable to align and combine or subtract images for comparison. We selected the orientation that Quarters 1, 5, and 9 share, as it had the most available combined data.

Eight images for the Kepler Quarter 1 observation were recorded during the late part of April 2009. Though the rest of the images we will discuss are monthly images, it appears these were taken in three successive days. The Kepler Quarters 5 and 9 observations occurred from April to June 2010 and 2011, respectively. Quarter 5 included three images, one from the latter part of each month, while Quarter 9 contained only two images, as the one from June is not yet released.

Image Reduction and Analysis Facility (IRAF), a software system with the purpose of processing astronomical data, was used to prepare the images. After all thirteen images were downloaded from Kepler, we utilized IRAF to separate each of the images into their respective 84 channels, funneling them into 84 subdirectories. We applied a script to each of the subdirectories that combined all of the Quarter 1 images into a template image. The brightness values of the template and Quarters 5 and 9 images were then divided by 100,000 in order for the next few steps to run more smoothly.

To prepare for the alignment and subtraction of the images, pixel coordinates of at least three non-saturated, well-focused stars were written into a .stamps file. This provides markers for the program, so it can recognize what to use for matching the point-spread function of the

images. After completing the above steps, we were able to run *snphot_new*, a program designed by Brian Schmidt, a researcher at Australian National University, in order to align each channel's Quarters 5 and 9 images to the respective template; the template was then subtracted from each of the respectively aligned images.

I visually searched for events and stellar objects that were incommensurable in the subtractions with “ds9”, an imaging and data visualization application that displays .fits images. For every variant, I noted the celestial coordinates and a comment about the characteristic of the variant recognized. This was done to compare the results with current catalogs of extra-solar bodies, such as the Set of Identifications, Measurements, and Bibliography for Astronomical Data (SIMBAD) and the General Catalog of Variable Stars (GCVS). SIMBAD includes a catalog of known variables in the Kepler field.

Data

Shown in Fig. 2 is a 1024x1100-pixel template image from channel 50. Noticeable traits are the star cluster NGC 6819² and scattered bright stars, separated by dimmer stars as a light background.

² Information about this star cluster can be seen at <http://helas.astro.uni.wroc.pl/data/kepler/pulsating_stars_-_Kepler_FOV/OC_Kepler.html>.

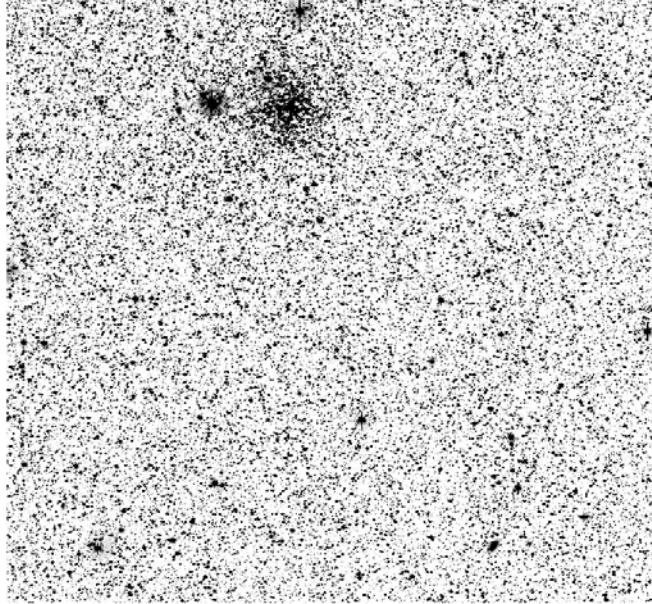


Figure 2: The template image (opposite contrast) taken from channel 50. Note that it has 1024x1100 pixels.

Figure 3 is a display of a candidate transient found in channel 58 at right ascension 19:28:36.52 and declination +47:51:22.70. The transient is the faint object that lies directly above and to the right of the crosshairs.

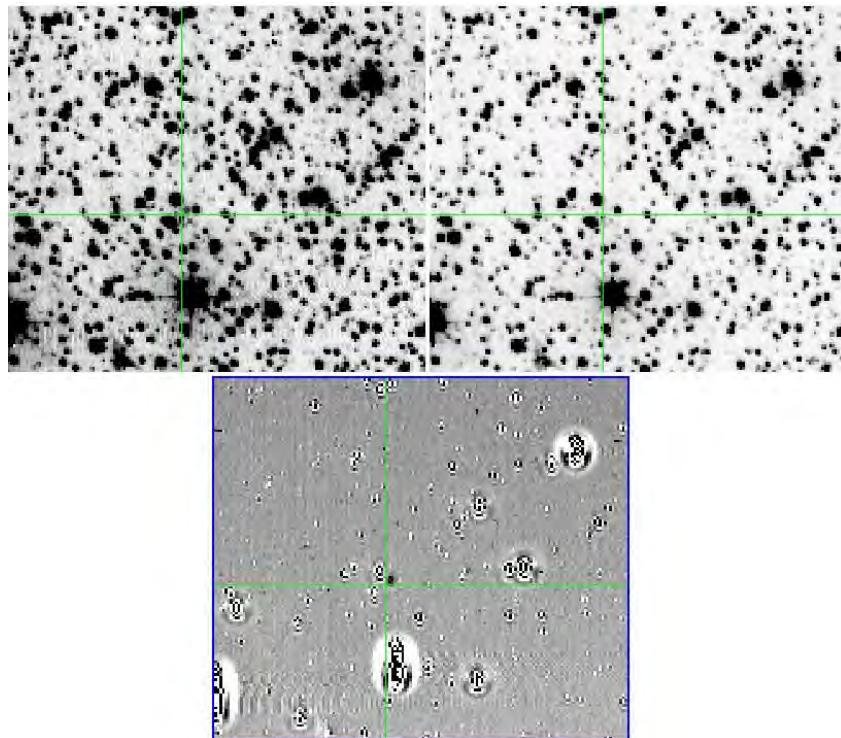


Figure 3: A Quarter 9 image of channel 58 (top-left), the template image of channel 58 (top-right), and the Quarter 9 subtracted image (bottom) are shown in opposite contrast. The candidate transient is located to the upper right of the each crosshair.

Table 1 displays 14 significant variables/transients. One is noted as being recognized by SIMBAD.

Channel	RA	Dec	SIMBAD
02	18:49:25.42	+43:39:52.61	-
09	19:05:52.79	+39:55:21.66	-
09	19:04:28.43	+40:05:06.15	-
12	19:02:30.29	+39:44:19.42	-
14	18:48:18.55	+47:07:45.15	-
17	18:58:16.14	+46:13:35.14	-
17	19:03:37.39	+45:48:17.27	-
28	19:16:16.66	+38:58:11.05	-
40	19:12:35.19	+48:07:08.55	-
42	19:21:54.71	+44:08:59.75	-
53	19:25:44.54	+51:09:31.20	V* V1119 Cyg
58	19:28:36.54	+47:51:22.70	-
73	19:45:18.02	+48:59:42.16	-
75	19:40:09.08	+50:48:17.47	-

Table 1: “Channel” refers to one of the 84 channels from which the significant variable/transient came. “RA” is right ascension while “Dec” is declination. “SIMBAD” refers to the name SIMBAD recognized if the object existed in the catalog.

Results and Analysis

A meticulous search for variables and transients in all 84 channels of the Kepler Quarters 5 and 9 monthly images resulted in 1042 candidates being found. Of these 1042, 14 candidate variables/transients have been marked as unique or significant. This marking signifies that the candidate was peculiar or dissimilar to the others in a noticeable manner. These can be seen in Table 1. For example, in Figure 3, the object identified as the possible transient is not noticeable in the template image, a compilation of images from April 2009. However, nearly two years later, it is recorded as existing in the two Quarter 9 images and subtractions.

Though many of the 1042 candidates may be known stellar objects and variables/transients, we suppose that a number of these are objects yet to be identified from the Kepler Mission data. Providing 1042 candidates for the catalog, SIMBAD recognized 240 as having celestial coordinates within 20 arc seconds of their identified stars, while only one of the 14 significant variables/transients was recognized by congruent standards. Further analysis will be done in the future to determine the significance of these findings, and some will be selected for further study by Kepler in Cycle 3.

Conclusion

The Kepler Mission, starting in the spring of 2009, monitors ~156,000 stars in a field of view within the constellations Cygnus and Lyra. Utilizing the data collected since the beginning of the mission, we have processed images from Quarters 1, 5 and 9 to search for variable stars and

transients. After visually surveying each of the 84 channels individually, we have identified 1042 candidates. In this paper we display a table of 14 significant, or unique, candidates. These candidates are compared with known variable star catalogs, i.e. SIMBAD and GCVS, to determine which are newly identified variables/transients; furthermore, a portion of the 1042 candidates will be chosen for study by Kepler in Cycle 3.

References

Borucki, W. J., et al. 2010, *Science*, 327, 977

Borucki, W. J., for the Kepler Mission, 2010, arXiv:1006.2799

Borucki, W. J., et al. 2011, arXiv:1102.0541

Gilliland, R. L., et al. 2011, arXiv:1107.5207

Hayden, B. T., et al. 2010, arXiv:1008.4797